SISSA
Scuola
Internazionale
Superiore di
Studi Avanzati

Physics - PhD course in
Statistical Physics

Statistical physics of constrained and long-range interacting quantum systems: thermalization and critical properties

Candidate:
Eduardo Gonzalez Lazo

Advisor:
Marcello Dalmonte

Academic Year 2020-21

Introduction

In generic isolated systems, non-equilibrium states are expected to thermalize: relax to states in which the values of macroscopic quantities are stationary, universal with respect to widely differing initial conditions and predictable using the framework of statistical mechanics. Intuitively less clear, however, is how these states can be reached through local dynamics that follows microscopic laws [1, 2].

Non-equilibrium dynamics of large-scale quantum many-body systems is a notorious challenge for both analytical and numerical computations. Progress in this research direction has accelerated in recent years, a trend that can be partially attributed to success in producing controllable, quantum-coherent systems of ultracold atoms [3, 4] and trapped ions [5] with high degree of isolation [6]. The latter platforms can mimic interacting quantum many-body systems by reconstructing their Hamiltonian, under precisely controlled conditions [7–10]. These experimental platforms naturally realize quantum Ising or Heisenberg models, with the possibility to engineer two-body interaction potentials decaying proportionally to $r^{-\alpha}$ as a function of the distance r between lattice sites, ranging from van-der-Waals-like ($\alpha = 6$) and dipolar interactions ($\alpha = 3$) in the context of Rydberg atoms [11, 12], to Coulomb ($\alpha = 1$) and infinite-range ($\alpha = 0$) potentials for trapped ions [13, 14]. For the case of van der Waals interactions, strong nearest-neighbor interactions can be implemented on these systems, leading to an effective constrained dynamics in both Ising- and XY-type regimes. This regime has proven fruitful to show interesting phenomena and peculiar non-equilibrium properties. Particularly, the phenomenon of weak ergodicity breaking found in Ref. [15] and its relation with the existence of many body quantum scars [16] in the spectrum of the Hamiltonian. These setups offer the possibility to access real-time quantum dynamics and strongly correlated quantum many-body states, opening numerous avenues not only for future quantum technologies, but also for studying long-standing theoretical problems. Thermalization and long-range interactions in isolated quantum systems are of fundamental interest and naturally addressed in these platforms.

The research work presented in this thesis addresses some open questions regarding thermalization and thermal equilibrium in quantum systems featuring long-range interactions and constrained dynamics. Utilizing a combination of numerical and analytical tools, this work studies the thermalization and critical properties of experimentally important models and contributes to the efforts towards the quantum simulation of complex phenomena in condensed matter and statistical physics. In particular, we focus on two main grand-issues. The first one concerns ergodicity breaking in constrained systems (inspired by strong power law interactions with large decay exponent, such as the aforementioned van der Waals), that we specifically address via characterising spectral properties. We will present two studies on constrained systems, that suggest the following picture: while constraints favor weak-ergodicity breaking (in the form of quantum scar states), they seem to unfavor strong-ergodicity breaking, such as many-body localization in the presence of disorder. The second study concerns instead the critical properties of long-range systems. There, we focus on equilibrium, critical properties, that we characterize in details in regimes of direct access to present experiments. In doing so, we introduce a methodological development, by empowering Monte Carlo algorithms with a combination of non-local loop updates - an instrumental step to address criticality. Following this second line, we present a series of additional methods developed to tackle continuous, long-range interacting systems, that have recently surged to attention due to the realization of atom supersolids.

The thesis is structured as follows. Part I focusses on the study of thermalization in constrained quantum many-body systems. In that respect, Chapter 1 reviews basics as-

pects and concepts concerning quantum thermalization in isolated systems. By means of the eigenstate thermalization hypothesis (ETH) we clarify how thermalization is directly related - and strongly tied to - the properties of individual eigenstates. The phenomena of Many-body localization and quantum many-body scars are explained, introducing different measures that characterize ETH and its breaking. Chapter 2 presents our results on the calculated ETH and spectral properties of a certain kind of constrained quantum models (PXP model with different radius of constraint). These results suggest an ergodic, ETH obeying behaviour of all the studied models although the appearance of some special eigenstates. In Chapter 3 we investigate whether quantum scars on these constrained models are stable with respect to perturbations in the Hamiltonian and if they persist for larger constraint radii. In Chapter 4 we focus on the interplay between constraints, interactions and disorder, and investigate ergodicity and its breaking under the combination of these factors. We show that 1D spin chains with local constraints can remain ergodic even in the presence of strong disorder, and explain such an unexpected behavior utilizing a series of mappings that illustrates the qualitative, 'delocalizing' effect constraints might have. The Part II of the thesis is dedicated to the study of strongly correlated systems by means of Monte Carlo methods. In Chapter 5 we investigate both the ground state and the nonzero-temperature regimes of quantum Ising chains with long-range ferromagnetic interactions. Using large-scale path integral Monte Carlo simulations we study the phase diagram and critical properties of the model. Chapter 6 presents my work on the development of an implementation of the Path Integral Monte Carlo algorithm for continuous space systems. Here, we present a benchmark of our implementation for a system of bosons interacting via a soft-core potential.

List of publications

The thesis is based on the following publications:

Chapter 3 – F.M. Surace, M. Votto, E.G. Lazo, A. Silva, M. Dalmonte and G. Giudici, *Exact many-body scars and their stability in constrained quantum chains*, *Physical Review B* **103** (2021) [2011.08218].

Chapter 4 – P. Sierant, E. Gonzalez Lazo, M. Dalmonte, A. Scardicchio and J. Zakrzewski, *Constraints induced delocalization*, *Accepted in Phys. Rev. Lett.* (2021) [2103.14020].

Chapter 5 – E. Gonzalez Lazo, M. Heyl, M. Dalmonte and A. Angelone, *Finite-temperature critical behavior of long-range quantum Ising models*, *Submitted to SciPost Phys.* (2021) [2104.15070].

Contents

Part I

Thermalization in constrained quantum systems

Chapter 1

Quantum thermalization in isolated systems

Describing a system with many constituents by keeping track of every degree of freedom is usually a practically impossible task. Statistical approach is mandatory, i.e. calculate the average behaviour of the system, as given for example by some macroscopic observable instead of the single particle dynamics. This approach finds support on the basis of statistical mechanics and thermal equilibrium, where is claim that the exact knowledge of individual trajectories is not necessary and systems can be well described by a few parameters that are time independent, i.e., temperature, internal energy, etc.. This simple description comes from the ability of systems to perform ergodic dynamics, i.e., all microscopic states of the system will be uniformly explored, constrained only by conservation laws.

In the case of classical systems, the ergodic exploration of the phase space has been traced to the chaotic motion present on the system [20]. Classical results and concepts in this subject can not be directly applied in quantum systems [2]. Significant efforts have been focused on understanding the process of quantum thermalization in isolated systems, i.e, is statistical mechanics applicable in these systems, do quantum systems act as their own bath, do quantum systems exhibit ergodic behaviour? The problem of quantum thermalization has gain much interest thanks to recent experimental progress, in controllable, quantum-coherent systems of ultracold atoms [3, 4] and trapped ions [5]. These highly tunable quantum systems that are – to very good approximation – isolated from any environment allow to characterize their quantum thermalization properties [21]. Of great interest are quantum system failing to thermalize, for protecting exotic equilibrium phenomena [22–24] and realize them in a non equilibrium setup [15, 25–27]. Opening up opportunities for the creation of novel states with long-lived coherence in systems that are now experimentally realizable.

This chapter introduces the basis on the current understanding of the process of quantum thermalization in isolated systems. In that respect in Section 1.1 is introduced the concept of thermalization for quantum system, and the ETH as the underlying mechanism for thermalization on these systems is explained. The validity of the ETH is also addressed in this chapter. Although the ETH has been numerically verified for few-body observables in a variety of systems, not all quantum systems or all eigenstates obey it. The fact that many body localized phases strongly violate ETH is explained in Section 1.2. And in Section 1.3 we address a phenomenon suggestive of weak ergodicity breaking found in experiments, explained by the existence of highly non-thermal eigenstates called quantum scars. Through the chapter different measures that characterize thermal, insulating and ETH obeying behaviour are introduced.

1.1 Thermalization in quantum systems

Given an isolated quantum system prepared in an out of equilibrium state $\hat{\rho} = |\Psi_0\rangle\langle\Psi_0|$ and described by a time-independent Hamiltonian $\hat{H}$. The expectation value of a few-body operator $\hat{O}$ at time t is

$$\langle\hat{O}(t)\rangle = \mathrm{Tr}(e^{-i\hat{H}t}\hat{\rho}e^{i\hat{H}t}\hat{O}) = \sum_{n,m}\rho_{nm}O_{mn}e^{-i(E_n-E_m)t}, \tag{1.1}$$

where ρ_{nm} and O_{mn} are the matrix elements of the density matrix and the operator $\hat{O}$ in the eigenbasis $\{|E_n\rangle\}$ of $\hat{H}$, such that $\hat{H}|E_n\rangle = E_n|E_n\rangle$, and E_n is the energy for the eigenstate n, for simplicity $\{E_n\}$ is an ordered set.

Thermalization in quantum systems normally refers to observables. An observable is said to thermalize if in the thermodynamic and long time limit the average expectation value of the observable ($\bar{O}$) is equal to the corresponding thermal ensemble [canonical (C) and microcanonical (MC)] value ($\langle\hat{O}\rangle_T$),

$$\bar{O} = \langle\hat{O}\rangle_T = \langle\hat{O}\rangle_C = \langle\hat{O}\rangle_{MC} \tag{1.2}$$

$$\langle\hat{O}\rangle_C = \frac{1}{Z}\,\mathrm{Tr}(e^{-\beta\hat{H}}\hat{O}), \tag{1.3}$$

$$\langle\hat{O}\rangle_{MC} = \frac{1}{N_\Delta}\sum_{|E_n-E|\leq\Delta} O_{nn}, \tag{1.4}$$

where the total energy and the inverse temperature β are related by $E = \mathrm{Tr}(\hat{H}\hat{\rho}) = (1/Z)\,\mathrm{Tr}(e^{-\beta\hat{H}}\hat{H})$ with $Z = \mathrm{Tr}(e^{-\beta\hat{H}})$ and $N_\Delta \equiv \sum_{|E_n-E|\leq\Delta} 1$ being Δ a small energy window. Importantly, is also required that temporal fluctuations of the expectation value about the thermal ensemble prediction are small at most later times.

If one tries to calculate $\bar{O}$ from Eq. (1.1) assuming there are not degeneracies in the energy spectrum (reasonable assumption for generic quantum systems after removing all trivial symmetries) one obtains

$$\bar{O} \equiv \lim_{t_0\to\infty}\frac{1}{t_0}\int_0^{t_0} dt\langle\hat{O}(t)\rangle = \sum_n \rho_{nn}O_{nn}. \tag{1.5}$$

From Eq. (1.5), it would appear the equilibrium expectation value depends on the initial state of the system through the matrix elements ρ_{nn} and this is at odds with the concept of thermalization. Moreover, a many body system will need a long time to make sure that the sum of the non diagonal elements in Eq. (1.1) averages to zero which is in contradiction with experimental observation.

1.1.1 The eigenstate thermalization hypothesis

ETH is a conjecture introduced by Deutsch and Srednicki [28, 29] and propose an ansatz for the matrix elements of observables in the basis of the eigenstates of a Hamiltonian [30]:

$$O_{mn} = O(E)\delta_{mn} + e^{-S(E)/2}f_0(E,\omega)R_{mn}, \tag{1.6}$$

where $E \equiv (E_m + E_n)/2$, $\omega \equiv E_n - E_m$ and $S(E)$ is the thermodynamic entropy at energy E. Both $O(E)$ and $f_0(E,\omega)$ are smooth functions of their arguments, $O(E)$ is equal to the expectation value of the observable O in the microcanonical ensemble at energy E and R_{mn} is a random variable with zero mean and unit variance.

This ansatz has immediate implications in the understanding of thermalization in many body quantum systems. Indeed, assuming that the expectation value of the total energy

$$E = \sum_n \rho_{nn} E_n \tag{1.7}$$

has a quantum uncertainty

$$\Delta \equiv \left[\sum_n \rho_{nn} (E_n - E)^2 \right]^{1/2} \tag{1.8}$$

that is small (for typical states, this quantity scales with the system size L as $\Delta \sim L^{-1/2} E$). In the large L regime, combining the ansatz Eq. (1.6) and the time average of the expectation value in Eq. (1.5) one obtains the relation

$$\bar{O} = \langle \hat{O} \rangle_T + O(\Delta^2) + O(L^{-1}) + O(e^{-S/2}). \tag{1.9}$$

Using this ansatz, one encounters that the fluctuations of $\langle \hat{O}(t) \rangle$ about its equilibrium value $\bar{O}$ are small. Then, whatever the initial value $\langle \hat{O}(t=0) \rangle$, $\langle \hat{O}(t) \rangle$ must eventually approach its equilibrium value, and remains near it most of the time.

As a consequence of ETH one can explain the occurrence of thermalization in isolated quantum systems. Moreover, it follows that in the thermodynamic limit the expectation value of every few-body operator in every energy eigenstate is the thermal value. The previous statement sometimes is called "strong ETH" (every eigenstate), in the case the expectation value for some eigenstates does not agree with the corresponding thermal value it is normally said that the system only obey ETH in a weak sense (weak ETH).

The main approach for studying ETH numerically is exact diagonalization (ED). The eigenstates and their ETH properties for discrete Hamiltonians like the Hubbard models or spins systems have been calculated using ED, where many of these lattice systems have been found to obey ETH [31–38]. ETH is difficult to thoroughly test numerically because it requires calculating the many-body eigenstates using ED and extrapolate the results to the thermodynamic limit. While all known examples of systems that thermalize obey ETH, still is not clear if ETH is a necessary condition for thermalization.

1.2 Many body localization

The exchange of energy and particles between different parts of a system is required in order for this to thermalize. Therefore, an insulating system is expected to break ergodicity. Insulating behaviour was studied in non-interacting disordered systems. Here, a disorder potential change the single particle eigenstates in a lattice, instead of having Bloch states the eigenfunctions become localized in some region of space and decay exponentially far away from that. This phenomenon goes under the name of Anderson localization [39, 40].

Importantly was also the study of this phenomenon for interacting particles, where the interaction could induces processes which may potentially destroy localization. This lead to the discovery of an Anderson localization similar mechanism for interacting systems, dubbed many body localization(MBL) [41–44]. This phenomenon exhibit a quantum phase transition from an ergodic phase to a dynamical localized phase, where interestingly the latter can survive even at nonzero temperatures. This transition is an eigenstate phase transition marked by a sharp change in properties of the many-body eigenstates and thus in the dynamics of the system. The MBL phase has been proved to be a stable phase making this phenomenon a robust mechanism that avoids thermalization in closed systems.

The localized phase was found to break ETH in Ref. [44]. There, Pal and Huse using ED calculated the eigenstates for the Heisenberg spin 1/2 chain of size L with random fields along the z direction

$$\hat{H} = \sum_{i=1}^{L} h_i \hat{S}_i^z + J\hat{\mathbf{S}}_i \cdot \hat{\mathbf{S}}_{i+1}, \tag{1.10}$$

where the static-random fields for each site h_i are independent, uniformly distributed random variables in the interval $[-h, h]$.

Eigenstate expectation values. In particular they calculated the local expectation value of the z component of the spin

$$\langle E_n | \hat{\sigma}_i^z | E_n \rangle \tag{1.11}$$

in eigenstates $|E_n\rangle$ and found that in the localized phase this quantity fluctuate widely between adjacent many-body eigenstates, not obeying the ETH expected behaviour [Eq. (1.6)] where a local observable should be smooth function of energy. The scaling of the average difference of $\langle E_n | \hat{\sigma}_i^z | E_n \rangle$ between adjacent eigenstates showed that for weak disorder strength (h) this difference decays exponentially in L, signaling an ergodic, ETH obeying behaviour in the thermodynamic limit. On the contrary for large disorder strength the difference is non-vanishing as L is increased, suggesting that ETH is violated. This result is depicted in Fig. 1.1 where one can see the clear differences between the two regimes.

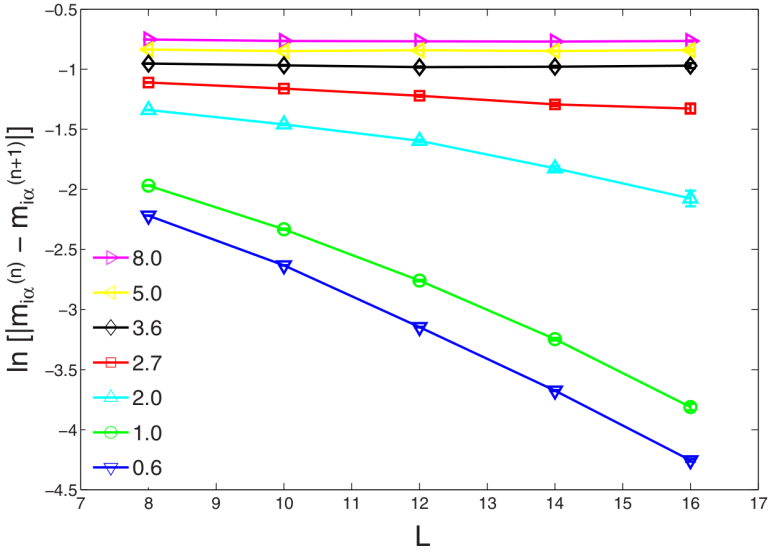

Figure 1.1: Logarithm of the averaged difference between the local magnetizations in adjacent eigenstates for different h values (indicated in the legend). The $m_{i\alpha}^{(n)}$ is the same quantity in Eq. (1.11) where n refers to the state in certain realization α (certain set $\{h_i\}$). The average is over disorder realizations, states and sites. The figure is taken from Ref. [44].

Average level spacings ratio. The level statistics was also studied, in Ref. [44] the average ratio of adjacent level spacings was calculated. The previous quantity is defined as:

$$\overline{r} = \left\langle \frac{\mathrm{Min}\{\Delta E_n, \Delta E_{n+1}\}}{\mathrm{Max}\{\Delta E_n, \Delta E_{n+1}\}} \right\rangle, \tag{1.12}$$

where $\Delta E_n = |E_n - E_{n-1}|$. This quantity can be seen as an overall result from the studies of Random Matrix Theory (RMT) and quantum chaos and it has been used to quantify the distance from integrability on finite size lattices systems [45–47] and to characterize diffusive-to-insulating transition and phases in the MBL phenomenon [42, 48, 49]. In the localized, insulating phase, in the thermodynamic limit, the eigenstates are localized in the many-body Fock basis of localized single-particle orbitals. Therefore, states that are nearby in energy are far apart in this Fock space and do not interact or show level repulsion. As a result, nearby energy levels are simply Poisson distributed yielding $\overline{r}_{PS} \approx 0.386$. In the diffusive phase, the level statistics of a large sample are those of the Gaussian orthogonal ensemble (GOE) in the RMT, where $\overline{r}_{GOE} \approx 0.53$ (associated with a Wigner-Dyson statistics). In general for an ergodic systems this quantity is expected to flow to the value $\overline{r}_{GOE}$ as the thermodynamic limit is reached.

It was also proved numerically in [50,51] that MBL eigenstates display a low amount of entanglement, where the entanglement scales proportional to the volume of the boundary of the subsystem, known as area law entanglement. Oppositely, thermal eigenstates in the same system showed volume-law entanglement with the entanglement equal to the thermal equilibrium entropy of the subsystem, that scales with the number of its degrees of freedom.

All this suggested the existence of conservation laws for strongly disordered systems. This expectations were made concrete in [51–53], proposing an emergent 'integrability' in the MBL phase with Hamiltonians that are non linear functionals of a complete set of local integrals of motions (LIOMs). This emergent integrability explains the breakdown of ergodicity where information about the initial state is retained in the initial values of LIOMs. The MBL integrability is conceptually different to other known types of integrability present in non-interacting systems and in Yang-Baxter integrable systems [54], been the MBL emergent integrability robust against weak and finite perturbations of the Hamiltonian.

1.3 Many-body quantum scars

Many body localized systems fail to thermalize irrespective their initial state [54]. Another phenomenon inconsistent with ergodicity and thermalization but strongly dependent on the initial state has been discovered experimentally [15]. The experiment consisted of neutral atoms loaded in a one-dimensional tweezer array. The atoms can couple to highly exited Rydberg states resulting in repulsive van der Waals interactions between Rydberg atoms. The quantum dynamics of the system is described by the Hamiltonian

$$H = \frac{\Omega}{2} \sum_i \hat{\sigma_i}^x - \Delta \sum_i \hat{n}_i + \sum_{i<j} V_{ij} \hat{n}_i \hat{n}_j, \tag{1.13}$$

where Δ is the detuning of the driving lasers from the Rydberg state, $\hat{n}_i = |r_i\rangle \langle r_i|$ is the occupation of the Rydberg state, $\hat{\sigma}_i^x = |g_i\rangle \langle r_i| + \text{h.c.}$ describes the coupling between the ground state $|g_i\rangle$ and the Rydberg state $|r_i\rangle$ of an atom at position i, driven at Rabi frequency Ω, V_{ij} is the interaction energy between Rydberg excitations. The interaction strength V_{ij} can be tuned varying the distance between the atoms or by coupling them to a different Rydberg state. The strong interaction between Rydberg atoms provides an effective constraint on the dynamics, not allowing simultaneous excitations of nearby atoms into the Rydberg state. Interestingly, when the system was prepared in a charge density wave state (CDW), with every odd atom in a exited state, and then quenched the parameter Δ to zero, the obtained dynamics exhibited oscillations with anomalously slow

decay. Here, measurements of the Rydberg state occupation n_i showed that the initial CDW state collapses after the quench, a new state with an excitation at every even site builds up and the system continues to oscillate between these two states (Fig. 1.2). The oscillations persist on the full time range accessible in the experiment, much longer than the timescales Ω^{-1} and $V_{i,i+1}^{-1}$.

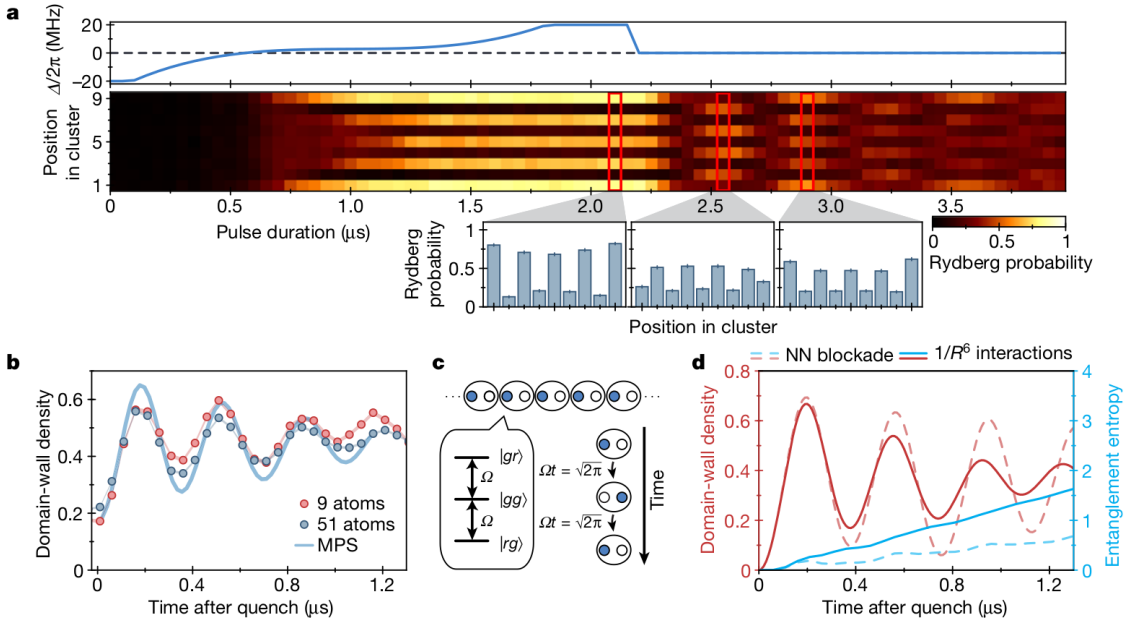

Figure 1.2: (a) Δ is controlled in time in order to adiabatically prepare the CDW state, then is quenched to $\Delta = 0$. The spatially resolved Rydberg probability is shown for an array of 9 atoms. (b) Domain-wall density after the quench. (c) Illustration of a toy model for the oscillations. (d) Numerical simulation of domain-wall density and entanglement entropy after the quench. Figure taken from Ref. [15].

The initial state energy density corresponds to an infinite temperature ensemble with respect to the quenched Hamiltonian and interestingly the system does not relax to thermal equilibrium, or it does well beyond experimental timescales. Oppositely, it was found that for other initial states the decay to thermal expectation values is rather fast, and no anomalous oscillations are observed. It was later understood that this phenomenology is due to a specific set of states present in the spectrum, dubbed quantum many-body scars [16, 55], in analogy with a similar phenomenon in single-particle quantum chaos [56].

1.3.1 The PXP model

The Rydberg atom experiment in Ref. [15] described by Eq. (1.13) is effectively captured by a quantum model with kinetic constraints. The constraints in this model are induced by strong nearest-neighbor repulsion between atoms in excited states. The interaction between Rydberg atoms suppresses simultaneous excitations of nearby atoms, and allow the excitation to Rydberg state only for pairs of atoms separated by at least one site. In the strong interaction limit $V_{i,i+1} >> \Omega$, the system evolves in an effective constrained Hilbert space. Here, one can project the Hamiltonian onto the subspace spanned by configurations where only excitations separated by at least one site are admitted, obtaining an effective

Hamiltonian

$$H_{PXP} = \sum_{j}^{L} P_{j-1} X_j P_{j+1}, \tag{1.14}$$

where $P_i = (1 - Z_i)/2$ and X_i, Z_i are the X and Z Pauli matrices at site i respectively and L is the number of sites. This Hamiltonian describes the so-called PXP model.

Using exact diagonalization methods Turner et al. calculated the eigenstates of this model [55] and characterize the ETH behaviour of these states. In that respect, the expectation value of a local observable $O^Z = (1/L)\sum_{j=1}^{L} Z_j$ in the eigenstate basis to test the diagonal part of the ETH ansatz [Eq. (1.6)] was calculated. The expectation value for most eigenstates was found to be concentrated in the vicinity of the canonical ensemble prediction. Interestingly, from this analysis there was also found a number of states that clearly violates the ETH prediction (dubbed "scars") [see Figure 1.3 (left panel)]. The scars and the tower of states departing from them with weakly non thermal values extend trough the whole spectrum and the number of scars scales proportionally to the system size L.

Entanglement entropy of eigenstates. The bipartite entanglement of the eigenstates S was also calculated and their results are reproduced in Figure 1.3 (right panel). The equivalence of all observables to their canonical values proposed by the ETH implies that the von Neumann entanglement entropy of a subregion A in an eigenstate $|E_n\rangle$, $S^{E_n} = -\operatorname{Tr}_A(\hat{\rho}_A^{E_n} \ln \hat{\rho}_A^{E_n})$ is equal to the thermodynamic entropy of A at temperature T which correspond to the eigenstate energy E_n. Here a special band of eigenstate with low entropy (labeled as 0,...,7) was found and is clearly differentiable from the cloud of thermal states. It was also demonstrated that the entanglement entropy of these scars does not scale obeying a volume law with the system size while thermal states on this system do.

The previous results demonstrate that the PXP model obeys the weak ETH due to the existence of this relative small number of non-thermal eigenstates. These scars in comparison with the thermal eigenstates resulted to have large overlap with the CDW state, therefore a quantum quench from the CDW state was expected and proved to give rise to coherent oscillations, and consequently was claimed that these eigenstates play a key role in the experimentally obtained many body revivals in [15].

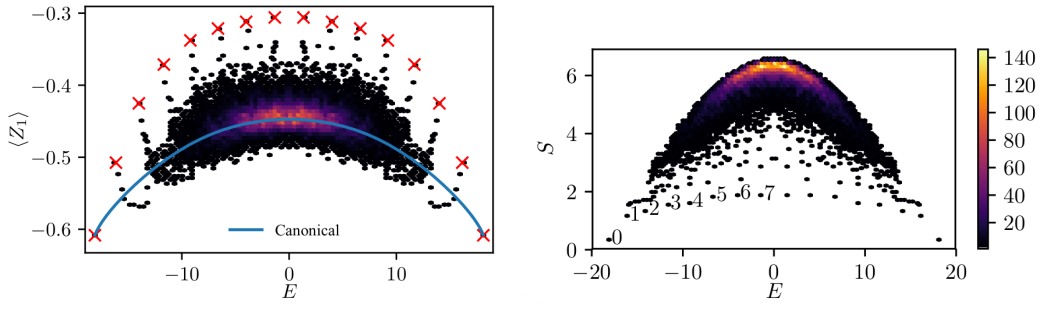

Figure 1.3: Expectation value of the local observable Z_1 (left panel) as a function of energy. The color scale indicate the density of points, contributions from scars are marked by a cross in the figure and the continuous line marks canonical thermal average. Bipartite entanglement entropy (right panel) as a function of energy. Figures taken from Ref. [55].

Chapter 2

ETH characterization in constrained models

2.1 Introduction

The PXP model introduced in Section 1.3.1 is defined on a constrained Hilbert space excluding configurations with two adjacent excitations. This reduction of the Hilbert space allows to perform exact studies up to system sizes that are considerably larger when compared to the usual 'unconstrained' models. Interestingly, one can generalize the PXP model to take into account larger radius of constraints. In this case the strong interactions allow excitations to Rydberg states only for pairs of atoms separated by at least α sites [12, 15, 57–59]. As the radius of constraint is increased the Hilbert space dimension $\mathcal{H}_d(L)$ is reduced for a certain system size L.

The characterization of thermal properties of eigenstates and insulating MBL behaviour of an isolated system relies mainly on ED calculations. While in principle one can diagonalize any Hamiltonian matrix by numerical means, in practice these numerically exact studies are restricted for rather small systems sizes. In the case of spin chain systems, the study is restricted to few tens of spins and great care has to be taken when drawing conclusions about the thermodynamic limit. The system size restriction comes from the exponential increase of $\mathcal{H}_d(L)$ with the number of spins ($\mathcal{H}_d(L) = 2^L$ for a spin 1/2 system).

Although there has recently been much of activity and interest in characterizing the finite-energy density (exited states) properties of quantum models [60], quantum models with local constraints like generalizations of PXP model is an uncharted territory. There is simply not much known on how these models behave, not only regarding thermalization, but on rather general grounds. The peculiar scaling of the configuration space on these models facilitate the study of finite-volume effects, but may also lead to cross comparison (two constrained systems of the same size may have considerably different Hilbert space). Importantly, these spin models are immediately motivated by Rydberg atoms experiments, and simple instances like the PXP model have shown interesting properties. Lastly, it is not immediately clear how the combination of disorder and local constraints may affect quantum transport.

This chapter presents our results on the calculated ETH and spectral properties of the PXP model for different constraint radius. ED methods were employed to calculate all the eigenstates for different symmetry sectors using periodic and open boundary conditions.

2.2 Model and methods

The model studied is a one dimension spin 1/2 lattice described by the Hamiltonian

$$\hat{H} = \sum_{i=1}^{L} P_i^{\alpha} X_i P_{i+1+\alpha}^{\alpha}, \tag{2.1}$$

where the projectors $P_i^{\alpha} = \prod_{j=i-\alpha}^{i-1}(1 - Z_j)/2$ assure that the dynamics is confined to a constrained Hilbert space and $\alpha = 1$ reduce to the usual PXP model. Here, the strong interactions allow excitations to Rydberg states only for pairs of atoms separated by at least α sites.

We analyzed the model in Eq. (2.1) via ED studies, performed in both open(OBC) and periodic(PBC) boundary conditions and in a variety of reflection and translation symmetry sectors. Here, for simplicity, we discuss our results and model properties for PBC and symmetry sectors $I = +1$ and $K = 0$ for reflection and translation, respectively. Analysis of results for OBC and others symmetries sectors lead us to the same conclusion stated at the end of this chapter.

The local dimension d_α of the system for different constraint radius α satisfies the equation[1]

$$(d_\alpha)^{\alpha+1} = (d_\alpha)^{\alpha} + 1. \tag{2.2}$$

The following table list the different local dimension, maximum system size L and corresponding $\mathcal{H}_d$ we fully diagonalized for several values of α.

α	d_α	L	$\mathcal{H}_d$
1	1.61803	30	31836
2	1.46557	36	13604
3	1.38028	48	55449
4	1.32472	50	13190
5	1.2852	60	29445

Table 2.1: Different systems sizes and configuration space dimension for the different models we studied with different radius of constraint α

2.3 Results

Our first step was to compute the half-chain bipartite entanglement entropy of every eigenstate for different radius of constraint. Our results coincide with existing ones for $\alpha = 1$ model in Ref. [16], showing hallmark features such as the "band of scars", i.e, low-entropy eigenstates that extend trough the spectrum [see Fig. 2.1]. Such a feature disappears when considering other values of α; instead low-entropy eigenstates appear in "towers" in the central region of the spectrum.

Subsequently, we calculated the expectation value of local observables in the eigenstates. In Figure 2.2, the calculated expectation value $\langle Z_i \rangle = \langle E_n | \sum_i Z_i | E_n \rangle$ as a function of the eigenstate energy E_n is presented. There, the majority of the eigenstates produce thermal

[1] Although there is no explicit solution of this equation for $\alpha > 3$ one finds the asymptotic form $d_\alpha = 1 + \frac{W(\alpha)}{\alpha} + ...$ where W is the Lambert W-function solving the equation $W(x)e^{W(x)} = x$. Already at $\alpha = 5$ the error is about 1%.

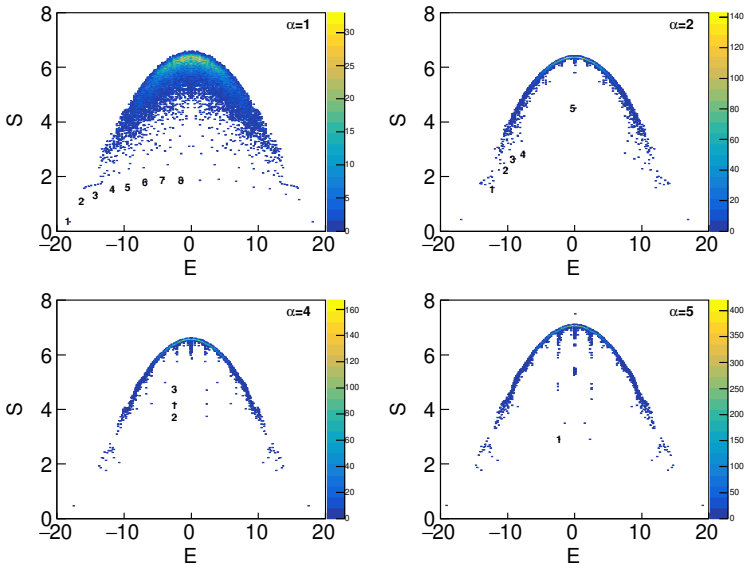

Figure 2.1: Half chain bipartite entanglement entropy calculated as a function of the eigenstate energy for different values of radius of constraint α. Color scale indicates the density of data points. Eigenstates showing special features are labeled with numbers for the different α values.

expectations values. The special case $\alpha = 1$ exhibit this band of eigenstates that don't obey the ETH. Results for $\alpha > 1$ do not show mayor deviations from thermal expectations values. Still, the special eigenstates found when analyzing the entanglement entropy(labeled in the figures) show non thermal expectation values for some radius of constraint.

The study on how the locality of observables influences the eigenstate expectation values is depicted in Figures 2.3 and 2.4. Here, $\langle X_i X_{i+1} \rangle = \langle E_n | X_i X_{i+1} | E_n \rangle$ and $\langle X_i X_{i+4} \rangle = \langle E_n | X_i X_{i+4} | E_n \rangle$ expectation values as a function of the eigenstate energy were calculated. The analysis of our results indicates that expectation values such as $\langle X_i X_{i+4} \rangle$ do not show great deviations from their thermal values even for the $\alpha = 1$ case. Oppositely, for observables with shorter support such as $\langle X_i X_{i+1} \rangle$, the band of scars eigenstates appears in the $\alpha = 1$ model.

We present our study of the spectral statistics for different values of α. The average ratio of adjacent level spacings $\overline{r}$ defined in Eq. (1.12) was calculated, where the average was taken over the full spectrum. For an ergodic system, this quantity is expected to flow to the value $\overline{r}_{GOE} \simeq 0.53$ associated with a Wigner-Dyson statistics. While for $\alpha = 1$ ergodicity has been already verified in various works [61, 62], we check this assumption when $\alpha > 1$ in Fig. 2.5 (a) , where we show the values of $\overline{r}$ for different α and system sizes. We find a clear flow to $\overline{r}_{GOE}$ for increasing system sizes. We can therefore argue that the system has a spectral statistics compatible with ergodicity.

Finally, the scaling of the average difference of $m_n = \langle E_n | \hat{\sigma}_i^z | E_n \rangle$ between adjacent eigenstates as a function of the system size L was calculated and is presented in Figure 2.5 (b). An exponential decay of this quantity is present for all the different radius of constraints signaling an ergodic, ETH obeying behaviour in the thermodynamic limit for all the models.

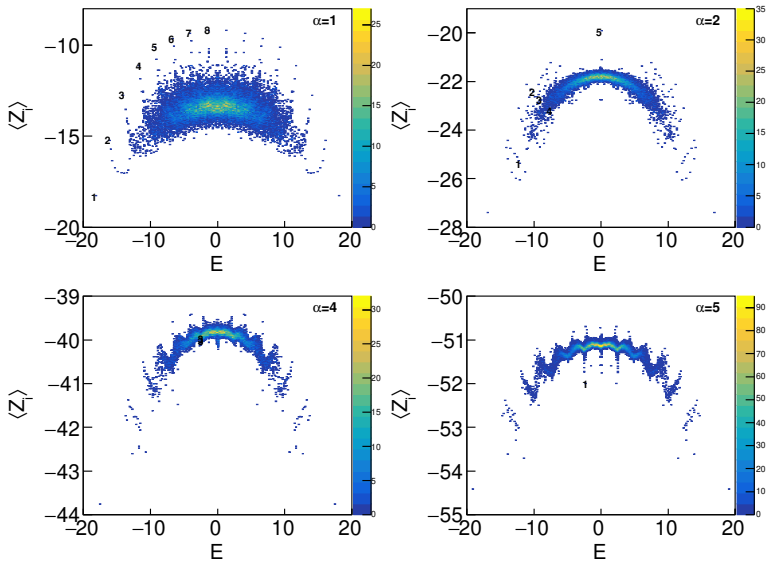

Figure 2.2: Expectation value $\langle Z_i \rangle$ in the eigenstates as the function of the corresponding energy of the state for the different α models. Expectation values in special eigenstates are labeled (see text).

2.4 Conclusions

Extensive full ED studies were performed in the generalized PXP model with different radius of constraints. We characterized spectral and ETH properties of these models. Low-entropy eigenstates that extend trough the spectrum were only found in the original($\alpha = 1$) PXP model. Although the appearance of these special eigenstates in the $\alpha = 1$ model, more general estimators (i.e., average level spacing ratio scaling) suggest an ergodic, ETH obeying behaviour of all the studied models. In the same manner our results suggest no existence of integrable behaviour on these systems. The results presented in this section provided the building blocks for the studies in the next two sections.

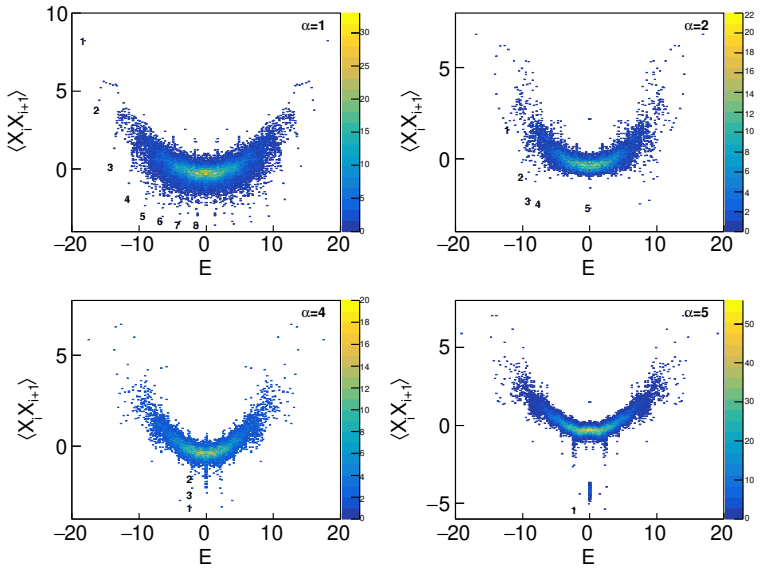

Figure 2.3: Expectation value $\langle X_i X_{i+1} \rangle$ in the eigenstates as the function of the corresponding energy of the state for the different α models. Expectation values in special eigenstates are labeled.

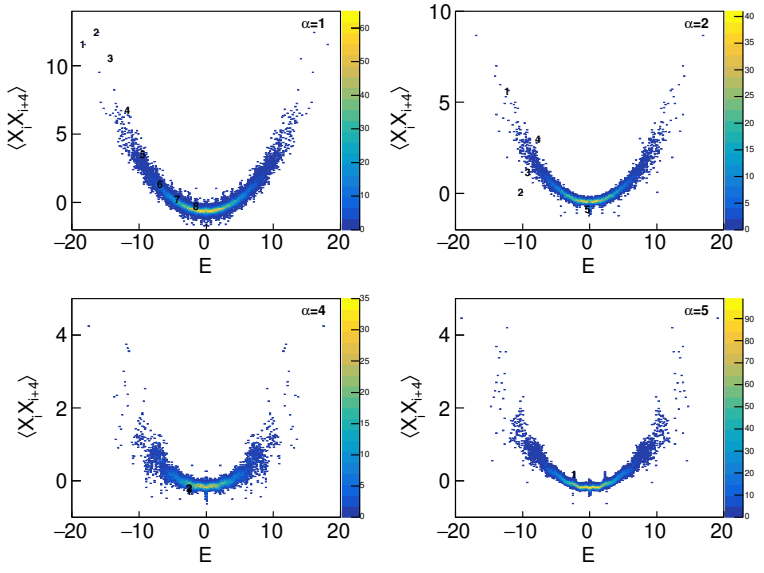

Figure 2.4: Expectation value $\langle X_i X_{i+4} \rangle$ in the eigenstates as the function of the corresponding energy of the state for the different α models. Expectation values in special eigenstates are labeled.

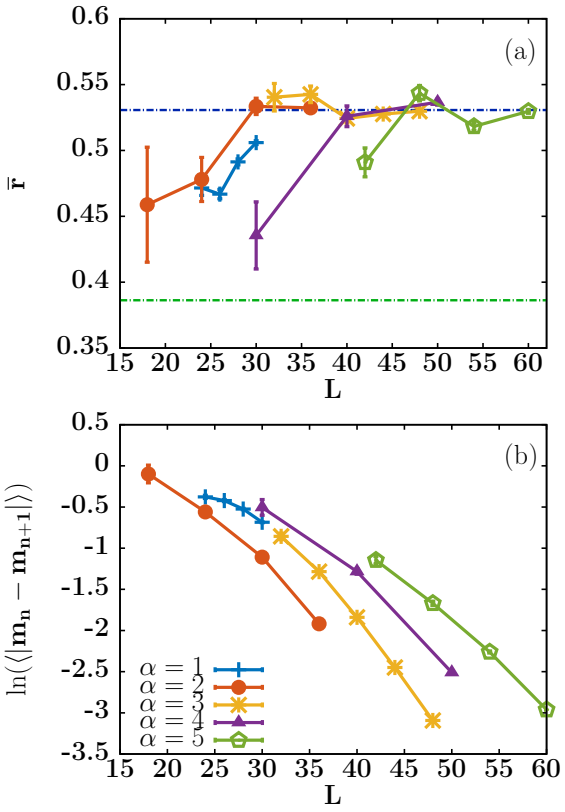

Figure 2.5: (a) Ratio $\overline{r}$ of nearby gaps averaged over the full spectrum for different values of α. The dashed horizontal lines represent $\overline{r}_{GOE}$ and $\overline{r}_{PS}$ values. (b) Logarithm of the averaged difference between the local magnetizations in adjacent eigenstates for different α values as a function of the system size L.

Chapter 3

Exact many-body scars and their stability in constrained quantum chains

3.1 Introduction

Quantum scars in the PXP model were originally used to explain the slow dynamics observed by evolving a charge-density wave (CDW) initial state in the above-mentioned experiment with Rydberg atoms: For a chain of length L, there are $L+1$ scar eigenstates, with a large overlap with the CDW, spread throughout the spectrum and (approximately) equally spaced in energy. Crucially, numerical results reveal hybridization of these scars with thermal eigenstates, implying that they are not stable in the thermodynamic limit [61]. Therefore the resulting dynamics from this initial state is expected to eventually thermalize. However, two exact uniform matrix product eigenstates have been found for all (even) system sizes [63]. This fact demonstrated the existence of ETH violating eigenstates that survive in the infinite size limit, and motivated the study of their stability against perturbation. In Ref. [64] the authors address this problem by using perturbation theory: From the scaling of the averaged matrix elements, they find no qualitative difference between the scars and thermal eigenstates, and thus deduce that the scars are not stable against perturbations. Nonetheless, they claim that thermalization is slow, because of parametrically small matrix elements.

Here, we analyse a different quantity (the fidelity susceptibility), which is a renowned probe of quantum chaos [65–67], and is not subject to the arbitrariness of the averaging procedure. Part of our results contrast with Ref. [64], showing that the scars with zero energy have a completely different behavior from thermal eigenstates and are anomalously stable to first order in perturbation theory. These findings suggest that thermalization of quantum scars is even slower than previously expected, having originated from effects beyond the first perturbative order.

We remark that this anomalous stability is observed only for scars with zero energy, so we cannot conjecture a similar mechanism for explaining the persistence of non-exact scars at finite energy in the PXP model. In fact, although a construction based on a "single mode approximation" suggests a possible connection between the band of $L+1$ quantum scars at all energies and the matrix product state (MPS) quantum scars at zero energy [63], these two sets of low-entropy eigenstates appear to have different origin. For example, while the former are stabilized by a specific fine-tuned perturbation [68] and have

logarithmic scaling of entanglement entropy with system size, the latter are destroyed by the same perturbation and have finite entanglement entropy in the thermodynamic limit.

In order to frame our finding about scar stability in the broader picture of ETH violations in constrained quantum systems, we prove that a novel set of exact eigenstates arising at zero energy (and at non-zero energy, when open boundary conditions are imposed) exists in generalized PXP models with $\alpha > 1$. We do not find a band of eigenstates equally spaced in energy like the one observed in the PXP model. These results suggest that exact scars are a generic property of one-dimensional models constrained by Rydberg blockade. We then extend our stability analysis to this second set of scars, and show how, in analogy with the $\alpha = 1$ case, they display anomalous stability.

The chapter is structured as follows. In Sec. 3.2, we introduce the PXP model and the scar eigenstates, and we set the notation for the following sections. In Sec. 3.3 we introduce the fidelity susceptibility and put forward a link between such observable and a recently proposed spectral version of the adiabatic gauge potential [67, 69]. In Sec. 3.4 we focus on the models with radius of constraints $\alpha > 1$: we describe the exact scars with $E = 0$ as product states of "dimers" (Sec. 3.4.1), and the exact scars with $E \neq 0$ as matrix product states (Sec. 3.4.2); finally, we show that the exact scars with $E = 0$ are anomalously stable against perturbations (Sec. 3.4.4).

3.2 The model

The model considered is the PXP model, introduced in Section 1.3.1. We report here, for convenience, the Hamiltonian in terms of the Pauli matrices X_i, Y_i, Z_i at site i and the operators $P_i = (1 - Z_i)/2$, $n_i = (1 + Z_i)/2$. In the constrained space we define

$$H_0 = X_1 P_2 + \sum_{j=2}^{L-1} P_{j-1} X_j P_{j+1} + P_{L-1} X_L \tag{3.1}$$

for open boundary conditions and

$$H_0 = \sum_{j=1}^{L} P_{j-1} X_j P_{j+1} \tag{3.2}$$

with the identification of the sites $j \equiv j + L$ for periodic boundary conditions. We are interested in the effects induced by a perturbation V that has the same symmetries of H_0. More concretely, the Hamiltonian is $H = H_0 + \lambda V$, where

$$V = X_1 P_2 Z_3 + \sum_{j=2}^{L-2} P_{j-1} X_j P_{j+1} Z_{j+2} + \sum_{j=3}^{L-1} Z_{j-2} P_{j-1} X_j P_{j+1} + Z_{L-2} P_{L-1} X_L \tag{3.3}$$

for the case of open boundary conditions and

$$V = \sum_{j=1}^{L} (P_{j-1} X_j P_{j+1} Z_{j+2} + Z_{j-2} P_{j-1} X_j P_{j+1}) \tag{3.4}$$

for periodic boundary conditions.

Both H_0 and V commute with the space reflection symmetry I and anticommute with the particle-hole symmetry $C_{ph} = \prod_i \sigma_i^z$. As a consequence, the spectrum is symmetric

with respect to the eigenvalue $E = 0$ and the energy zero eigenspace has a dimension growing exponentially with system size [70]. For more details about the peculiar properties of the spectrum we refer to Appendix A.1.

Many-body scars

As stated above, many-body scars are states that do not satisfy ETH. It was shown in Ref. [27] that the spectrum of the PXP model exhibits a band of equally-spaced many-body scars. These scars were responsible for the observation of long-lived oscillation in a Rydberg atom experiment [15]. Their exact form is not known analytically, and their persistence in the thermodynamic limit is still an open question. However, as was shown in Ref. [63], H_0 has also some exact scars in the form of MPS eigenstates at finite energy density. For open boundary conditions they are defined as

$$|\Gamma_{i,j}\rangle = \sum_{\{\sigma\}} v_i^T A_{\sigma_1\sigma_2} \dots A_{\sigma_{L-1}\sigma_L} v_j \, |\sigma_1\sigma_2 \dots \sigma_{L-1}\sigma_L\rangle \tag{3.5}$$

with

$$A_{00} = \begin{pmatrix} 0 & -1 \\ 1 & 0 \end{pmatrix}, \; A_{01} = \begin{pmatrix} \sqrt{2} & 0 \\ 0 & 0 \end{pmatrix}, \; A_{10} = \begin{pmatrix} 0 & 0 \\ 0 & -\sqrt{2} \end{pmatrix}, \tag{3.6}$$

$i, j = 1, 2$ and $v_1 = (1, 1)^T$, $v_2 = (1, -1)^T$. Γ_{12} has energy $\sqrt{2}$, Γ_{21} has energy $-\sqrt{2}$, whereas Γ_{11} and Γ_{22} have energy 0. In the next sections, we will focus on scars with well-defined inversion quantum number, so we define $|\Gamma_I\rangle = (|\Gamma_{11}\rangle - |\Gamma_{22}\rangle)/\sqrt{2 - 2\langle\Gamma_{11}|\Gamma_{22}\rangle}$.

For periodic boundary conditions, the two scarred eigenstates $|\Phi_1\rangle$ and $|\Phi_2\rangle$ are defined as

$$|\Phi_1\rangle = \sum_{\{\sigma\}} \mathrm{Tr}[A_{\sigma_1\sigma_2} \dots A_{\sigma_{L-1}\sigma_L}] \, |\sigma_1\sigma_2 \dots \sigma_{L-1}\sigma_L\rangle \tag{3.7}$$

and $|\Phi_2\rangle = T_x |\Phi_1\rangle$, where T_x is the translation operator. Both have energy 0. Their properties under the symmetries are the following: $I |\Phi_i\rangle = (-1)^{L/2} |\Phi_i\rangle$ and $C_{ph} |\Phi_i\rangle = (-1)^{L/2} |\Phi_i\rangle$ for $i = 1, 2$. We will work with the linear combinations $|\Phi_{K=0,\pi}\rangle = (|\Phi_1\rangle \pm |\Phi_2\rangle)/\sqrt{2 \pm 2\langle\Phi_1|\Phi_2\rangle}$. Even though these are not responsible for the persistent oscillations observed in experiments, their putative stability in the thermodynamic limit outlines their importance.

3.3 Perturbation theory and ETH

It is crucial to understand how to define *stability* for these kind of eigenstates. In general, we will say that an eigenstate of H_0 is stable if it can be deformed to an eigenstate of $H_0 + \lambda V$ with a local unitary transformation in the thermodynamic limit. Usually this criterion is satisfied by ground states in gapped systems. Here we are interested in the scars $|\Gamma_{\alpha\beta}\rangle$ and $|\Phi_i\rangle$ which are in the middle of a dense spectrum, in the absence of a gap to protect them. The local character of the transformation, if it exists, should guarantee that a stable scar retains its character (no ETH and area law entanglement) in the thermodynamic limit. For generic eigenstates, no stability is expected. This can be understood as a consequence of the Eigenstate Thermalization Hypothesis: to first order in the perturbation strength λ, the perturbed eigenstate can be written as

$$|n^0\rangle + \lambda |n^1\rangle = |n^0\rangle + \lambda \sum_{m \neq n} \frac{\langle m^0|V|n^0\rangle}{E_n^0 - E_m^0} |m^0\rangle \, . \tag{3.8}$$

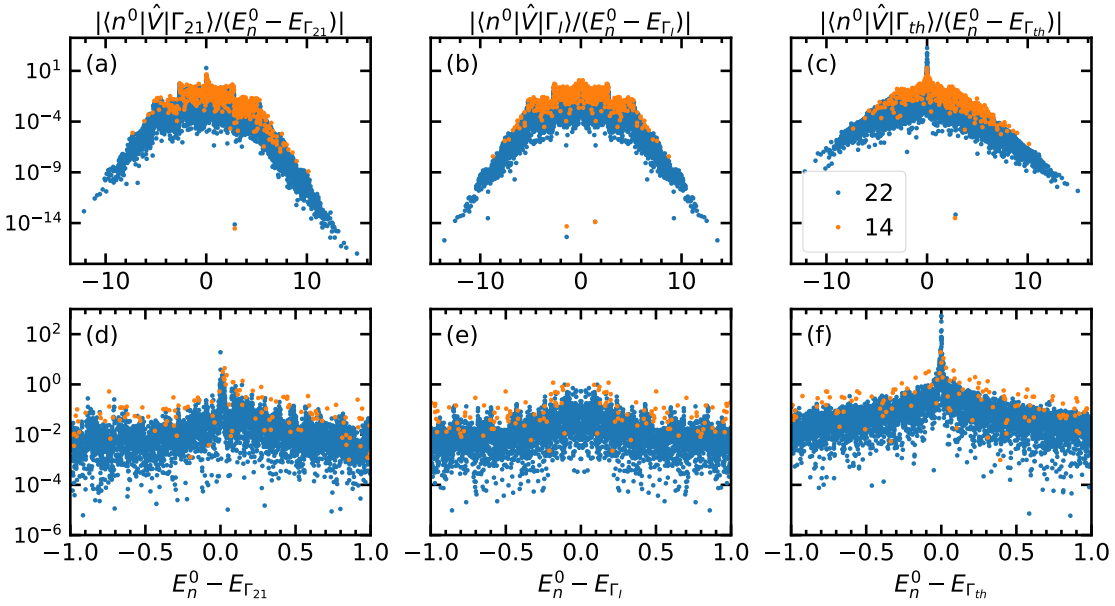

Figure 3.1: Absolute value of the ratio between the matrix element and the energy difference between a target state and a state of the spectrum. The same data are represented in a larger (first row) and in a smaller (second row) range of energy difference. The target states are the scars eigenstates $|\Gamma_{21}\rangle$ (a,d), $|\Gamma_I\rangle$ (b,e) defined in Sec. 3.2 and a thermal eigenstate $|\Gamma_{th}\rangle$ (c,f) taken as the third eigenstate after $|\Gamma_{21}\rangle$ in order of increasing energy. The clear peak observed when a thermal eigenstate $|\Gamma_{th}\rangle$ is considered is not present for the scars eigenstates, pointing at a suppression of the matrix elements of the perturbation for the latter states.

According to ETH, the off-diagonal matrix element $\langle m^0|V|n^0\rangle$ scales as $\exp(-S/2)$, where S is the extensive thermodynamic entropy of the system. The energy denominator, on the other hand, scales as $\exp(-S)$ for nearby eigenstates. This simple argument implies that the first order correction diverges exponentially in the system size L.

Hence, a natural question to answer is whether the first order correction to the scars behaves according to the scaling predicted by ETH or not. In Ref. [64], it was found that the matrix elements $\langle m^0|V|\Gamma\rangle$ averaged over a certain set of eigenstates $\{|m^0\rangle\}$ close in energy to $|\Gamma\rangle$ do indeed scale as $\exp(-S/2)$, where $|\Gamma\rangle$ is one of the scars for the case of open boundary conditions. This is however not sufficient to claim instability: the matrix elements which are responsible for the divergence are the ones involving states that are very close in energy. As can be seen in Fig. 3.1, the matrix elements weighted with the inverse energy gaps behave very differently for the scars and for generic thermal states: the vanishing denominator produces a peak in the case of a thermal state; the scars, despite the vanishing energy gaps, do not exhibit this peak, signalling a suppression of matrix elements for small gaps. Moreover, the averaging procedure of matrix elements introduces some arbitrariness in this respect: the result depends on the choice of the set of eigenstates that are included in the average.

We propose to diagnose the stability of scar eigenstates by studying the fidelity susceptibility, defined as [71]

$$\chi_F\left[|n^0\rangle\right] = \lim_{\lambda\to 0} \frac{-2\ln|\langle n^0|n^\lambda\rangle|}{\lambda^2} \tag{3.9}$$

where $|n^0\rangle$ is an eigenstate of H_0 and $|n^\lambda\rangle$ is the eigenstate of $H_0 + \lambda V$ obtained from

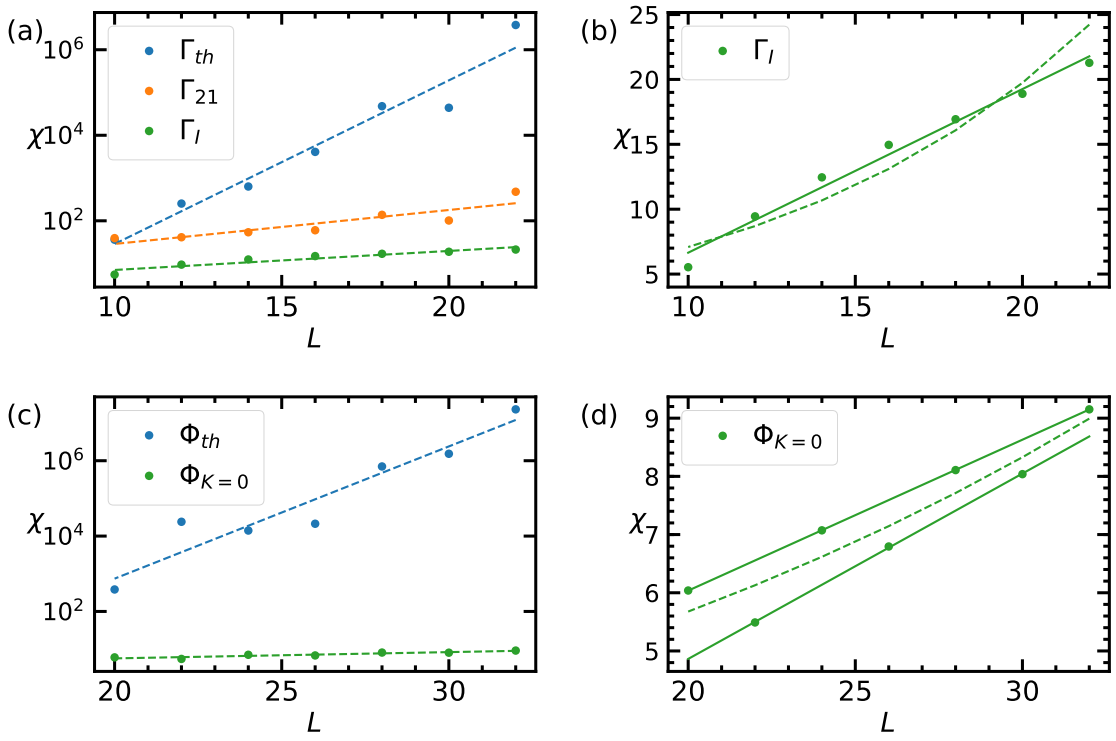

Figure 3.2: Scaling of the fidelity susceptibility with system size. The results shown refer to the states (a) $|\Gamma_{th}\rangle$, $|\Gamma_{21}\rangle$ and $|\Gamma_I\rangle$ with open boundary conditions and to the states (c) $|\Phi_{th}\rangle$ and $|\Phi_{K=0}\rangle$ with periodic boundary conditions. As can be seen in the panels with linear y-scale (b), (d), the scaling of the fidelity susceptibility of a zero energy scar eigenstate is polynomial with the system size, in sharp contrast to what happens for thermal eigenstates or scars at non-zero energy (a),(c). Solid lines are fits for the linear scalings (the two different lines for $\Phi_{K=0}$ capture the even-odd effect), dashed lines are fits for exponential scalings.

$|n^0\rangle$ with a perturbative construction in λ. From the explicit construction of the state, one finds[1]

$$\chi_F\left[|n^0\rangle\right] = \sum_{m\neq n} \left| \frac{\langle m^0|V|n^0\rangle}{E_n^0 - E_m^0} \right|^2 . \tag{3.10}$$

The fidelity susceptibility is a measure of the response of an eigenstate to perturbations: when averaged over different eigenstates, for example, it has been very recently used as a measure of quantum chaos [67, 69]. For gapped ground states of local Hamiltonians, it is expected to scale as $\chi_F \sim L$ with the system size L. On the other hand, as argued above, ETH implies a scaling $\chi_F \sim \exp(L)$ for eigenstates at finite energy density.

Note that, due to the special properties of this perturbation, all the matrix elements of V between zero energy states vanish (see Appendix A.1): as a consequence, the fidelity susceptibility is well-defined even for states in the exponentially degenerate zero-energy manifold and can be computed for all the scarred eigenstates.

We obtain that only a subset of the exact scars appear to be stable. Indeed the scaling of the fidelity susceptibility for the scars $|\Phi_{K=0}\rangle$ (for the case of periodic boundary conditions)

[1] We use that $|n^\lambda\rangle = (|n^0\rangle + |n_\perp\rangle)/\||n^0\rangle + |n_\perp\rangle\|$, with $\langle n_\perp|n^0\rangle = 0$ to obtain $\langle n^0|n^\lambda\rangle = \||n^0\rangle + |n_\perp\rangle\|^{-1} = (1 + \langle n_\perp|n_\perp\rangle)^{-1/2} = 1 - \frac{1}{2}\lambda^2 \langle n^1|n^1\rangle + O(\lambda^3)$.

and $|\Gamma_I\rangle$ (for the case of open boundary conditions) shown in Fig. 3.2 suggests a linear dependence[2] $\chi_F \sim L$, as evidenced by the solid lines. On the contrary, the scaling for $|\Gamma_{21}\rangle$ and for the generic thermal eigenstates $|\Gamma_{th}\rangle$ and $|\Phi_{th}\rangle$[3] are compatible with an exponential growth (dashed lines), as predicted by ETH. These results show that $|\Phi_{K=0}\rangle$ and $|\Gamma_I\rangle$ are perturbatively stable to an infinitesimal perturbation. We note that these differences are not only qualitatively manifest (power versus exponential scaling), but also quantitatively striking, so that the different scaling regimes can be diagnosed despite the fact that our analysis is limited to modest system sizes up to $L = 32$ spins.

We now want to understand if they are also stable to a finite strength λ of the perturbation. If these states were akin to gapped ground states, we would have expected stability to hold in the thermodynamic limit for a finite λ as long as it is much smaller than the gap. The absence of a gap makes the quest for an energy scale associated with scars much less obvious.

To address this problem, we compute the states $|\Phi^{\lambda}_{K=0}\rangle$ and $|\Gamma^{\lambda}_{i}\rangle$ obtained by perturbing the scars $|\Phi_{K=0}\rangle$ and $|\Gamma_I\rangle$ in the following way

$$|\Phi^{\lambda}_{K=0}\rangle = \frac{1}{\mathcal{N}^{\lambda}_{\Phi}} \frac{1}{1 + \lambda Q H_0^{-1} Q V} |\Phi_{K=0}\rangle \tag{3.11}$$

$$|\Gamma^{\lambda}_{I}\rangle = \frac{1}{\mathcal{N}^{\lambda}_{\Gamma}} \frac{1}{1 + \lambda Q H_0^{-1} Q V} |\Gamma_{I}\rangle \tag{3.12}$$

where Q projects on the subspace with $E_0 \neq 0$, and $\mathcal{N}^{\lambda}_{\Phi}$, $\mathcal{N}^{\lambda}_{\Gamma}$ are normalizing factors. The states $|\Phi^{\lambda}_{K=0}\rangle$ and $|\Gamma^{\lambda}_{I}\rangle$ are the perturbed eigenstates to infinite order in perturbation theory. We numerically compute the von Neumann bipartite entanglement entropy $S(\lambda)$ of these states for different system sizes (Fig. 3.3). This quantity exhibits peaks that get closer to $\lambda = 0$ as L increases, indicating a stronger and stronger hybridization with other eigenstates in the spectrum. This fact strongly suggests that, despite the stability observed to first order in perturbation theory, the scars are ultimately not stable for finite $\lambda \neq 0$ [4].

3.4 Models with radius of constraint $\alpha > 1$

Since the first studies on the PXP model, several other instances of quantum many-body scars have been put forward [72–88]. While it is tempting to extend some of the findings above to a general setting, we refrain from this for the very simple reason that PXP models have a characteristic feature - a constrained Hilbert space that cannot be reduced in tensor product form - that is not present in other instances of quantum scars. We pursue instead an alternative route, based on investigating the stability of quantum scars in an enlarged class of constrained models.

In concrete, we consider a generalization of the PXP model, where we extend the constraint to the sites within an integer radius α, i.e. $n_i n_j = 0$ whenever $|i - j| \leq \alpha$, with

[2] On top of the linear growth, the scaling for the scar $|\Phi_{K=0}\rangle$ is subject to an even-odd effect related to the different parity under inversion symmetry of the state ($I = (-1)^{L/2}$).

[3] The state $|\Gamma_{th}\rangle$ is chosen as the third eigenstate after $|\Gamma_{21}\rangle$ in increasing order of energy. The state $|\Phi_{th}\rangle$ is the state with energy closest to -0.3.

[4] We note that performing a rigorous finite-size scaling analysis for the position of the first peak versus system size is tricky for two reasons: *(i)* we can only consider a coarse grained set of values of λ, so that we can only put an upper bound on the position of the peak, and *(ii)* the peaks may be due in principle to different level crossing, making a finite-size extrapolation not fully reliable. Our conclusion is based on the fact that we systematically observe the peak moving towards vanishing perturbations, with no exception, very rapidly with system size.

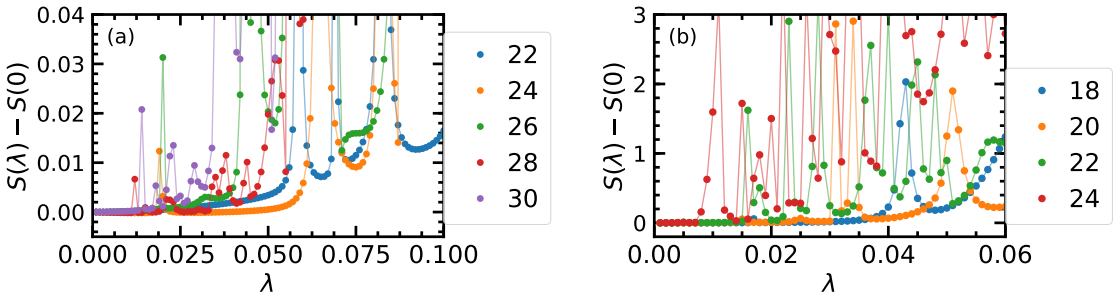

Figure 3.3: Bipartite entanglement entropy of the states (a) $|\Phi^{\lambda}_{K=0}\rangle$ and (b) $|\Gamma^{\lambda}_{I}\rangle$ as a function of λ. Peaks in this quantity signal hybridization of the perturbed state with thermal eigenstates. By increasing the system size, we find peaks closer and closer to $\lambda = 0$, suggesting that the scar eigenstates are not stable in the thermodynamic limit.

$n_j = \frac{Z_j+1}{2}$. The Hamiltonian has the form:

$$H_0^{\alpha} = \sum_i P_{i-\alpha} \dots P_{i-1} X_i P_{i+1} \dots P_{i+\alpha}, \tag{3.13}$$

where P_j is the projector on the state $|0\rangle$. The Hamiltonian (3.13) coincides with the PXP model for $\alpha = 1$ and arises as an effective approximation of the long-range Hamiltonian describing Rydberg atoms arrays when the (continuous) blockade radius is increased (by e.g. tuning the distance between the atoms). Similarly to the PXP model, this Hamiltonian commutes with the reflection symmetry I and anticommutes with the particle-hole symmetry C_{ph}, and the spectrum has the same properties (see Appendix A.1).

3.4.1 Exact scars with $E = 0$

We now show that, although the models considered here satisfy the Wigner-Dyson spectral statistics, some states in the spectrum have finite entanglement entropy in the thermodynamic limit and hence violate the eigenstate thermalization hypothesis.

For a system with $L = (\alpha + 2)n$ (with n integer), consider the following state

$$|\phi_\alpha\rangle = \bigotimes_{i=0}^{n-1} \left[(|01\rangle - |10\rangle) \underbrace{|0 \dots 0\rangle}_{\alpha} \right]_{b_i} \tag{3.14}$$

where the index b_i labels blocks of $\alpha + 2$ sites. The state of the first two sites of a block is an antisymmetric superposition (that we call a *dimer*) and hence is annihilated by the spin flip. All the other sites of a block cannot be flipped: they are "frozen" by the previous or the next dimer. Therefore, the state $|\phi_\alpha\rangle$ (and all the states obtained from it by translations) is a scar with energy $E = 0$ for generic $\alpha > 1$.

We can construct many exact scars with $E = 0$ by placing dimers (depicted in red in Fig. 3.4) on the chain. Two dimers must be separated by a number ℓ of zeros in the range $\alpha \leq \ell \leq 2\alpha - 2$. We can also have longer-range dimers involving sites that are not nearest neighbours. In this case, the number ℓ of zeros between two dimers of range r_1 and r_2 must be in the interval $\alpha \leq \ell \leq 2\alpha - r_1 - r_2$. This last condition implies that the ranges of two consecutive dimers are bounded by $r_1 + r_2 \leq \alpha$.

This construction works also in the case of open boundary conditions, with the following rules for the boundaries: if the first (last) dimer of the chain has range r, then the number of zeros preceding (following) it must be $\ell \leq \alpha - r$.

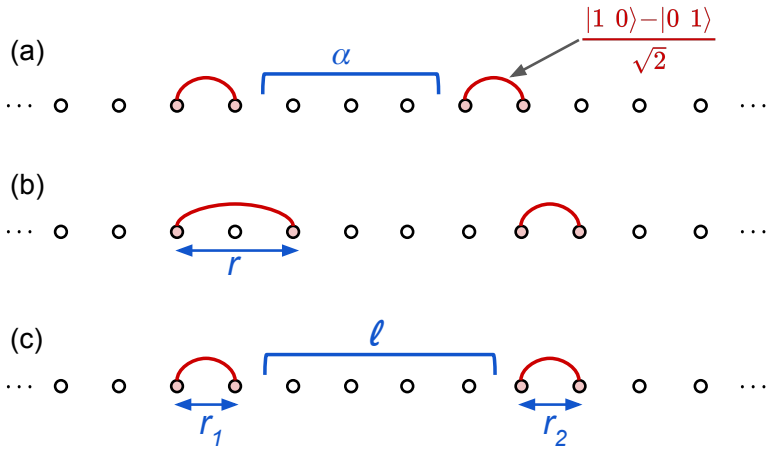

Figure 3.4: Some eigenstates with $E = 0$. (a) The state $|\phi_\alpha\rangle$ is made of dimers (in red) separated by sequences of 0s of length α. (b) Dimers can have range $r > 1$. (c) Dimers can be separated by any distance ℓ, such that $\alpha \leq \ell \leq 2\alpha - r_1 - r_2$.

We note that the structure of these states, that we write as product states of dimers, is reminiscent of the construction of scar eigenstates found in other constrained models [84, 89].

3.4.2 Exact scars with $E \neq 0$

In the following, we will show that the models of Eq. (3.13) have scars also at $E \neq 0$ when open boundary conditions are imposed. While, as we have shown in Sec. 3.4.1, it is possible to write many exact $E = 0$ eigenstates as product states of dimers, for these scars we need to resort to a more involved construction: we write them as matrix product states with finite bond dimension, independent of the system size.

Exact scars with $E = \pm\sqrt{3}$

For system sizes $L = (\alpha+2)n+3$, with n integer, we are able to write two exact scars with energy $E = \pm\sqrt{3}$ as matrix product states. To define these states, we divide the chain in blocks labelled from 1 to $2n+1$: the blocks labelled by odd numbers contain 3 sites, while the blocks labelled by even number contain $\alpha - 1$ sites. As we prove in Appendix A.4, the following state is an exact eigenstate with energy $E = \sqrt{3}$:

$$|\psi_\alpha^{(3)}\rangle = \sum_{\vec{s}} \left[(1,0)^T \cdot N^{s_1} M^{s_2} \dots M^{s_{2n}} N^{s_{2n+1}} \cdot (0,1)\right] |\vec{s}\rangle \tag{3.15}$$

where $s_1, s_2, \dots, s_{2n+1}$ label the states of the blocks and

$$M^s = \begin{cases} 1 & \text{if } s = 00\dots00 \\ 0 & \text{otherwise,} \end{cases} \tag{3.16}$$

$$N^{000} = \begin{pmatrix} 0 & \sqrt{3} \\ 0 & 0 \end{pmatrix}, \qquad N^{100} = \begin{pmatrix} 0 & 1 \\ 0 & 1 \end{pmatrix}, \tag{3.17}$$

$$N^{010} = \begin{pmatrix} 1 & 1 \\ 0 & -1 \end{pmatrix}, \qquad N^{001} = \begin{pmatrix} -1 & 1 \\ 0 & 0 \end{pmatrix}. \tag{3.18}$$

From the relation $C_{ph}H_0^\alpha = -H_0^\alpha C_{ph}$ we immediately find that the state $|\psi_\alpha^{(-3)}\rangle = C_{ph}\,|\psi_\alpha^{(3)}\rangle$ is another eigenstate of H_0^α with eigenvalue $E = -\sqrt{3}$.
We also note that the state obtained by taking the trace in Eq. (3.15) is a zero energy eigenstate for $L = (\alpha+2)n+3$ when open boundary conditions are imposed. Moreover, removing the matrix N at one of the two boundaries we can construct an MPS that is invariant under translations of $\alpha+2$ sites

$$|\varphi_\alpha\rangle = \sum_{\vec{s}} \mathrm{Tr}(B^{s_1}B^{s_2}\dots B^{s_n})\,|\vec{s}\rangle\,, \tag{3.19}$$

where $B = MN$ and s_i runs through the 3 allowed states of the i-th block, made of $\alpha+2$ sites. This state is a zero energy eigenstate for periodic boundary conditions and system sizes $L = (\alpha+2)n$, and it has non-vanishing overlap with the dimer eigenstates of Sec. 3.4.1; however, for generic α it has a component that is independent of those states. The matrix B yields a non-injective MPS, whose parent Hamiltonian has a degenerate groundspace [90]. In fact, the state in Eq. (3.19) can be written as a cat state

$$\begin{aligned}|\varphi_\alpha\rangle = &\left[\left(|L\rangle + \frac{1}{2}|R\rangle - \frac{3}{2}|C\rangle\right)|\underbrace{0\dots0}_{\alpha-1}\rangle\right]^{\otimes n}\\ &+\left[\left(\frac{1}{2}|L\rangle + |R\rangle - \frac{3}{2}|C\rangle\right)|\underbrace{0\dots0}_{\alpha-1}\rangle\right]^{\otimes n}\\ &= |\varphi_\alpha^1\rangle + |\varphi_\alpha^2\rangle\,,\end{aligned} \tag{3.20}$$

where $|L\rangle = |100\rangle$, $|C\rangle = |010\rangle$ and $|R\rangle = |001\rangle$. The parent Hamiltonian of this state have $|\varphi_\alpha^1\rangle \pm |\varphi_\alpha^2\rangle$ as the two degenerate ground states. This is in contrast with the eigenstates of Ref. [63] ($|\Phi_1\rangle$ and $|\Phi_2\rangle$ in Sec. 3.2) which are injective MPSs, and thus unique ground states of their parent Hamiltonian.

Exact scars with $E = \pm\sqrt{q}$

We find that other (possibly degenerate) MPS scars appear at energies $E = \pm\sqrt{q}$ with q integer. This property is a consequence of the structure of these matrix product states. Similarly to the case of periodic boundary conditions, the action of the Hamiltonian on these states is such that the complicated interaction is decoupled into smaller non-interacting blocks. Their energies are therefore determined by the energy of a single block: in the cases we consider, the energy of a block can be 0 or $\pm\sqrt{q}$ where $q \leq \alpha+1$ is the size of the block. In Appendix A.5 we write down explicitly some exact eigenstates of H_0^α with energy $E = \pm\sqrt{2}$ for $\alpha = 3$.

3.4.3 Relation with exact scars for $\alpha = 1$

The exact scars described here are reminiscent of the ones found in Ref. [63]: there, it was shown that the PXP model ($\alpha = 1$) has exact MPS scars at $E = 0$ for periodic boundary conditions, and both at $E = 0$ and $E = \pm\sqrt{2}$ when open boundary conditions are imposed. The states we study for $\alpha \geq 2$, however, show a qualitative difference with respect to them: in the case of open boundary conditions, the energy density profile does not have peaks at the edges, but has a pattern that is uniformly repeated in the full system. This can be understood from the MPS structure of these states. The scars in Eq. (3.5) have the

form of AKLT states in which two-site blocks play the role of $S = 1$ spin variables. As we show in Appendix A.3, the energy density of the PXP model corresponds to the local magnetization of the AKLT state in the z direction. The boundary properties of the scars can be interpreted using the "dilute antiferromagnet" representation of the AKLT state: in the S_z basis, the state is a superposition of configurations with alternating $+$ and $-$, and with an arbitrary number of 0 placed in between. The different boundary vectors α, β of $|\Gamma_{\alpha\beta}\rangle$ fix the sign of the first and last non-zero spins of the configurations. Therefore, the local magnetization is non-zero close to the boundaries but goes to 0 far from them. The state in Eq. (3.15), on the other hand, has a very different structure: if we use, once again, a basis in which the local energy corresponds to a local magnetization, we can write $|\psi_\alpha^{(3)}\rangle$ as a superposition of configurations with a single $+$ (on one of the 3-site blocks), and 0 magnetization everywhere else. Therefore, in contrast with the dilute antiferromagnet of the scars $|\Gamma_{\alpha\beta}\rangle$, this state is reminiscent of a spin wave, with a single magnetic excitation uniformly spread in the chain.

3.4.4 Stability

We now analyse the response of the exact scars described above to a perturbation. The perturbation we apply is

$$V^\alpha \;=\; \sum_i Z_{i-\alpha-1}P_{i-\alpha}\dots P_{i-1}X_iP_{i+1}\dots P_{i+\alpha} \;+\; P_{i-\alpha}\dots P_{i-1}X_iP_{i+1}\dots P_{i+\alpha}Z_{i+\alpha+1}. \tag{3.21}$$

This term has the same symmetries of H_0^α, namely it commutes with I and anticommutes with C_{ph}. Similarly to the PXP case, we use the fidelity susceptibility to check whether these states are stable to first order in perturbation theory.

In Fig. 3.5, we present the results of the stability analysis. In the upper left panel, we plot the fidelity susceptibility of a generic (thermal) eigenstate of the spectrum $|\phi_{th}\rangle$ (chosen as the eigenstate with energy closest to $1.9, 1.7, 1.35$ for $\alpha = 2, 3, 4$ respectively): for every α, the scaling with system size is exponential, as expected from ETH (dashed lines). In the other panels, we plot instead the fidelity susceptibility of the scars $|\phi_\alpha\rangle$ defined in Eq. (3.14): the scaling here is linear[5] (solid lines) for every α, signalling a clear violation of ETH. These results suggest that the anomalous stability of the scars with $E = 0$ is a generic feature of this class of one-dimensional models constrained by Rydberg blockade.

3.5 Conclusions

In this section, we investigated the stability against perturbations of exact quantum scars arising in spin chains constrained by Rydberg blockade. We first analysed the PXP model and found that some of the MPS scars found in Ref. [63] exhibit a power law scaling of the fidelity susceptibility with system size. This result is a signature of their stability, a remarkable feature for eigenstates in the middle of a dense many-body spectrum. This fact is however limited to first order in perturbation theory, as a numerical analysis of the higher-order perturbative corrections reveals hybridization of exact scars eigenstates with thermal eigenstates. This behavior is reminiscent of the many-body "dark states" observed in Ref. [91, 92]. We find the anomalous scaling of the fidelity susceptibility only

[5]Similarly to the state $|\Phi_{K=0}\rangle$ in Fig.3.2-(d), the scaling for $|\phi_\alpha\rangle$ is subject to an even-odd effect related to the different parity under inversion symmetry ($I = (-1)^{L/(\alpha+2)}$).

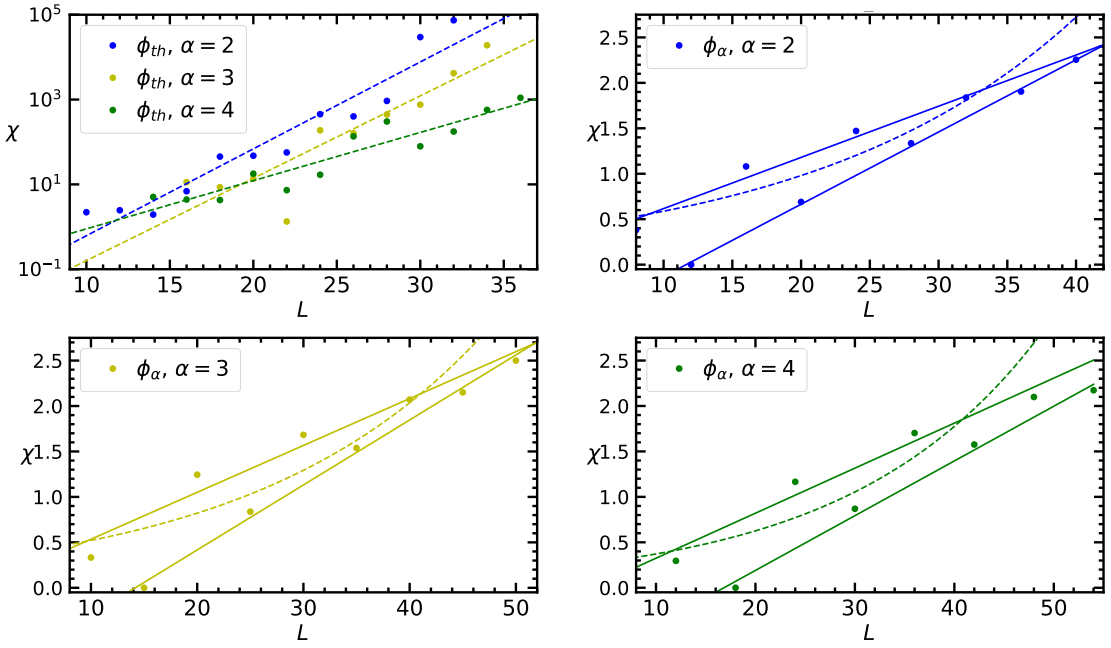

Figure 3.5: Scaling of the fidelity susceptibility with system size. The results shown refer to the generic states ϕ_{th} (upper left panel) and the scarred eigenstates ϕ_α (upper right panel and lower panels). Dashed lines are obtained from fits with an exponential scaling, solid lines with linear scaling. The result points at the same behavior occuring in the PXP model.

for scars with zero energy, suggesting that the properties of the $E = 0$ subspace, such as the exponential degeneracy enforced by the invariance of this subspace under particle-hole and inversion symmetries, may be a key factor in stabilizing these states. Although not shown here, if we perturb with a term that breaks these properties, we find no signatures of stability for any of these low-entropy eigenstates.

To validate these conclusions, we extended our discussion to models with larger blockade radius α. First, we constructed novel classes of states that are exact scars eigenstates for any α and have energy eigenvalues $E = 0$ and $E = \pm\sqrt{q}$ (with q integer). The construction is based on an effective decoupling of the sites of the chain into "non-interacting blocks", and allows us to write these states into simple matrix product form. We then studied their fidelity susceptibility under perturbations that do not spoil the exponential degeneracy of the zero-energy eigenspace, a common property of the family of constrained models we analysed. Also in this case, we found these eigenstates to be stable at first perturbative order when they belong to the $E = 0$ subspace.

Our results suggest that an increasing number of exact MPS scars appear in the spectrum for larger values of α, and their complete classification is beyond the scope of this work. It is also worth noticing that, contrarily to the $\alpha = 1$ case (PXP model), no "approximate scars" eigenstates – akin to the ones found in Ref. [27] – appear for $\alpha > 1$, as can be seen from an inspection of the bipartite entanglement entropy of each eigenstate as a function of the energy. This fact provides strong indications that there is, in general, no relationship between the appearance of eigenstates with low entanglement entropy, equally spread uniformly in the energy spectrum, and the existence of exact MPS eigenstates in spin models constrained by Rydberg blockade. It stands as an open question whether these new exact MPS states can lead to clear experimental signatures, since, having no recur-

rent spectral structure, they are not expected to play any role in anomalous oscillations observed in experiments (that, indeed, were not reported for larger constraint radii).

From a methodological standpoint, our results suggest that generalizations of the fidelity susceptibility to spectral properties can provide useful quantitative insights on the stability of ETH, in agreement to recent applications to quantum chaos diagnostics proposed in Ref. [67, 69].

Chapter 4

Constraint-induced delocalization

Locating and characterizing the MBL transition is notoriously difficult. For the most studied system which shows MBL, the disordered XXZ spin chain, the maximal system size accessible to present day supercomputers for an exact treatment is $L = 24$ [93–96]. On top of that, the observed finite-size scaling is slow. The ensuing difficulties in extrapolating results to the thermodynamic limit sparkled a recent debate about the existence of the MBL phase [97–100] and its dynamical properties [101–103]. In parallel to these theoretical efforts, experiments in the synthetic quantum matter have already probed regimes of strong interactions and strong disorder necessary for MBL in both Ising- and Hubbard-type models [4, 104]. Very recently, a new generation of platforms based on Rydberg atoms in optical lattices and tweezers [12, 15, 58, 59, 105] has demonstrated an impressive capability to perform coherent dynamics up to considerably long timescales, allowing, for instance, for the realization of mesoscopic-sized ordered states [106, 107]. Strong nearest-neighbor interactions that characterize these systems naturally lead to effective constrained dynamics in both Ising- and XY-type regimes. A natural question to ask is thus, whether the interplay between constraints, interactions and disorder can lead to a scenario that is qualitatively different from the unconstrained models, and whether such a scenario can be characterized by common, generic features.

In this chapter, we show that 1D spin chains with local constraints can remain ergodic even in the presence of a strong disorder. Such models are experimentally realized in arrays of ultracold Rydberg atoms [12, 15, 58, 59, 105]. The local constraints arise in the Rydberg blockade regime and alleviate the exponential growth of Hilbert space with the system size L. This feature allows us to overcome the limitation of small system sizes that impede studies of the MBL transition in the conventional, unconstrained spin chains and to consider constrained models of sizes exceeding $L = 100$ sites for the largest constraint radius considered.

Investigating the crossover between ergodic and MBL regimes, we see no signs of localization in the thermodynamic limit. We identify the reason for this behavior in a non-trivial action of a "quenched disorder" term in a constrained model. Such a term does not simply act as an on-site disorder on the basic excitations of the clean system, but between them: in a representation in which the basic degrees of freedom of the system are *unconstrained*, the quenched disorder term is written as both a random on-site energy term and a random density-density interaction. Both terms are of the same order and their interplay does not allow the system to be in a strong disorder, weak interaction regime in which MBL can be established in a controlled manner [41]. Focusing on models that are motivated by the aforementioned experiments, we believe that this observation extends to a broad class of constrained models.

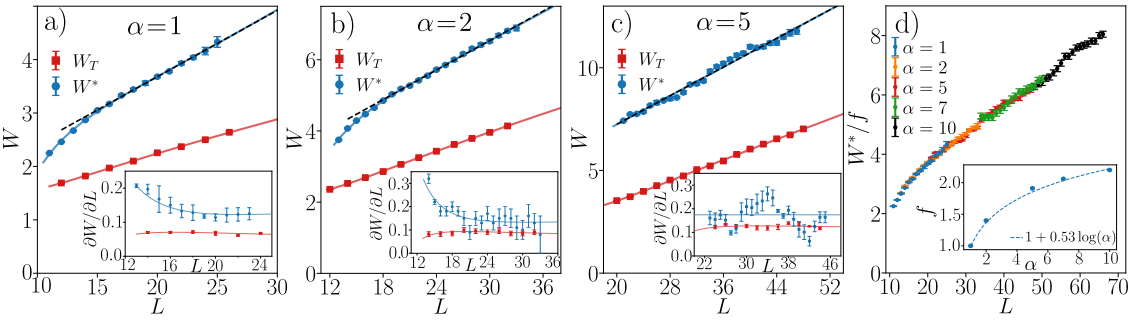

Figure 4.1: The ergodic-MBL crossover in disordered PXP (4.1) models. Panels a)-c): disorder strengths W_T and W^* as function of system size L. Solid lines denote fits of the form $W(L) = aL + b + c/L + d/L^2$ (both for $W_T(L)$ and $W^*(L)$), dashed lines correspond to $W^*(L) = aL + b$. The insets show derivatives of data with respect to L. Panel d) shows $W^*(L)$ rescaled by a factor f, obtained by minimizing the distance between the $W^*(L)/f$ curves for varying radius of constraint α.

4.1 Disordered PXP models

We consider a 1D chain of Rydberg atoms in the frozen regime and assume that strong interactions allow the excitation to Rydberg state only for pairs of atoms separated by at least α sites [12, 15, 57–59]. This leads to the Hamiltonian

$$\hat{H} = \sum_{i=1}^{L} P_i^{\alpha} S_i^x P_{i+1+\alpha}^{\alpha} + \sum_{i=1}^{L} h_i S_i^z \tag{4.1}$$

expressed in terms of the spin operators $\boldsymbol{S}$, where the projectors $P_i^{\alpha} = \prod_{j=i-\alpha}^{i-1}(1/2 - S_j^z)$ assure that the dynamics is confined to a constrained Hilbert space, h_i are independent, uniformly distributed random variables in the interval $[-W/2, W/2]$ with W being the disorder strength and with periodic boundary conditions (PBC) $\boldsymbol{S}_{L+i} \equiv \boldsymbol{S}_i$ assumed.

The clean ($h_i = 0$) PXP models are known to host many-body scar states for a constraint radius $\alpha = 1$ [108–116] as well as for $\alpha \geq 1$ as discussed in the previous chapter and even in presence of disorder [117]. The scar states are, however, not statistically important for the properties of generic eigenstates that are of direct interest here. On the other hand, for a PXP model with disorder on both the S^x and S^z terms, both an ergodic and an MBL regimes were claimed to exist [118]. That was interpreted in favour of a stable MBL phase at large disorder strengths. For the blockade radius α, the Hilbert space dimension is $\mathcal{H}_d^{\alpha}(L) = (d_{\alpha})^L$ where $d_{\alpha} \approx 1.6180, 1.4656, 1.2852$ respectively for $\alpha = 1, 2, 5$. This allows us to access progressively larger system sizes with increasing α while studying the crossover between ergodic and MBL regimes. Similar ideas, employing local constraints to access larger volumes, were used to demonstrate a presence of MBL regime in 2D dimer systems [119, 120] and to study MBL in Krylov spaces of a pair-hopping model [121].

4.2 Ergodic-MBL crossover in PXP models

We calculate eigenvalues E_i and eigenstates of disordered PXP models (4.1) for $\alpha = 1, 2, 5$ using full exact diagonalization for system sizes L for which the Hilbert space dimension $\mathcal{H}_d \leq 10^4$ and POLFED algorithm [95] for larger L. We compute $r_i = \min\{g_i, g_{i+1}\}/\max\{g_i, g_{i+1}\}$ (where $g_i = E_{i+1} - E_i$), average it over $\min\{\mathcal{H}_d/20, 1000\}$ of the eigenvalues from the middle of the spectrum and subsequently average the results over disorder realizations to obtain

the average gap ratio $\overline{r}$. The number of disorder realizations varies between a few millions for the smallest L down to no less than 2000 (5000) for the largest (second largest) system size L considered for a given model. The average gap ratio $\overline{r}$ reflects properties of level statistics changing between $\overline{r}_{GOE} \approx 0.53$ for an ergodic system and $\overline{r}_{PS} \approx 0.386$ for a localized system [122]. Indeed, for small disorder strengths W the average gap ratio in the considered models is $\overline{r} = \overline{r}_{GOE}$, and it decreases to $\overline{r} \approx \overline{r}_{PS}$ for large W, see Appendix B.

To investigate the crossover between the ergodic and MBL regimes we introduce two system-size dependent disorder strengths: i) $W_T(L)$ – the disorder strength for which, at a given system size L, the average gap ratio starts to deviate from the ergodic value and is equal to $\overline{r}_{GOE} - p$ (we choose $p = 0.01$ but other choices of $0.005 < p < 0.02$ lead to quantitatively similar results); ii) $W^*(L)$ – the disorder strength for which curves $\overline{r}(W)$ cross for system sizes L_1 and L_2 such that $L = (L_1 + L_2)/2$, we use $2 \leq |L_1 - L_2| \leq 4$ for $\alpha = 1, 2$ and $4 \leq |L_1 - L_2|$ for $\alpha \geq 5$ (see Appendix B).

The resulting $W_T(L)$ and $W^*(L)$ curves divide the phase diagram into three regimes: ergodic for $W < W_T(L)$ with $\overline{r}(W) = \overline{r}_{GOE}$; "critical" for $W_T(L) < W < W^*(L)$ in which the value of $\overline{r}(W)$ increases with system size L towards $\overline{r}_{GOE}$; MBL for $W > W^*(L)$ in which, for system sizes smaller than L, the average gap ratio $\overline{r}(W)$ decreases down to $\overline{r}_{PS}$ with increase of system size.

For the widely studied disordered XXZ model [42, 123–133], one observes the scalings $W_T(L) \sim L$ and $W^*(L) \sim W_C + c/L$ [95]. Extrapolating the scaling $W^*(L) \sim W_C + c/L$ to $L \to \infty$, one gets a critical disorder strength $W_C \approx 5.4$, slightly larger than the usually cited value $W_C \approx 3.7$ [125] but consistent with various lower bounds [134–136]. At the same time, the two scalings $W_T(L) \sim L$ and $W^*(L) \sim W_C + c/L$ become incompatible for system sizes larger than $L_0 \approx 50$ (a length scale which appeared before, for this model [100]). The asymptotic regime $L > L_0$ is well beyond reach of present day supercomputers for XXZ model, hence evidence for either of the scalings to prevail in the thermodynamic limit is lacking. We show below that the situation is much clearer for disordered constrained models.

For disordered PXP models we observe a linear dependence $W_T(L) \sim L$ as shown in Fig. 4.1 (a-c). The disorder strength $W^*(L)$, describing the drift of the crossing point with system size, shows a clear curvature at small L suggesting the $W^*(L) \sim W_C + c/L$ scaling. However, for $L \gtrapprox 20$ for $\alpha = 1$ ($L \gtrapprox 22$ for $\alpha = 2$) this curvature vanishes and $W^*(L)$ starts to grow linearly with the system size L. see Fig. 4.1(a-b). Importantly, for $\alpha = 2$ the interval of system sizes for which the linear drift $W^*(L) \sim L$ is observed is wider than for $\alpha = 1$. Increasing the radius of the blockade further, to $\alpha = 5$, we still see – Fig. 4.1 c) – a linear dependence $W_T(L) \sim L$. The curvature of the $W^*(L)$ curve, observed for smaller system sizes disappears for $\alpha = 5$. Instead, we observe a linear drift $W^*(L)$ with a small oscillation on top of it for all available system sizes.

These conclusions are further supported by the derivatives $\partial W_T/\partial L$, $\partial W^*/\partial L$ shown in the insets of Fig. 4.1. The derivative $\partial W_T/\partial L$ clearly approaches a constant w_T with the increasing system size. The derivative $\partial W^*/\partial L$ decreases with L for $\alpha = 1, 2$, oscillates around a constant for $\alpha = 5$ and is bound from below by $\partial W_T/\partial L$. This is consistent with a linear drift of the both disorder strengths $W_T(L) \sim w_T L$ and $W^*(L) \sim w^* L$ with $w_T \leq w^*$ at sufficiently large L (see also [137]). A similar analysis can be performed for entanglement entropy with the same conclusions.

Superimposing results for various constraint radius α as shown in Fig. 4.1 d), we observe that they fall on top of a universal curve if the crossing points $W^*(L)$ are rescaled by factor f that increases approximately logarithmically with α. This is surprising: one could expect that the larger α implies smaller number of spin flips for a given spin configuration

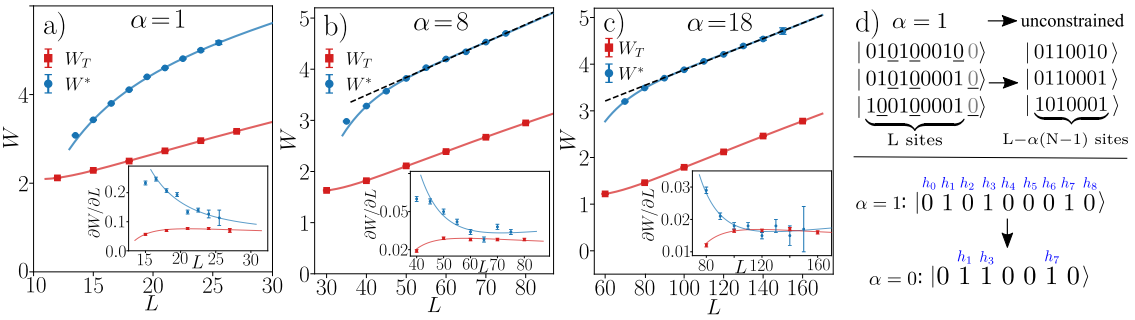

Figure 4.2: The ergodic-MBL crossover in disordered constrained models with $U(1)$ symmetry (4.2). Panels a)-c): disorder strengths W_T and W^* as function of system size L. Panel d) (top): the mapping between constrained and unconstrained models: α unoccupied sites added after the right end of the chain are denoted in gray, the underlined sites are joined to the neighboring particles to form the particles of the unconstrained model. Panel d) (bottom) the potential felt by the particles before and after the mapping.

enhancing localization in the system. In fact, exactly the opposite is true. To see that, consider a spin configuration with maximal number of spins up for given α which is roughly equal to $L/(1+\alpha)$. To perform a transition to a spin configuration with all spins up shifted by one lattice site, it suffices to act $2L/(1+\alpha)$ times with the kinetic term of the Hamiltonian (4.1). Hence, the kinetic term becomes more effective with increasing radius of constraint favoring delocalization at larger α (see also Appendix B). However, this is not the ultimate reason of why we observe delocalization in the constrained models as we show below.

A constrained model with $U(1)$ symmetry. Consider a system of spinless fermions with Hamiltonian

$$H = \sum_{i=1}^{L} P_i \left(c_i^\dagger c_{i+1} + c_{i+1}^\dagger c_i \right) P_{i+2+\alpha} + \sum_{i=1}^{L} h_i n_i \tag{4.2}$$

where $c_i^\dagger$ (c_i) are fermionic creation (annihilation) operators, the particle number operator is $n_i = c_i^\dagger c_i$, the projectors $P_i^\alpha = \prod_{j=i-\alpha}^{i-1}(1-n_j)$ assure that the particles are separated by at least α sites, h_i are independent, uniformly distributed random variables in the interval $[-W/2, W/2]$ and PBC are imposed. The model (4.2) maps, via the Jordan-Wigner transformation, to model analogous to disordered PXP model (4.1) with S_i^x replaced by a spin-flip term $S_i^x S_{i+1}^x + S_i^y S_{i+1}^y$ in the kinetic term. Hence, (4.2) is a natural extension of the constrained model (4.1) that has the $U(1)$ symmetry and preserves the total magnetization $S^z = \sum_{i=1}^{L} S_i^z$ (or equivalently, the total number of particles $N = \sum_{i=1}^{L} n_i$). We consider a filling $N/L = 1/(\alpha+2)$. The model (4.2) (for $\alpha = 1$) can be viewed as a strong interaction limit of XXZ spin chain [138] (We note that, differently from Ref. [138], we are interested solely in the regime with the constrains exactly satisfied) and may be realized experimentally by Rydberg dressing technique [105, 139–142].

In contrast to the PXP models, the kinetic term of the constrained model (4.2) does not become more effective when the constraint radius α is increased. Indeed, due to the particle number conservation, roughly $L/2$ actions of the kinetic term are needed to reach an arbitrary Fock state from a given starting Fock state (see also Appendix B). Based on the argument above, one could then expect that the constrained models with $U(1)$ symmetry are much more prone to localization. This, however, turns out not to be the case, as revealed by an analysis of the crossover in the average gap ratio $\overline{r}$ between the ergodic and MBL regimes. The disorder strengths $W_T(L)$ and $W^*(L)$, shown in Fig. 4.2 a)-c) are

similar to the results for the disordered PXP models. The boundary of the ergodic regime $W_T(L)$, behaves linearly in L, $W_T(L) \sim w_T L$. The boundary of the MBL regime, $W^*(L)$, shows some curvature at smaller L but then approaches a linear behavior $W^*(L) \sim w^* L$, with slope $w^* \geq w_T$. Hence, the whole crossover between ergodic and MBL regimes drifts linearly with L towards increasing disorder strengths and the systems delocalize in the thermodynamic limit.

4.3 On-site disorder in presence of constraints

To understand the delocalization of the constrained models, let us reconsider the Hamiltonian (4.2), and assume open boundary conditions (OBC) for simplicity. The presence of constraints prevents the particles from approaching each other at a distance smaller than α. Hence, it is possible to associate an *excluded volume* of α sites with each of the particles (for instance to the right of the particle). Then, by adding α unoccupied sites at the right end of the chain, one can replace each particle and α sites to its right, by an occupied site of a new, smaller chain. This shrinking procedure, illustrated in Fig. 4.2 d), defines a one-to-one mapping between Fock states of system of L sites with constraint of radius α and between Fock states of an *unconstrained* system of spinless fermions on $L - \alpha(N-1)$ sites. Moreover, the particles can hop in the same manner before and after the mapping (if a given particle cannot hop, say, to the right in the constrained model due to a presence of another particle α sites to its right, it also cannot hop to the right in the unconstrained model since the neighboring site is occupied). This means that in the absence of disorder ($h_i = 0$), the Hamiltonian of the model (4.2) for N particles on L sites with constraint radius α and OBC exactly coincides with a Hamiltonian of N spinless fermions on $L - \alpha(N-1)$ sites. Thus, for $h_i = 0$ the constrained model (4.2), which is a non-Gaussian fermionic model can be mapped to a non-interacting system.

What happens when disorder is introduced to the system? The model (4.2) becomes interacting *due to* the presence of on-site disorder term $\sum_i h_i n_i$. To see this, consider again the mapping between constrained and unconstrained model, as shown in the bottom panel of Fig. 4.2 d). For the constrained model, a particle at site i experiences the potential h_i. After the mapping, the particle at site i of the unconstrained model feels the potential $h_{i+\alpha N_i}$ (where $N_i \equiv \sum_{j=1}^{i-1} n_i$). The disorder becomes a source of interactions in the constrained model (4.2) since the potential felt by a particle on site i depends on the total number of particles to its right. Rewriting $\sum_{i=1}^{L} h_{i+\alpha N_i} n_i = \sum_i h_i n_i D_i^0 + \sum_i h_{i+\alpha} n_i D_i^1 + \ldots$, where $D_i^0 = \prod_{j<i}(1-n_j)$ $[D_i^1 = \sum_k n_k \prod_{j<i, j\neq k}(1-n_j)]$ is non-zero if there is exactly 0 [1] particles on sites $1 \leq j < i$ and further terms contain analogous terms that are non-zero if there are $1 < n < N$ particles on sites $1 \leq j < i$. Hence, the on-site disorder term introduces random interactions of infinite range to the model the constrained model is mapped to. Moreover, the strength of interactions is increasing with disorder strength W. Those two factors are at the root of the numerically observed delocalization of constrained models. Importantly, while our mapping between constrained and unconstrained models does not directly apply to disordered PXP models (since the varying number of spins up translates into varying length of the unconstrained chain), the mechanism in which disorder in presence of constraints provides interactions in the system is at play also in those models.

Our argument works also in the context of gauge theories as long as there is no direct Coulomb force. Hence, models such as 1D U(1) quantum links are captured by our reasoning (equivalent, for some parameter regimes, to the PXP model [116]), while models such as U(1) Wilson theories [143, 144] and 2D quantum link models [119, 120] are not.

4.4 Conclusions

Studying the crossover between ergodic and MBL regimes in locally constrained quantum spin chains, we observe that the whole crossover shifts linearly to larger disorder strength W with increasing system size. This trend, thanks to the availability of larger system sizes in the constrained Hilbert space geometry, is well documented and occurs both in the disordered PXP models as well as in models with $U(1)$ symmetry.

We argue that the observed delocalization can be traced back to fundamentally different roles played by the on-site disorder in conventional and constrained models. A sufficiently strong disorder leads to MBL in the former models as was exemplified for the disordered transverse field Ising model [145,146]. In contrast, for the constrained models studied here, the disorder can be seen as giving rise not only to one-body terms that tend to localize the fundamental excitations of the clean system but necessarily also to interactions that become stronger when disorder strength is increased. Depending on the details of the model, these interactions can be sufficiently strong to ultimately lead to delocalization. The family of disordered, constrained quantum spin chains considered in this work can be investigated experimentally in Rydberg atom setups. From the theoretical perspective, it emphasizes the richness and potential generality of dynamics arising out of the competition between interactions, disorder, and constraints.

Part II

Strongly Correlated Systems a Path Integral Monte Carlo study

Chapter 5

Finite-temperature critical behavior of long-range quantum Ising models

5.1 Introduction

Systems featuring long-range interactions are central in condensed matter and statistical physics, due to both their widespread presence in nature and the wide range of characteristic physical phenomena they display. However, their statistical and dynamical properties are much less understood than those of short-range systems [147, 148]. Classical long-range interacting systems are present in many fields of physics, ranging from, e.g., the dynamics of galaxies [149], plasma [150] to ionic crystals [151]. A statistical mechanics approach highlights distinguished properties in these systems, such as nonadditivity of energy, inequivalence of statistical ensembles, slow relaxation, and ergodicity breaking (for a review see, e.g., [152]).

Within the last decade, interest in quantum long-range interacting models has further surged due to the progress in manipulating and controlling these systems at an unprecedented level in cold atoms platforms [11–14, 153].

These experimental platforms naturally realize quantum Ising or Heisenberg models, with the possibility to engineer many-body interaction potentials decaying proportionally to $r^{-\alpha}$ as a function of distance r, ranging from van-der-Waals-like ($\alpha = 6$) and dipolar interactions ($\alpha = 3$) in the context of Rydberg atoms [11, 12], to Coulomb ($\alpha = 1$) and infinite-range ($\alpha = 0$) potentials for trapped ions [13, 14].

In particular the latter platform is of remarkable interest for the study of extremely long-range interactions, due to the small values of α that can be achievable. The spin system is modeled by a crystal of electromagnetically trapped atomic ions, with two electronic energy levels within each ion behaving as an effective spin-1/2 particle. These system achieve a great number of interacting spins and high fidelity of quantum state initialization and measurement. The ultracold ions arrange themselves in an equilibrium configuration from the balance between the attraction towards the trap centers and the inter-ion Coulomb repulsion resulting in a crystal structure along the weak confinement axes. The latter can be highly tuned and allows to study interacting spin systems in one dimension. Effective magnetic fields and spin-spin interactions can be realized by applying external microwave or optical fields to the ions. Pair interactions between the spins of the form $J_{ij}\sigma_i^z\sigma_j^z$ can be obtained, here, the experimental Ising couplings J_{ij} describe a correlated hyperfine transition of the i-th and the j-th ion mediated by the exchange of a virtual phonon. The

form of the coupling is well approximated by a typical long-range coupling:

$$J_{ij} = \frac{J_0}{|i-j|^\alpha}. \tag{5.1}$$

The exponent α can be set in the range $0 < \alpha < 3$ by adjusting the lasers frequencies. Note that energy scales are α-dependent, so, depending on experimental details, some regimes could be more accessible than others.

Recent experiments in such long-range interacting models have mostly centered on the investigation of inherent dynamical phenomena, such as Kibble-Zurek mechanism [106, 154], or dynamical quantum phase transitions [155, 156], discrete time crystals [157, 158], prethermalization [159] and many-body localization [5]. Despite of recent progress [160,161] in the understanding of thermalization in these long-range systems one key question has, however, remained open: especially in the limit of small interaction exponents, it is not known whether these long-range systems follow the fundamental principle of thermalization as expected for generic short-range models. In the first place, this obviously requires a thorough understanding of the thermal properties of the system of interest, which have only been partially explored even in paradigmatic Hamiltonians such as the one-dimensional long-range quantum Ising model.

One-dimensional long-range quantum Ising model. A quantum long-range model that can be directly realized in cold atoms experiments, is the long-range quantum Ising model with algebraically decaying interactions,

$$H = -\sum_{i\neq j}^{N} \frac{V}{|i-j|^\alpha} \hat{\sigma}_i{}^z \hat{\sigma}_j^z - h \sum_i^N \hat{\sigma}_i^x, \tag{5.2}$$

where $\hat{\sigma}_i^z$ ($\hat{\sigma}_i^x$) is the z (x) Pauli matrix and N is the number of sites.

The critical behaviour of this model has been object of intense theoretical study in the classical ($h \to 0$) limit. It was proven by Dyson [162] the existence of a phase transition for $1 < \alpha < 2$ between an ordered phase (ferromagnetic) and a disordered phase (paramagnetic). Renormalization Group (RG) studies [163, 164] predict that in any dimension d, two values of $\alpha = \alpha^{\pm}(d)$ exist such that for $\alpha < \alpha^-(d)$ the critical behaviour of the model is described by the mean-field theory, while for $\alpha > \alpha^+$ the system recovers the short-range counterpart model behaviour.

In particular, for $d = 1$, RG methods point to the existence of three different regimes as a function of the parameter α: (i) for $1 < \alpha \leq 3/2$ the mean field approximation is valid even at the critical point, (ii) for α greater than some α_* the model has the same critical exponents of the short-range model ($\alpha \to \infty$), and (iii) for $3/2 < \alpha \leq \alpha_*$ the critical exponents depend in a non trivial manner on the parameter α. The value $\alpha_* = 2$ was found in References[1] [162, 166, 167] and for $\alpha = 2$ a phase transition of the Berezinskii-Kosterlitz-Thouless universality class occurs [168–170].

In the $\alpha \leq 1$ regime the energy density of the model diverges; this effect can be avoided allowing to properly define the thermodynamic limit, by rescaling the interaction strength according to a procedure known as Kac's prescription.

Zero and finite temperature critical properties of the quantum model in Eq. 5.2 were studied in [171]. Using RG methods, Dutta and Bhattacharjee characterized the critical behaviour in the regime $\alpha > d$. In the case of the quantum phase transition it was found

[1] this boundary is still at the center of intense investigations, see e.g. [165] and references therein.

that the lower critical dimension for a fixed α follows the form $d_l = (\alpha - 1)/2$ and the upper critical dimension depends also on α like $d_u = 3(\alpha - 1)/2$. The one dimensional case was studied in detail. Importantly, due to the dependence of d_l with α, a zero temperature transition for all values of α is present. Here, was found three different regimes that characterize the critical behaviour as a function of α: (i) for $1 < \alpha \leq 5/3$ criticality is described by mean field theory, (ii) for $\alpha \geq 3$ the model has the same critical exponents of the well known short-range limit , and (iii) for $5/3 < \alpha < 3$ the critical exponents depend in a non trivial manner on the parameter α.

Oppositely with respect to the zero-temperature case, the finite-temperature critical behaviour of the one dimensional LR quantum Ising model is still poorly understood. Indeed, the latter has been predicted by general theoretical arguments [172] to belong to the universality class of the corresponding classical long-range Ising model, with quantum effects not changing this description at the qualitative level. While this picture has been essentially confirmed for the case $\alpha = 2$ by SSE studies [173], the latter demonstrated, in the proximity of the ground-state critical point, the presence of considerable finite-size effects induced by strong quantum fluctuations, which all but prevent observation of the expected classical regime even at very large system sizes.

In light of the experimental realizations of these models discussed above, investigating the thermal critical behavior of these Hamiltonians remains therefore of great importance, in order to determine the role and strength of the quantum effects in perturbing the predicted classical picture. Furthermore, (numerically) exact analysis of the finite-temperature regime is essential to determine non-universal details such as, e.g., the position of thermal critical points, which are influenced in a key way by quantum effects, and whose knowledge is crucial for laboratory realizations. Such a study is of especially great interest in the extremely long-ranged regime $0 < \alpha < 1$, which, to our knowledge, has not been the object of this kind of investigation, and (as mentioned above) is directly realizable in trapped-ions setups.

5.2 Methods

In this section, we describe the path integral mapping procedure, specifically for the quantum Ising chain in a transverse field case. Our goal is to formulate the problem in such a way that it becomes amenable to quantum Monte Carlo simulations. The latter method together with its particularities for the study of long-range interacting systems is also explained.

5.2.1 Path integral mapping

In the case of a system in thermal equilibrium described by a quantum Hamiltonian $\hat{H}$, the thermal expectation value of an observable $\hat{A}$ at inverse temperature $\beta = 1/T$ is defined as

$$\langle A \rangle = \frac{1}{Z} \operatorname{Tr} \left\{ \hat{A} e^{-\beta \hat{H}} \right\}, \tag{5.3}$$

where $Z = \operatorname{Tr}\{e^{-\beta \hat{H}}\}$ is the partition function.

Since in general the eigenvalues and eigenvectors of H are not known the estimation of such a quantity is extremely difficult for large systems. In this context, an effective strategy is provided by the *Path Integral* mapping: in this approach, one maps the quantum many body Hamiltonian to an equivalent classical system, where thermal averages can be computed employing standard techniques.

Following this prescription, the partition function is rewritten as

$$Z = \operatorname{Tr} \left\{ e^{-\beta \hat{H}} \right\} = \operatorname{Tr} \left\{ \prod_{j=1}^{P} e^{-\tau \hat{H}} \right\} = \sum_{\{|\alpha_0\rangle\}} \langle \alpha_0 | \prod_{j=1}^{P} e^{-\tau \hat{H}} | \alpha_0 \rangle, \tag{5.4}$$

where $\tau = \beta/P$ and $\{|\alpha_0\rangle\}$ is a complete basis of the system Hilbert space. Inserting identity operators $\sum_{\{|\alpha\rangle\}} |\alpha\rangle \langle\alpha|$ between the exponentials results in

$$Z = \sum_{\{|\alpha_i\rangle\}} \langle \alpha_0 | e^{-\tau \hat{H}} | \alpha_{P-1} \rangle \langle \alpha_{P-1} | \cdots | e^{-\tau \hat{H}} | \alpha_1 \rangle \langle \alpha_1 | e^{-\tau \hat{H}} | \alpha_0 \rangle \tag{5.5}$$

The Hamiltonian is then decomposed in two non-commuting terms $\hat{H} = \hat{H}_0 + \hat{H}_1$, where e.g., $\hat{H}_0$ is diagonal on the chosen basis set $\{|\alpha\rangle\}$. Then, the exponentials can be approximated as

$$e^{\tau(\hat{H}_0 + \hat{H}_1)} = e^{\tau \hat{H}_0} e^{\tau \hat{H} 1} + \mathcal{O}(\tau^2). \tag{5.6}$$

According to the Baker–Campbell–Hausdorff formula the partition function becomes

$$Z = \sum_{\{|\alpha_i\rangle\}} \langle \alpha_0 | \, e^{-\tau \hat{H}_0} e^{-\tau \hat{H}_1} \, | \alpha_1 \rangle \, \langle \alpha_1 | \, e^{-\tau \hat{H}_0} e^{-\tau \hat{H}_1} \, | \alpha_2 \rangle \cdots \langle \alpha_{p-1} | \, e^{-\tau \hat{H}_0} e^{-\tau \hat{H}_1} \, | \alpha_0 \rangle + \mathcal{O}(\tau) \tag{5.7}$$

$$= \sum_{\{|\alpha_i\rangle\}} e^{-\tau E_0} \, \langle \alpha_0 | \, e^{-\tau \hat{H}_1} \, | \alpha_1 \rangle \, e^{-\tau E_1} \, \langle \alpha_1 | \cdots e^{-\tau E_{p-1}} \, \langle \alpha_{p-1} | \, e^{-\tau \hat{H}_1} \, | \alpha_0 \rangle + \mathcal{O}(\tau), \tag{5.8}$$

where $E_i \equiv \langle \alpha_i | \, H_0 \, | \alpha_i \rangle$.

The approximation error due to the procedure above (known as *Suzuki-Trotter breakup*) vanishes for $P \to \infty$, making the mapping asymptotically exact.

The quantum Ising chain in a transverse field case. To clarify the procedure, the mapping is applied to a spin system. Specifically to a generalization of the Hamiltonian in Eq. 5.2. The generalized Hamiltonian is

$$\hat{H} = \underbrace{\sum_{i<j} J_{ij}\hat{\sigma}_i^z\hat{\sigma}_j^z}_{\hat{H}_0} + \underbrace{\sum_i h_i\hat{\sigma}_i^x}_{\hat{H}_1}. \tag{5.9}$$

Following the recipe explained in this section, a partition function of an equivalent classical model will be obtained. In this case, the complete basis of the Hilbert space is formed by the tensor product of single site $\hat{\sigma}_i^z$ eigenvectors with $\hat{\sigma}_i^z|\sigma_i\rangle = \sigma_i|\sigma_i\rangle$ and $\sigma_i = \pm 1$, the elements of the basis are referred as $|\boldsymbol{\sigma}\rangle$. Each term in Eq. 5.7 takes the form

$$\langle\boldsymbol{\sigma}_k|\, e^{-\tau\hat{H}_0}e^{-\tau\hat{H}_1}\,|\boldsymbol{\sigma}_{k+1}\rangle = e^{\tau\sum_{ij}J_{ij}\sigma_{ki}\sigma_{kj}}\,\langle\boldsymbol{\sigma}_k|\, e^{-\tau\hat{H}_1}\,|\boldsymbol{\sigma}_{k+1}\rangle \tag{5.10}$$

The remaining operator can be rewritten by expanding the exponential in Taylor series: noting that $(\sigma_i^x)^2 = 1$, even terms carry no operators, while the odd terms are left with only $\hat{\sigma}_x$. Regrouping the terms, one finds

$$e^{-\tau\hat{H}_1} = \prod_i(\cosh(\tau h_i) + \hat{\sigma}_i^x\sinh(\tau h_i)). \tag{5.11}$$

In order to rewrite the global partition function as a classical partition function, one needs to write the new matrix element as exponentials. For each spin term the desired form is (keeping into account the presence of a fictitious inverse temperature $\beta_{cl} = 1$)

$$\langle\sigma_{ki}|\, e^{\tau h_i\hat{\sigma}_i^x}\,|\sigma_{(k+1)i}\rangle \equiv \Gamma_i e^{\gamma_i\sigma_{ki}\sigma_{(k+1)i}}, \tag{5.12}$$

where the indexes k and i label the imaginary time slice and spin position respectively. Using Eq. (5.11) for the cases of parallel and antiparallel spins expectation values, one obtains

$$\langle(\uparrow,\downarrow)_i|\, e^{\tau h_i\hat{\sigma}_x}\,|(\uparrow,\downarrow)_i\rangle = \cosh(\tau h_i) \equiv \Gamma_i e^{+\gamma_i} \tag{5.13}$$

$$\langle(\uparrow,\downarrow)_i|\, e^{\tau h_i\hat{\sigma}_x}\,|(\downarrow,\uparrow)_i\rangle = \sinh(\tau h_i) \equiv \Gamma_i e^{-\gamma_i}. \tag{5.14}$$

Using the previous equations one can calculate the values of Γ_i and γ_i as

$$\gamma_i = -\frac{1}{2}\ln(\tanh(\tau h_i)) \tag{5.15}$$

$$\Gamma_i = \sqrt{\frac{1}{2}\sinh(2\tau h_i)}. \tag{5.16}$$

Each matrix element brings a $\prod_i\Gamma_i$ multiplication factor, where i runs over the sites. Therefore, the overall partition function can be written as

$$Z = \left(\prod_{i=1}^{L}\Gamma_i\right)^P \sum_{\{\sigma_{ki}\}}\exp\left[-\beta_{cl}\left(-\sum_{k=1}^{P}\sum_{i,j=1}^{L}\frac{\tau J_{ij}}{\beta_{cl}}\sigma_{ki}\sigma_{kj} - \sum_{i=1}^{L}\frac{\gamma_i}{\beta_{cl}}\sum_{k=1}^{P}\sigma_{ki}\sigma_{(k+1)i}\right)\right]. \tag{5.17}$$

The product of exponentials becomes the exponential of the sum of terms. This is the partition function of a classical, anisotropic, two-dimensional Ising mode, with system sizes P and L along the two directions. The spins here are classical variables. This formulation of the problem, unlike its quantum counterpart [Eq. (5.4)], is amenable to direct analysis via the powerful framework of Monte Carlo (MC) techniques, which are presented in the following sections.

5.2.2 Monte Carlo algorithms

The ensemble average of a quantity A for a classical system is given by

$$\langle A\rangle = \frac{\sum_i A(C_i)e^{-\beta E(C_i)}}{\sum_i e^{-\beta E(C_i)}} = \sum_i A(C_i)\left(\frac{e^{-\beta E(C_i)}}{Z}\right) = \sum_i A(C_i)W(C_i), \tag{5.18}$$

where the sum runs over all the configurations C_i of the system, $A(C_i)$, $E(C_i)$ are the value of the observable on the configuration C_i and the energy of the latter respectively, Z is the partition function and $W(C_i) = e^{-\beta E(C_i)}/Z$ will be referred as *configuration weight*.

The number of configurations in a many-body system usually scales exponentially with the system size (e.g., 2^N configurations for a system of N spin-1/2), making the exact calculation of sums such as that in Eq. (5.18) is usually impossible for medium to large system sizes. One of the most successful approach for the calculation of such quantities is known as *Monte Carlo Sampling*. This is an stochastic approach where the key idea is to approximate the complete sum in Eq. (5.18) with that of a number M of calculated terms in random configurations $\{C'\}$ of the system. Such an estimate asymptotically converge to the exact result as M is increased(as long as the configurations are uncorrelated). The statistical uncertainty of the calculated value scales asymptotically as $1/\sqrt{M}$ and is independent of the system size (which may however influence the time required to reach the asymptotic regime).

A practically feasible sampling of uniformly-distributed configurations will result in large statistical fluctuations on the calculated estimated values. This is because most of the sampled configurations will give a small weight if $W(C_i)$ is sharply peaked. A more efficient way of selecting configurations is *importance sampling*, where the generated configurations are statistically distributed following the weight function $W(C_i)$. Naturally, the latter procedure results in calculating sum terms with larger weight. With the weighting taken into account already in the selection of configurations, the estimate of the expectation value (A) is simply given by the arithmetic average of the function $A(C_i)$ over the generated subset C_i':

$$\langle A\rangle \cong \frac{1}{M}\sum_{i=1}^{M} A(C_i'). \tag{5.19}$$

Most importance sampling schemes involve creating a Markov chain of configurations (i.e., a sequence of configurations in which the probability that each of the elements is reached only depends on the preceding one) via applying random changes called *updates*.

In order to faithfully sample configurations according to the weight function, the update procedures are required to respect a few conditions.

(i) *Detailed balance* :

$$\frac{P(C_i' \to C_j')}{P(C_j' \to C_i')} = \frac{W(C_j')}{W(C_i')}, \tag{5.20}$$

where $P(C_i' \to C_j')$ is the transition probability from a configuration C_i' to a configuration C_j'. One possible choice for $P(C_i' \to C_j')$ which respect the detailed balance condition is the *Metropolis-Hastings (MH) sampling* [174] scheme,

$$P(C_i' \to C_j') = min\left(1, \frac{A_{ji}W(C_j')}{A_{ij}W(C_i')}\right), \tag{5.21}$$

where $A_{ij}(A_{ji})$ is the *proposition probability* for the $C_i' \to C_j'$ ($C_j' \to C_i'$) updates, i.e., probability of selecting the particular update that will lead from C_i' to C_j'.

The update can be accepted or rejected with probability 5.21, in this way satisfying the detailed balance condition. The ratio of configuration weights in this expression eliminates the need to compute Z, simplifying the sampling procedure.

(ii) *Ergodicity*: any configuration must be reachable from any other in a finite number of updates. If an update scheme is not ergodic, sectors of the configuration space may not be sampled, yielding incorrect results

The chosen updates have to obey these general rules, but the choice depends on the particular system and phenomena you are studying. The difference between all the possible choices boils down to their efficiency in exploring the configuration space.

As an example one of the most important considerations to make when choosing an update scheme is to minimize the amount of correlations between the sampled configurations. Indeed, in the Markov Chain MC sampling procedures, consecutive configurations are typically not statistically independent. Such condition is verified only between distant enough steps in the Markov Chain. The 'timescales' (in terms of MC steps) required to achieve statistical independence between two configurations is known as *autocorrelation time*, and its value strongly depends on both the physical behaviour of the system and the choice of MC updates. A higher auto correlation time leads to larger statistical uncertainties on MC estimates for observables [175]: the consequence of this effect may vary from simple requiring longer and more expensive simulations to making meaningful study of certain physical problems impossible in practice. A wise choice of updates (if available) is therefore paramount for numerically challenging problems.

In the next section, we will discuss several possible update choices for classical spin-(1/2) systems, which (through the Path Integral mapping discussed above) will be the focus of our numerical investigations.

5.2.3 MC updates for spin-1/2 systems.

We will consider systems of spin-1/2 degrees of freedom described by the Hamiltonian

$$H = -\sum_{ij} J_{ij}\sigma_i\sigma_j \qquad J_{ij} \geq 0. \tag{5.22}$$

In the following, we will introduce several choices of MC updates which can be employed to sample the configuration space of such spin systems, proceeding gradually towards more complex (and efficient) update procedures.

Single spin-flip. This basic local update is performed as follows:

1. A spin i is selected at random.
2. The change in energy δE_i between the present configuration and the one where the spin i is flipped is computed.
3. The spin i is flipped with probability $P_i = e^{-\beta\delta E_i}$.

This update is ergodic and the choice of P_i respects the detailed balance, implying that the single spin-flip is a fully valid choice for MC sampling of the configuration space.

However, updates such as this one may suffer from problems specifically caused by their local nature. As an example, it is well known that, close to a second-order critical point, the correlation length of the system diverges causing the effective dynamics of the system to be described by large clusters of spins rather than single-spin dynamics.

From the point of view of MC simulations, this leads a sharp increase in auto correlation times when approaching the critical point, a phenomenon known in this context as *critical slowing down*. In particular the auto correlation time τ_{AC} will depend on the system size L through the *dynamical critical exponent* z as

$$\tau_{AC} \propto L^z. \tag{5.23}$$

Due to the local nature of the single spin-flip updates, the sampling of the statistically relevant configurations, which are separated by changes at the typical scale of the cluster size, becomes extremely challenging. This leads to a relative hight value of $z \cong 2$ which renders simulations in the critical region very hard to perform.

Wolff or Single-Cluster algorithm Wolff [176] introduced a so-called single-cluster update, which is a variant of Swendsen–Wang [177] cluster update. In the Wolff's implementation a single cluster of parallel spins is formed and flipped. The fact that is exceedingly simple to implement has certainly contributed to the popularity of the Wolff algorithm. The prescription for implementing this update is as follows:

1. A spin i is selected at random.
2. All nearest neighbours j of i are added to the cluster with probability $p_{ij} = 1-e^{-2\beta J_{ij}}$, provided spins i and j are parallel and the bond between i and j has not been consider before.
3. Each spin j that indeed have been added to the cluster is also placed on the stack. Once all neighbours of i have been consider for inclusion on the cluster, a spin is retrieved from the stack and all its neighbours are considered in turn for inclusion in the cluster as well, following the prescription on step (2).
4. Steps (2) and (3) are repeated iteratively until the stack is empty.
5. The cluster is complete and all its spins are flipped.

Remarkably, this algorithms is rejection free. Indeed,the assignment of bonds involves specific probabilities, but once the cluster(s) have been formed can be flipped independently without imposing an acceptance criterion that involves the energy change induced by such a collective spin-reversal operation. The cluster created have a structure that is very efficient at destroying non local correlations in the MC sampling procedure. As a result, the dynamical critical exponent z is lowered to a much smaller value [178] and independent configurations can be generated at much faster rate that with a single-spin flip algorithm. This advantage only holds in the vicinity of the critical point.

Long-range cluster update. The study of systems with long-range interactions is notoriously difficult, due to the large number of iterations that has to be taken into account. Luijten and Blöte [179] developed an algorithm based on the Wolff cluster method. In this algorithm, the time per spin visit in the process of forming the cluster is independent of system size. This fact together with the reduction of critical slowing down by the use of cluster methods makes this algorithm very suitable for the study of critical phenomena and long-range interactions.

Following the single cluster prescription(for simplicity we consider a one dimensional model), one starts with a randomly chosen spin and activate bonds with all others parallel spins in the system with probability

$$p_{ij} = p_m \equiv 1 - e^{-2\beta J_{ij}}, \tag{5.24}$$

where p_m denotes the probability of activating a bond between two spins at distance $m = |j - i|$ (in lattice spacing units). As explained, when the bond is activated the corresponding spin is added to the cluster and the stack. When all neighbours of the first spin have been considered, a new spin is taken from the stack and the process is repeated until the stack is empty.

Importantly, to avoid considering each single bond, the concept of *cumulative bond probability* is introduced. This quantity allows to obtain the distance from the current analyzed spin to the first spin to be considered to be added to the cluster(the spin is added if both spins are aligned). The probability that the first bond is activated at a distance j from the current spin is given by

$$P(j) = (1 - p_1)(1 - p_2) \cdots (1 - P_{j-1})(p_j). \tag{5.25}$$

And one can define the cumulative bond probability as

$$C(j) \equiv \sum_{n=1}^{j} P(n). \tag{5.26}$$

Then, if a random number between $C(j-1)$ and $C(j)$ is drawn, the bond has to be activated between the current spin and the spin at distance j, provided they are parallel. The next bond has to be activated between the current spin and a spin at distance $k > j$, we have to shift P as

$$P_j(k) = (1 - p_{j+1})(1 - p_{j+2}) \cdots (1 - p_{k-1})p_k. \tag{5.27}$$

One can generalize Eq. (5.26) as

$$C_j(k) = \sum_{n=j+1}^{k} P_j(n), \tag{5.28}$$

and substituting p_m from Eq. (5.24), one finds:

$$C_j(k) = 1 - \exp\left(- \sum_{n=j+1}^{k} -2\beta J_n \right), \tag{5.29}$$

where J_n is the coupling between spins at distance n. The $C_j(k)$ values can be calculated in advance and saved in a lookup table. Then, the procedure of creating bonds with parallel spins from the current spin reduce to through random numbers ($\in [0, 1]$), and search in the lookup table the corresponding $C_j(k)$(note that the j value is always known). This will give us the distance k between the current spin and the spin to be added to the cluster. The value of j becomes equal to k and a new random number is trough and the procedure is repeated until $j > L$. After that, a spin is taken from the stack and the procedure of forming the cluster is repeated, and the general Single-Cluster recipe is followed.

5.3 Results

We study both the ground-state and finite-temperature phase diagram of the long-range ferromagnetic quantum Ising model in one spatial dimension, by means of numerically exact, large-scale Path Integral Monte Carlo simulations. We perform our calculations for two representative values of α: namely, we choose $\alpha = 0.05$ and $\alpha = 1.50$, within the extremely long-range region $\alpha < 1$ and intermediate region $1 < \alpha < 2$, respectively. We employ a wide variety of well-known finite-size scaling techniques to determine the position (i.e., the critical points) and critical exponents of both the ground-state and finite-temperature paramagnetic-ferromagnetic transitions displayed by the model, obtaining the phase diagram displayed in Fig. 5.1.

We determine the critical points and critical exponents for the ground-state ferromagnetic-paramagnetic transition. Our results for critical point positions and correlation length critical exponents are in agreement with existing predictions in the literature where the latter are available (i.e., $\alpha = 1.50$), while we encounter relatively small ($\sim 7\%$) deviations with respect to our estimate for the magnetization critical exponent. We then obtain accurate results for the position of the critical points in the finite-temperature regime for several values of the interaction strength. Concomitantly, our estimated correlation length critical exponents at $\alpha = 1.50$ essentially confirm the theoretical prediction of no qualitative deviations from the classical universality class due to quantum fluctuations, while discrepancies (up to 10% in the strongly interacting region) appear in the susceptibility critical exponent.

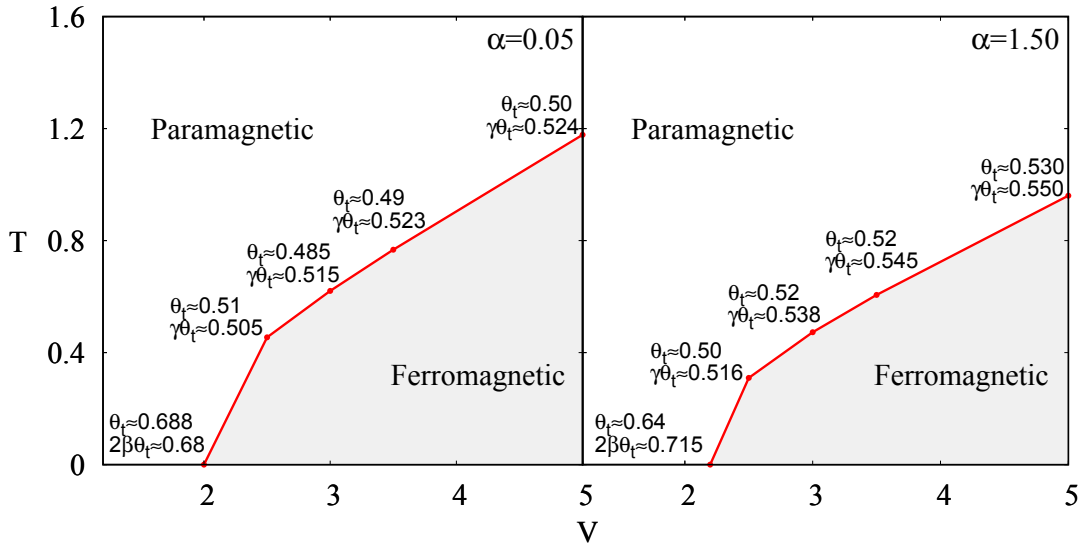

Figure 5.1: Calculated phase diagram of the long-range transverse-field Ising model in Eq. (5.30), displaying the ground-state and finite-temperature phase boundary and critical exponents obtained using finite-size scaling techniques. Panels (a) and (b) correspond to $\alpha = 0.05$ and $\alpha = 1.50$, respectively. Here, T is the system temperature in units of the Boltzmann constant, and V is the interaction strength in units of the transverse field (see below). The displayed results for the effective thermal exponent and its product with the magnetization and susceptibility critical exponent are those obtained via data collapse (see below).

The model is described by the Hamiltonian

$$H = -\frac{V}{K(L)} \sum_{i<j} \frac{\hat{S}_i^z \hat{S}_j^z}{r_{ij}^\alpha} - h \sum_i \hat{S}_i^x, \tag{5.30}$$

where $V > 0$ is the interaction strength, i, j run over the sites $1, \ldots, L$ of a one-dimensional lattice with periodic boundary conditions, r_{ij} is the distance between sites i and j, $\hat{S}_i^z$ ($\hat{S}_i^x$) is the component along z (x) of the spin-1/2 operator acting on site i, and $K(L) \equiv (L-1)^{-1} \sum_{i \neq j} r_{ij}^{-\alpha}$ is the Kać renormalization factor. The latter ensures the existence of a proper thermodynamic limit in the regime $\alpha \leq 1$, while for $\alpha > 1$ it amounts to a rescaling of the interaction strength, and does not change the universal features of the critical behavior of the model. We remark that the presence of this renormalization factor is directly related to how interactions with $\alpha < 3$ are engineered in trapped ions experiments. The latter exploit coupling between the ions and collective modes of the ion chain (phonons), mediated via a single laser shined over the full sample. Increasing the number of ions while keeping the lattice spacing constant naturally leads to a reduced coupling strength, that translates into the fact that the energy of the full system is still extensive - as reflected by Kać normalization. In the following, periodic boundary conditions are taken into account following the minimum-image convention, and $h = 1$ will be taken as unit of energy.

For very small interaction strength V, the ground state of the system in the thermodynamic limit is a paramagnet, characterized by a vanishing value of the magnetization along the z direction $|m_z| \equiv L^{-1} |\sum_i S_i^z|$. On the contrary, for $V \gg 1$ the system is in a ferromagnetic phase, displaying a finite $|m_z|$. The existence of a finite-V phase transition connecting these two states can be proven via analytical arguments (see, e.g., [180]); its UC depends strongly on the value of the decay parameter α. Indeed, the $\alpha = 0$ case, also referred to as *Lipkin-Meshkov-Glick model* [181], can be described in an exact fashion at the mean-field level [182], and the paramagnetic-ferromagnetic transition has been proven to be of the mean-field type in the $1 < \alpha < 5/3$ region. In contrast, in the regime $\alpha \geq 3$, the critical point belongs to the short-range UC (i.e., the one of the ferromagnetic-paramagnetic transition in the nearest-neighbor limit $\alpha \to \infty$).

In the finite-temperature regime, generic scaling arguments [172] predict that the model should display the same critical behavior as its classical (i.e., $h = 0$) counterpart, due to the finiteness of the system size in the imaginary time dimension (see below). The critical behavior of the classical model has been studied via both analytical (see, e.g., [183]), RG (see, e.g., [184]) and numerical techniques (see, e.g., [185]) in the $\alpha > 1$ regime. Here, the system displays a second-order ferromagnetic-paramagnetic thermal phase transition for $1 < \alpha < 2$, with the region $1 < \alpha < 3/2$ belonging to the mean-field regime, while in the point $\alpha = 2$ the model undergoes a finite-temperature transition of the BKT type, and the short-range regime is reached (i.e., no finite-temperature transition takes place) for $\alpha > 2$.

We perform our investigation of the Hamiltonian in Eq. (5.30) via Path Integral Monte Carlo (PIMC) [186], a numerically exact technique for the study of unfrustrated systems of bosons and quantum spins. In this approach, one maps the features of a quantum model of interest to those of an equivalent, higher-dimensional classical one, which is then studied via Metropolis Monte Carlo simulations. The quantum-to-classical mapping described above maps the partition function of the extended transverse-field Ising model in Eq. (5.30) into the one of an anisotropic extended Ising model on a rectangular lattice, via a procedure known as *Suzuki-Trotter breakup*. Here, in addition to the original spatial dimension, one also considers a discretized and periodic one, known as *imaginary time*, which extends in the interval $[0, \beta]$, where $\beta = 1/T$ is the inverse system temperature in units of the Boltzmann constant. The number of sites M along this direction (also known as *slices*) is

a free parameter which affects the accuracy of the mapping: indeed, the latter is exact up to $O(\beta/M)$ corrections, which vanish in the limit $M \to \infty$.

In the spatial direction, the extended Ising model resulting from the mapping displays the same ferromagnetic long-range interactions present in the spin-spin term of the model in Eq. (5.30), while spin-spin couplings are nearest-neighbor in the imaginary time direction. Our PIMC algorithm combines conventional Wolff cluster updates in imaginary time with efficient long-range cluster updates in the spatial direction. The latter combination -to our knowledge- has never been used before. The choice of these two state-of-the-art techniques allow to accurately analyze large system sizes (up to $L = 8192$ sites) at low enough temperatures (down to $\beta = 1024$) to reach the ground state regime. The Suzuki-Trotter corrections mentioned above are kept into account by performing simulations with increasing number of slices (up to $M = 65536$), until a value $M = M^*$ is found such that the corresponding values of the observables of interest were determined to be identical, within statistical error, to those obtained for $M = 2M^*$. The same protocol (with β in the place of M) is adopted to ensure the $T \to 0$ limit is reached in the investigation of the ground state regime.

The PIMC algorithm gives us direct access to observables commuting with the S_i^z operators, including the integer powers of $|m_z|$. This allows us to compute quantities such as the Binder cumulant

$$U = \frac{1}{2}\left[3 - \frac{\langle m_z^4 \rangle}{\langle m_z^2 \rangle^2}\right], \tag{5.31}$$

where $\langle \ldots \rangle$ stands for statistical averaging, which is expected to converge to 1 (0) in a ferromagnetic (paramagnetic) phase [175]. We also compute the "classical" susceptibility

$$\chi = \beta L \left(\langle m_z^2 \rangle - \langle |m_z| \rangle^2 \right), \tag{5.32}$$

which, in proximity of a finite-temperature critical point of a quantum model, approximates well the exact functional form of the magnetic susceptibility [173].

In order to extract reliable information on the critical behavior of the model in the thermodynamic limit, we exploit the well known finite-size scaling (FSS) theory [175]. In this framework, scaling relations of various quantities in terms of the correlation length ξ, which diverges when approaching a critical point, are exploited to obtain finite-size information by noting that in a finite system ξ will saturate to a value $O(L)$, where L is the system size. Features such as the position of the critical point or the critical exponents, on which the original scaling relations depended, can then be directly extracted via numerical fits as a function of L. In the following section, when discussing the fitting procedures to obtain such quantities, we will offer detailed formulae regarding FSS predictions for observables such as U and χ.

We investigate the critical properties of the model in Eq. (5.30) in the ground-state and finite-temperature regime for $\alpha = 0.05$ and $\alpha = 1.50$.

The first step in our analysis is the determination of the paramagnetic-ferromagnetic critical point V_c in the ground-state regime, which we accomplish by fitting to our numerical data for the Binder cumulant U its expected FSS behavior. The Binder cumulant curves $U(V)$ for system sizes L and, e.g., $2L$ are expected to cross at size-dependent points $V = V_U(L)$, which will follow (to the leading order) the FSS scaling [187, 188]

$$V_U(L) = V_c \left(1 + aL^{-\omega-\theta_t}\right), \tag{5.33}$$

where V_c is the critical point, and the *effective thermal exponent* θ_t is linked to the correlation length critical exponent ν.

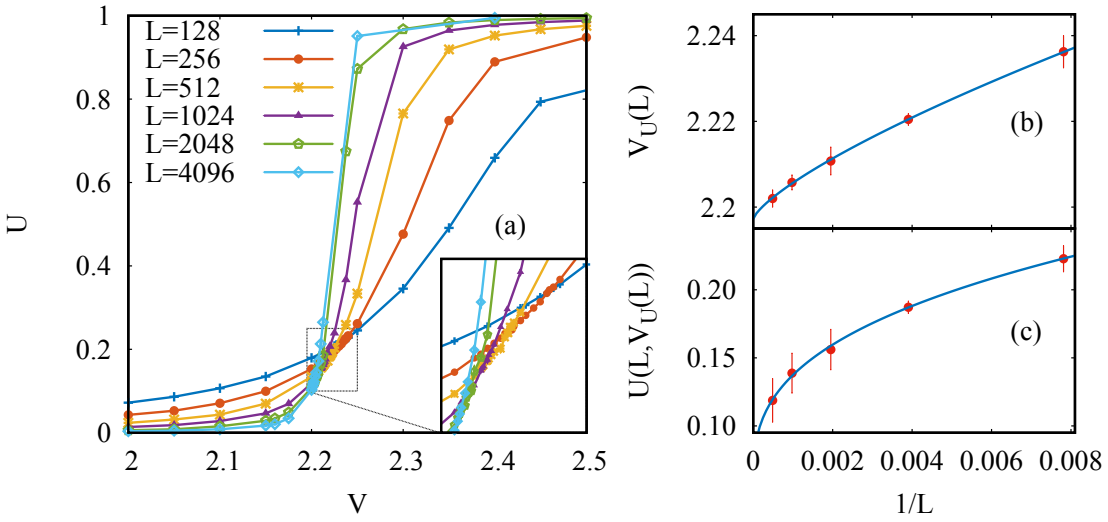

Figure 5.2: Binder cumulant scaling in the ground state regime (in all panels, $\alpha = 1.50$). Panel (a): Binder cumulant curves as a function of V for different system sizes. Solid lines are a guide to the eye. Inset: magnification of the curve crossing region. Panel (b): computed crossing positions $V_U(L)$ between the Binder cumulant curves at system sizes L and $2L$. The continuous line is a numerical fit to the expected FSS behavior in Eq. (5.33). Panel (c): computed values of the Binder cumulant at the crossing points $V_U(L)$ between system sizes L and $2L$. The continuous line is a numerical fit to the predicted FSS behavior in Eq. (5.34).

In the ground-state regime $\nu^{-1} = \theta_t$ outside of the mean-field region; conversely, when the latter is entered, corrections to the leading scaling behavior can be taken into account [188] via the generalized expression $\nu^{-1} = (d_{\rm uc}(\alpha)/d)\,\theta_t$, where d is the dimensionality and $d_{\rm uc}(\alpha) = 3(\alpha - 1)/2$ is the upper critical dimension for the value of α of interest.

Comparison of Eq. (5.33) with the predicted leading-order FSS behavior for the *value* of the Binder cumulant at the $V_U(L)$s,

$$U(L, V_U(L)) = b + cL^{-\omega}, \tag{5.34}$$

allows us to obtain estimates for V_c and θ_t, by fitting our computed results for the crossing features [see Fig. 5.2(a)] with the functional forms above.

Fig. 5.2(b-c) display examples of the FSS fitting procedures mentioned above; the obtained values of the critical point and of the effective thermal exponent θ_t are listed in Table 5.1.

α	V_c (BC)	V_c (DC)	θ_t (BC)	θ_t (DC)	$2\beta_m\theta_t$ (DC)
0.05	1.9997(4)	1.9999	0.50(7)	0.688	0.68
1.50	2.1972(7)	2.1981	0.39(6)	0.64	0.715

Table 5.1: Values of V_c, θ_t, and β_m (see text) associated to the ground state paramagnetic-ferromagnetic transition, computed via FSS analysis of the Binder cumulant crossings (BC) and via data collapse of the squared magnetization m_z^2 (DC).

In order to gain more insight into the ground-state critical behavior of the model, we perform a data collapse analysis by directly exploiting the FSS predictions for the behavior

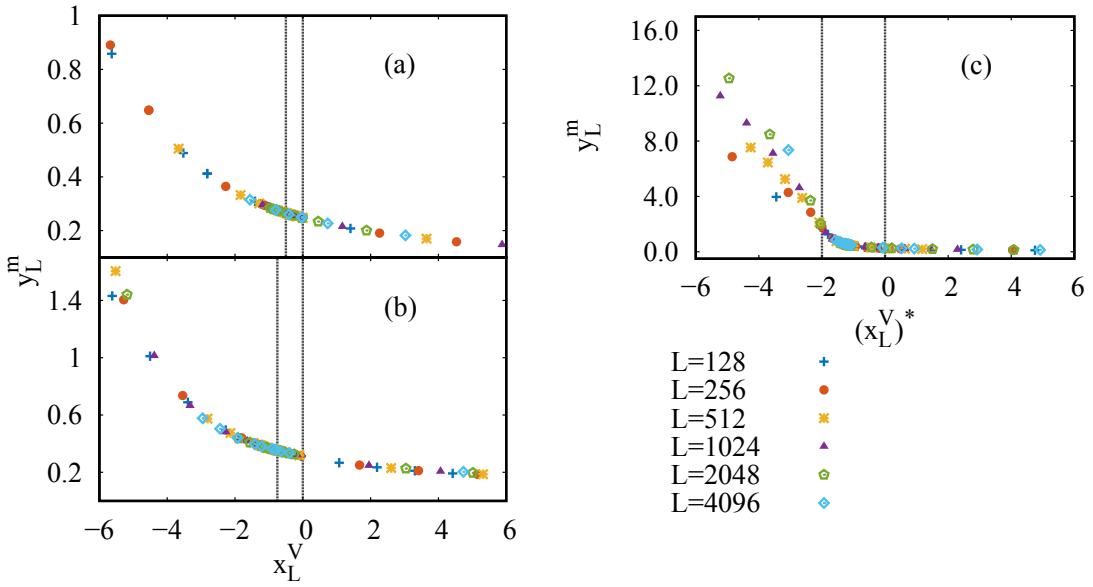

Figure 5.3: Panel (a): data collapse of the rescaled squared magnetization y_L^m as a function of the rescaled interaction strength x_L^V for $\alpha = 0.05$. Panel (b): same as panel (a) for $\alpha = 1.50$. Panel (c): same as panel (b), where the data collapse rescaling is performed on the Kać-factor-free rescaled interaction (see text). In all panels, the black dashed lines enclose the interval of the independent variable within which the data collapse scaling fit has been performed.

of the squared magnetization close to a critical point [175, 188],

$$m_z^2 \sim L^{-2\beta_m\theta_t} \cdot f\left[L^{+\theta_t}\left(V_c - V\right)\right] \qquad V \gtrsim V_c, \tag{5.35}$$

where β_m is the magnetization critical exponent, up to corrections of higher order in $1/L$. This scaling law implies that the rescaled magnetization curves $y_L^m \equiv m_z^2(L)L^{+2\beta_m\theta_t}$ for different system sizes should coincide if plotted as a function of $x_L^V \equiv (V_c - V)\, L^{\theta_t}$. We perform a high-order polynomial fit of y_L^m as a function of x_L^V in a window around the critical point $x_L^V = 0$ for a wide range of candidate values of V_c, θ_t and β_m, choosing as our final estimates for these quantities the values which resulted in the fit with the lowest chi-square value. While it is hard to assign a rigorous error bar to the results of a data collapse analysis, we estimate the order of magnitude of the error on our results by performing the same fits in a considerably larger (i.e, containing of the order of double the number of points) window around the critical point, and taking the difference between the optimal values of V_c, θ_t, and β_m for the two windows as the order of their numerical uncertainty.

Our collapsed data is displayed in Fig. 5.3(a-b); the obtained estimates for V_c, θ_t and β_m are listed in Table 5.1. We note that the data collapse behavior takes place over a fairly wide range of values of the rescaled order parameter x_L^V, despite relatively narrow fitting windows for the scaling behavior in Eq. (5.35) (the intervals between dashed lines in Fig. 5.3). This highlights the faithfulness of the data collapse scaling description of our numerical data, which translates to highly reliable estimates of the critical properties of the system.

Examination of our results points out i) the remarkable agreement of the critical point estimates obtained via the Binder cumulant FSS and the data collapse, and ii) conversely, the incompatibility between the two estimates for the effective thermal exponent θ_t. Due

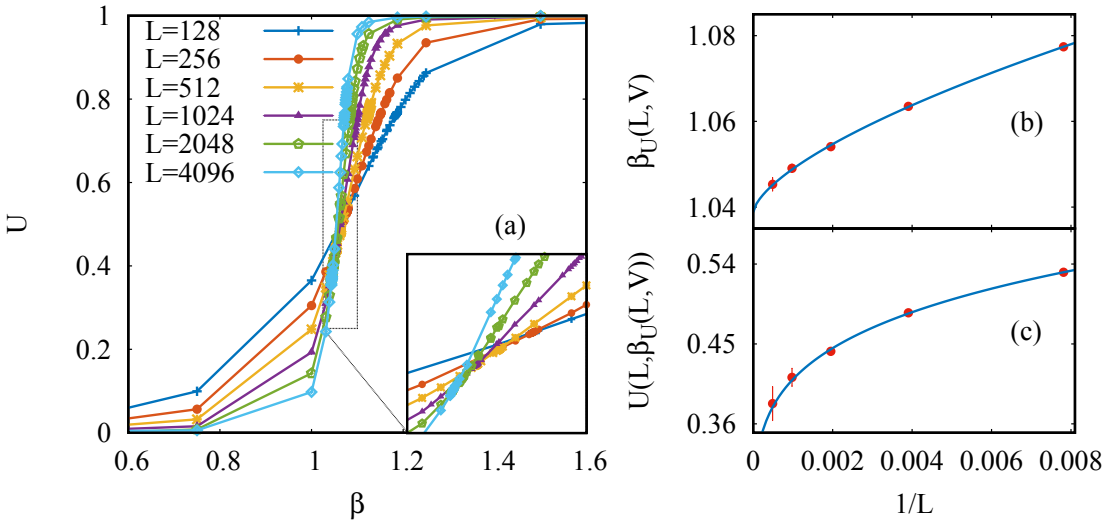

Figure 5.4: Binder cumulant scaling in the finite-temperature regime (in all panels, $\alpha = 1.50$ and $V = 5.0$). Panel (a): Binder cumulant curves as a function of β for different system sizes. Solid lines are a guide to the eye. Inset: magnification of the curve crossing region. Panel (b): computed crossing positions $\beta_U(L, V)$ between the Binder cumulant curves at system sizes L and $2L$. The continuous line is a numerical fit to the expected FSS behavior in Eq. (5.33). Panel (c): computed values of the Binder cumulant at the crossing points $\beta_U(L, V)$ between system sizes L and $2L$. The continuous line is a numerical fit to the predicted FSS behavior in Eq. (5.34).

to the arguments mentioned above, we believe the data collapse estimates for the critical features to be more reliable in this regard.

For $\alpha = 1.50$, we find agreement for θ_t and deviations of the order of 7% for $2\beta_m\theta_t$ from the independent SSE predictions in Ref. [188] which, in our notation, are $\theta_t \simeq 2\beta_m\theta_t \simeq 0.667$. We also find good agreement with the estimate $V_c \simeq 0.42$ (in our notation) given in [188] for the position of the ground-state critical point, by performing a data collapse where the rescaled interaction x_L^V is replaced by $\left(x_L^V\right)^* \equiv L^{+\theta_t}\left(V_c - V/K(L)\right)$ (the rescaling is required since the Kać correction factor is not employed in [188]). The resulting data collapse [see Fig. 5.3(c)] yields optimal values $\theta_t \simeq 0.64$, $2\beta_m\theta_t \simeq 0.76$, and $V_c \simeq 0.42$. For $\alpha = 0.05$, our estimates for θ_t and $2\beta_m\theta_t$ are compatible (up to deviations of the order of 3% in θ_t) with the ones corresponding to the $\alpha = 0$ mean-field critical behavior, i.e., $\theta_t = 2\beta_m\theta_t = 2/3$ [182].

Once the boundary of the ground-state ferromagnetic phase is determined, we investigate whether or not ferromagnetic order survives for $T > 0$, and more in general the details of the critical behavior of the model in this regime. To this end, we perform finite-temperature calculations for fixed values of V belonging to the ferromagnetic phase in the ground state regime. We apply the FSS framework to quantities such as the Binder cumulant and the susceptibility, computed as a function of T, to estimate features of the temperature-driven critical behavior.

Indeed, our results for the Binder cumulant as a function of β at fixed V and different system sizes immediately confirm the presence of a finite-temperature phase transition, as pointed out by the appearance of the crossing behavior discussed above [see Fig. 5.4(a)] at size-dependent points $\beta_U(L, V)$. We determine the V-dependent critical temperatures $\beta_c(V)$ and the associated $\theta_t(V)$ via fitting of the FSS relations in Eqs. (5.33)-(5.34) to

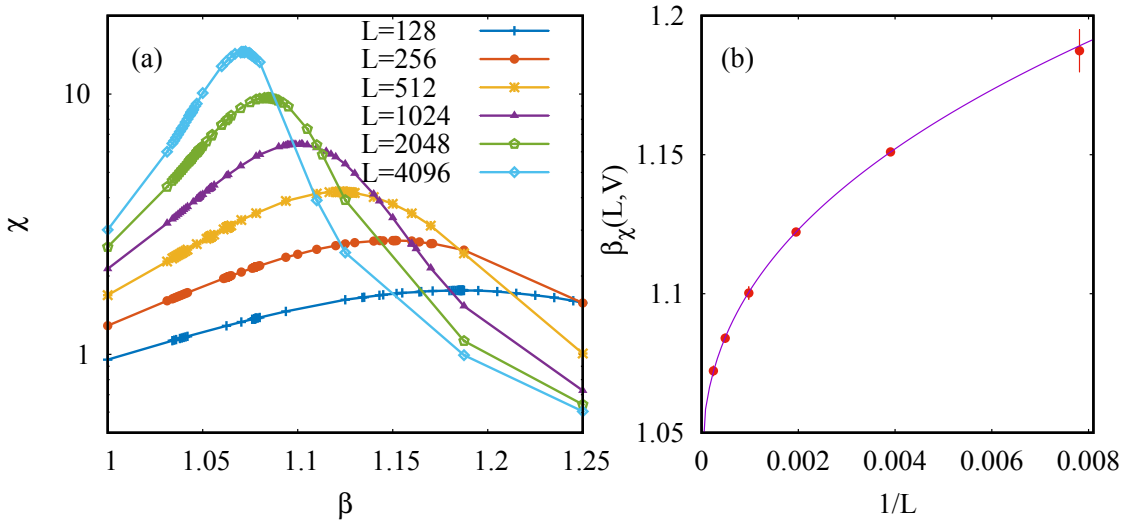

Figure 5.5: FSS analysis of the magnetic susceptibility in the finite-temperature regime (in all panels, $\alpha = 1.50$ and $V = 5.0$). Panel (a): susceptibility curves as a function of β for different system sizes. Solid lines are a guide to the eye. Panel (b): finite-size peak positions $\beta_\chi(L)$. The continuous line is a numerical fit to the expected FSS behavior in Eq. (5.36).

our computed crossing features, with the thermal critical points β_c and β taking the role of V_c and V, respectively. If the hypothesis of essentially classical critical behavior for the finite-temperature quantum model holds (as we argue below) one may link [189] θ_t to the correlation length critical exponent ν via the relation $\nu^{-1} = \left(d_{\rm uc}^{\rm class}(\alpha)/d\right)\theta_t$, where $d_{\rm uc}^{\rm class}(\alpha) = 2(\alpha - 1)$ is the classical upper critical dimension.

Examples of this analysis are displayed in Fig. 5.4(b-c): the obtained critical parameters are listed in Table 5.2. We remark here that our application of this approach encountered in some cases strong difficulties due to significant finite-size effects in proximity of the $\beta_c(V, L)$. In particular, the relatively large numerical uncertainties on the values of the Binder cumulant in this region led to the necessity to perform conservative estimates of the finite-size crossing points. In turn, this prevented us in some cases from obtaining meaningful (i.e., with small enough error bars) estimates for θ_t.

In order to obtain an independent estimation of our quantities of interest, we investigate the finite-temperature behavior of the magnetic susceptibility for the same values of V selected in our Binder cumulant analysis. At finite system size and fixed interaction strength, χ is expected to display peaks at size-dependent temperatures $\beta_\chi(L, V)$; the FSS framework predicts for the latter [175, 188] the leading scaling behavior

$$\beta_\chi(L, V) = \beta_c + fL^{-\theta_t} \tag{5.36}$$

as a function of the system size.

Our numerical data confirm the expected behavior of χ [see Fig. 5.5(a)]. Fitting the FSS functional form in Eq. (5.36) to the computed peak positions [see Fig. 5.5(b) for an example] allows us to directly estimate the critical temperatures and effective thermal exponents as a function of the interaction strength (see Table 5.2 for a list of results).

While also requiring conservative estimates (and therefore large error bars) for the peak positions, due to strong finite-size effects, we found the susceptibility-based approach to be much less sensitive to this issue than the Binder cumulant FSS discussed above. In

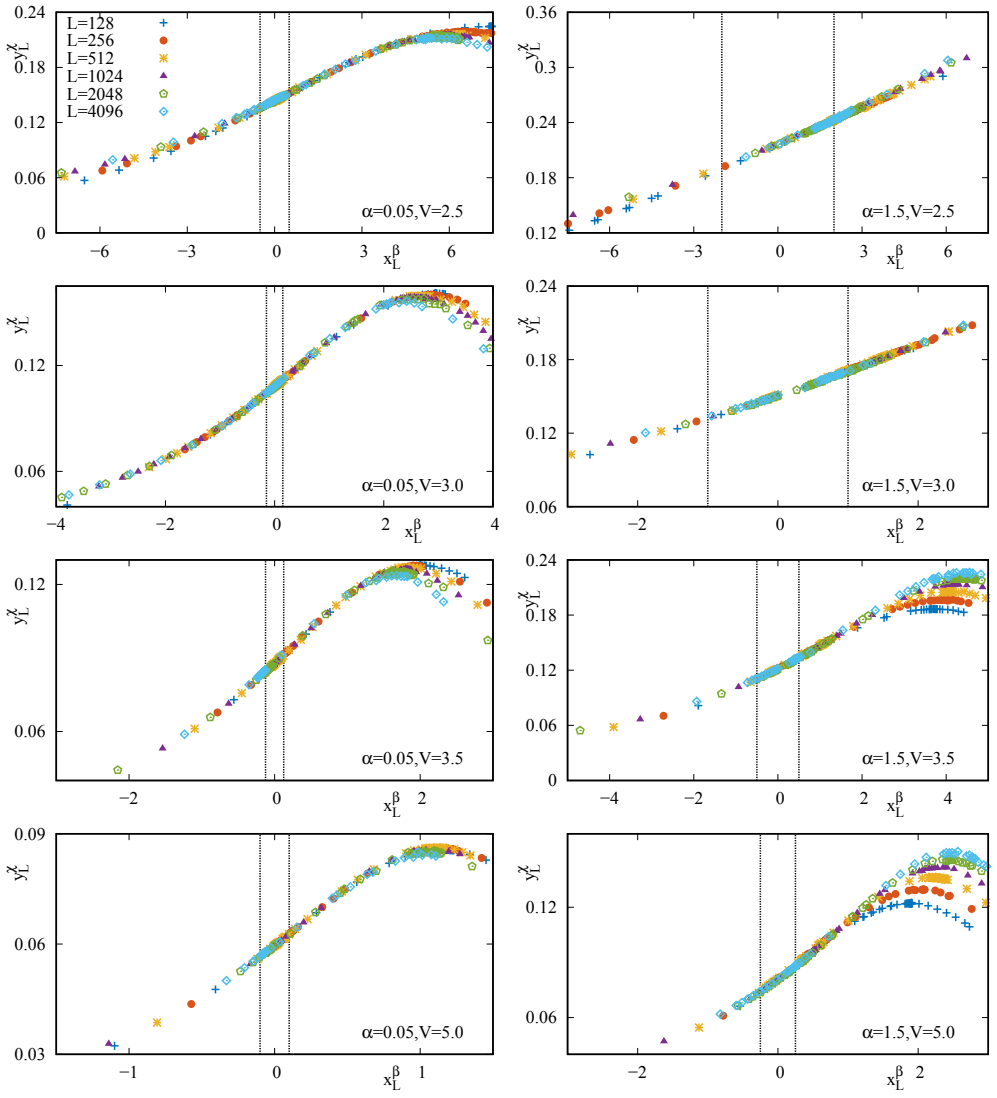

Figure 5.6: Data collapse of the rescaled magnetic susceptibility y_L^χ as a function of the rescaled order parameter x_L^β for the values of α and V studied in this work. The black dashed lines enclose the interval of x_L^β within which the data collapse scaling fit has been performed.

particular, we encountered problematic results only for $V = 2.5$, for both values of α considered in this work, where our estimates were strongly dependent on the set of system sizes considered in the fitting procedure (the reported results correspond to the fits with all sizes considered).

We finally analyze the critical properties of the model by performing a data collapse analysis for the behavior of the magnetic susceptibility close to the finite-temperature critical points [175, 185, 188],

$$\chi \sim L^{+\gamma\theta_t} \cdot f\left[L^{+\theta_t}\left(\beta_c - \beta\right)\right] \qquad \beta \sim \beta_c, \tag{5.37}$$

where γ is the susceptibility critical exponent, up to corrections of higher order in $1/L$. The analysis follows the same protocol outlined in our discussion of the ground-state regime, with the rescaled dependent and independent variables here being $y_L^\chi \equiv \chi(L)L^{-\gamma\theta_t}$ and

		β_c			θ_t			$\gamma\theta_t$
	V	U	χ	χ_{dc}	U	χ	χ_{dc}	χ_{dc}
$\alpha = 0.05$	$V = 2.5$	2.2007(4)	2.23(1)	2.20	/	0.72(4)*	0.51	0.505
	$V = 3.0$	1.6120(7)	1.61(1)	1.612	/	0.54(3)	0.485	0.515
	$V = 3.5$	1.299(1)	1.303(3)	1.303	/	0.54(2)	0.49	0.523
	$V = 5.0$	0.8474(2)*	0.844(2)	0.8491	0.5(1)	0.47(2)	0.50	0.524
$\alpha = 1.50$	$V = 2.5$	3.21(1)	3.351(9)	3.229	0.49(7)	0.75(1)*	0.50	0.516
	$V = 3.0$	2.109(1)*	2.12(1)	2.115	0.50(2)	0.48(3)	0.52	0.538
	$V = 3.5$	1.647(6)	1.646(5)	1.650	0.5(2)	0.46(2)	0.52	0.545
	$V = 5.0$	1.039(1)	1.035(1)	1.041	0.44(7)	0.41(1)	0.530	0.550

Table 5.2: Summary of the computed estimates for β_c, θ_t, and $\gamma\theta_t$ (see text) for the finite-temperature transitions at our investigated values of α and V. Our results are categorized according to the methodology employed to derive them: namely, FSS of the Binder cumulant crossings (U), FSS of the magnetic susceptibility peak position (χ), and data collapse of the susceptibility (χ_{dc}). Estimates marked with an asterisk ($*$) did not converge with respect to the choice of minimum size to be included in the fitting procedure.

$x_L^\beta \equiv (\beta_c - \beta)\, L^{\theta_t}$, respectively.

Fig. 5.6 displays our collapsed data for all the values of α and V investigated in this work; the corresponding optimal (in the sense discussed above) results for β_c, θ_t and γ are displayed in Table 5.2. As in the ground-state regime, we observe that the parameter range in which the data collapse scaling *ansatz* is respected noticeably exceeds our fitting window (and vastly so, in most cases), highlighting the accuracy of this approach in describing the critical behavior of the model. Furthermore, this protocol does not require the estimation of size-dependent features, such as the curve crossings for the Binder cumulant, or the peak position for the susceptibility, allowing us to obtain much more reliable and systematics-free results. We also note that high degree of accuracy with which the scaling law in Eq. (5.36) can be applied to describe the behavior of the "classical" susceptibility in Eq. 5.32 is a strong indication of the goodness of the latter as an approximation for the complete functional form of the magnetic susceptibility.

A direct analysis of the results for the critical exponents listed in Table 5.2 shows that our estimates obtained via FSS of the Binder cumulant crossings, where meaningful in the sense discussed above, are consistent within error bar with the ones obtained via susceptibility data collapse. Concomitantly, in some points we observe differences (which remain consistently small, except for the point $\alpha = 1.50, V = 5.00$) between the latter and the results of the susceptibility peak position FSS for the values of V in which the latter have converged with respect to the system sizes employed in the fitting procedure. In the points where this did not happen, the θ_t result from the susceptibility peak position fit decreased, shifting towards the data-collapse results, when smaller sizes were discarded.

According to the arguments mentioned in the preceding paragraphs, the universality class of the $T > 0$ ferromagnetic-paramagnetic transition should be the same of the corresponding transition in the classical counterpart of model Eq. (5.30). For $\alpha = 1.50$, the classical Hamiltonian is in the mean-field regime, and RG predictions, confirmed by classical Monte Carlo calculations [185], yield the estimates $\theta_t = \gamma\theta_t = 1/2$. Direct comparison with our most representative and reliable results in Table 5.2 (i.e., the one obtained via data collapse of the magnetic susceptibility) shows that our estimates for θ_t are in essential agreement with the classical prediction (with deviations outside of the estimated order of magnitude of the error only appearing for $V = 5.0$). Compatibility between our estimate

and the theoretical predictions, even for $V = 5.0$, is confirmed by the results obtained via FSS of the Binder cumulant, while the susceptibility FSS estimates, where converged, show appreciable deviations only for $V = 5.0$. Conversely, our estimates for $\gamma\theta_t$ show relatively consistent deviations (up to the order of 10%), which increase with the interaction strength.

These differences with the predicted results may be in principle due to several causes, including i) the "classical" approximation employed for the study of the susceptibility in our analysis, or ii) genuine quantum effects which introduce deviations with respect to the predicted classical behavior. However, we find it unlikely that either (i) and/or (ii) may be the dominant physical mechanism underlying the observed deviations, since both effects are essentially quantum in nature, and are expected to become weaker for larger values of V, where in contrast our results are more at odds with the classically predicted values. Indeed, for higher interaction strengths quantum effects are expected to weaken, due to both the larger value of V (in comparison to the transverse field h) and the higher temperature at which the critical region is located. This consideration leads us to the conclusion that despite these deviations (which may be caused by finite-size effects, or by higher-order corrections) the critical behavior of the model in this regime follows the classical UC.

As in the ground-state case, we find essential compatibility with the (classical) mean-field exponents at $\alpha = 0$; in particular, we match the predicted values [182] $\theta_t = \gamma\theta_t = 1/2$ up to relatively small deviations (of up to 2.5%) for the latter quantity, which also become larger in the strongly interacting regime, and are therefore likely not due to genuine quantum effects as argued above.

5.4 Conclusions and outlook

We study the ground-state and finite-temperature phase diagram and critical behavior of the long-range quantum Ising model in one spatial dimension, for values of the interaction exponent parameter of direct interest for current experiments in trapped ion setups. We perform numerically exact, large-scale PIMC simulations within both the extremely long-range region and intermediate long-range regime, respectively, employing a wide variety of finite-size scaling techniques to determine the location (i.e., the critical points) and critical exponents of both the ground-state and finite-temperature phase transitions displayed by the model.

We determine transition points and critical exponents for the ground-state ferromagnetic-paramagnetic transition. We find essential agreement with existing predictions for these quantities, where available (up to small deviations for the value of the magnetization critical exponent), and compatibility of our extremely-long-range results with the fully-connected universal properties. We then accurately estimate the position of the critical points in the finite-temperature regime for several values of the interaction strength. Here, our estimated critical exponents in the intermediate-long-range region essentially confirm the theoretical prediction of classical universality. In particular, in the intermediate long-range regime our estimated correlation length critical exponent is fully consistent with the classical predictions, while the susceptibility one displays deviations at most up to the order of 10%. Similarly, in the extremely long-range region we find compatibility with the (classical) mean-field universality class up to deviations of the order of 2.5% in the value of the correlation length critical exponent.

Beyond exploring the equilibrium phase diagram and the nature of critical points, our work is also directly relevant for another open question appearing in the context of quantum Hamiltonians with long-ranged interactions. This concerns quantum thermalization

and equilibration during coherent quantum dynamics without coupling to an environment, which appears all but settled. In the infinitely-connected limit of $\alpha = 0$ it is already well known that thermalization does not occur [190]. Furthermore, numerical works close to this infinitely-connected limit have already observed indications that thermalization could be prevented at least on the achievable time scales [191]. In order to settle this fundamental question, the understanding of the thermal equilibrium phases and properties, to which this work contributes, represents a first key step. While thermalization corresponds to ensemble equivalence of the thermal ensemble with the diagonal ensemble, capturing the long-time steady states during dynamics [192], it is also not known to which extent such long-range models exhibit ensemble equivalence on a general level. This concerns for instance the equivalence of the thermal and microcanonical ensemble, which is of central importance from the statistical physics point of view.

Chapter 6

PIMC in continuous space

As discussed in previous sections, the combination of Path Integral mapping and Monte Carlo sampling provides a powerful approach for the study of quantum spin systems. Such a technique, with the necessary modifications, can also be applied to the study of continuous-space systems, i.e., in the absence of an underlying lattice structure.

Since its introduction by the pioneering work from Pollock and Ceperley [193], which employed it to investigate the superfluid transition in ^{4}He, PIMC has become one of the most advanced and reliable methods for the analysis of these kind of systems, yielding numerically exact results at considerable system sizes and low temperatures.

This chapter presents my work on the development of an implementation of the PIMC algorithm for continuous space systems. Section 6.1 offers a brief introduction to the quantum-to-classical mapping declined in the case of continuous space Hamiltonians, while in Section 6.2 the configuration updates employed in the MC sampling process are discussed. Finally, Section 6.3 presents the testing results obtained using my PIMC implementation.

6.1 Path Integral mapping in continuous space

In the following, we will consider a many-body system of bosons of mass m in continuous space, described by a Hamiltonian $\hat{\mathcal{H}} = \hat{\mathcal{T}} + \hat{\mathcal{V}}$, where $\hat{\mathcal{T}}$ and $\hat{\mathcal{V}}$ are the kinetic and potential terms respectively.

As in the case of lattice systems, the partition function Z [Eqs. (5.4) – (5.5)] remains a central quantity for the evaluation of thermal expectation values.

Choosing the particle position basis $\{|\boldsymbol{R}\rangle\}$, where $\boldsymbol{R} = \{\boldsymbol{r}_1, ..., \boldsymbol{r}_N\}$ and $\boldsymbol{r}_i$ is the position of the ith particle for a system of N particles, and performing the Suzuki-Trotter breakup procedure displayed in Eq. (5.7), one obtains

$$Z = \int d\boldsymbol{R}_0 d\boldsymbol{R}_1 \cdots d\boldsymbol{R}_{P-1} \prod_{i=0}^{P-1} \rho(\boldsymbol{R}_i, \boldsymbol{R}_{i+1}; \tau) + \mathcal{O}(\tau) \quad \text{with } \boldsymbol{R}_P \equiv \boldsymbol{R}_0 \text{ and} \tag{6.1}$$

$$\rho(\boldsymbol{R}_i, \boldsymbol{R}_{i+1}; \tau) \equiv \int d\boldsymbol{R} \langle \boldsymbol{R}_i | e^{-\tau \hat{\mathcal{T}}} | \boldsymbol{R} \rangle \langle \boldsymbol{R} | e^{-\tau \hat{\mathcal{V}}} | \boldsymbol{R}_{i+1} \rangle. \tag{6.2}$$

Since the potential part of the Hamiltonian is diagonal in the position basis, we find

$$\langle \boldsymbol{R} | e^{-\tau \hat{\mathcal{V}}} | \boldsymbol{R}_{i+1} \rangle = e^{-\tau V(\boldsymbol{R}_{i+1})} \delta(\boldsymbol{R} - \boldsymbol{R}_{i+1}). \tag{6.3}$$

In the case of quadratic dispersion relation, i.e. $\hat{\mathcal{T}} = \frac{\hat{\boldsymbol{P}}^2}{2m}$, one can use the eigenfunctions of the momentum operator $\hat{\boldsymbol{P}}$ to evaluate the kinetic matrix element in the large system size limit as

$$\langle \boldsymbol{R}_i | e^{-\tau \hat{\mathcal{T}}} | \boldsymbol{R} \rangle = \int d\boldsymbol{P}' d\boldsymbol{P} \langle \boldsymbol{R}_i | \boldsymbol{P}' \rangle \langle \boldsymbol{P}' | e^{-\tau \frac{\hat{\boldsymbol{P}}^2}{2m}} | \boldsymbol{P} \rangle \langle \boldsymbol{P} | \boldsymbol{R} \rangle \tag{6.4}$$

$$= \int d\boldsymbol{P} \left(\frac{1}{2\pi\hbar} \right)^{Nd} \exp \left[\sqrt{-1} \frac{\boldsymbol{P}(\boldsymbol{R}_i - \boldsymbol{R})}{\hbar} - \tau \frac{\boldsymbol{P}^2}{2m} \right] \tag{6.5}$$

$$= \left(\frac{1}{4\pi\tau\lambda} \right)^{\frac{Nd}{2}} \exp \left[-\frac{(\boldsymbol{R}_i - \boldsymbol{R})^2}{4\lambda\tau} \right], \tag{6.6}$$

where d is the dimensionality of the system and $\lambda = \hbar^2/2m$. Joining Eq. (6.3) and Eq. (6.6), the generic matrix element in Eq. (6.2), also known as *propagator* becomes

$$\rho(\boldsymbol{R}_i, \boldsymbol{R}_{i+1}; \tau) = \underbrace{\left(\frac{1}{4\pi\tau\lambda} \right)^{\frac{Nd}{2}} \exp \left[-\frac{(\boldsymbol{R}_i - \boldsymbol{R}_{i+1})^2}{4\lambda\tau} \right]}_{\rho_F} \underbrace{\exp \left[-\tau V(\boldsymbol{R}_{i+1}) \right]}_{\exp[g(V(\boldsymbol{R}_{i+1}))]}. \tag{6.7}$$

Then, ρ_F is the propagator of N free particles. Several choices are available for the interaction each providing a different level of accuracy (i.e. higher or smaller Trotter breakup errors as a function of τ). In our work, we exploit the 4th order approximation introduced in Ref. [194], which is considerably more accurate, than the so called *primitive approximation* in Eq. (6.7).

The partition function then becomes

$$Z = \int d\boldsymbol{R}_0 d\boldsymbol{R}_1 ... d\boldsymbol{R}_{P-1} (4\pi\lambda\tau)^{-\frac{dNP}{2}} \exp \left[-\sum_{s=1}^{P} \frac{(\boldsymbol{R}_{s-1} - \boldsymbol{R}_s)^2}{4\lambda\tau} + g[V(\boldsymbol{R}_s)] \right]. \tag{6.8}$$

The model resulting from the quantum-to-classical mapping can be interpreted as a system of polymers created by linking *beads*. The latter may move freely in space but reside at fixed positions in imaginary time (see Fig. 6.1). In this description, each particle is composed by P beads, which interact with nearest linked beads through a spring like potential while beads at the same time slice s interact through the classical potential $g[V(\boldsymbol{R}_s)]$.

6.2 PIMC sampling. The Worm Algorithm

As in the case of lattice systems, performing the integrals in Eq. (6.8) for a many particles becomes prohibitive, suggesting the use of MC sampling to compute Z and the thermal values of observables of interest.

The most basic sampling procedure which can be adopted to this end employs *closed line* moves: these are updates in which the shape of the polymers is modified without breaking them or changing their connectivity (an example of such moves is the "wiggle" update discussed in the next paragraphs).

In order to sample sectors of the configuration space with different connectivity properties (which is crucial, for instance, to obtain accurate results for observables associated to superfluidity) one may complement closed-line moves with ad-hoc updates which change polymer connectivity [193]. While this choice in principle ensures ergodicity, in practice other, more effective updates schemes have emerged over the years, the most advanced being *Worm Updates* [195, 196], inspired by the original incarnation for lattice systems [197].

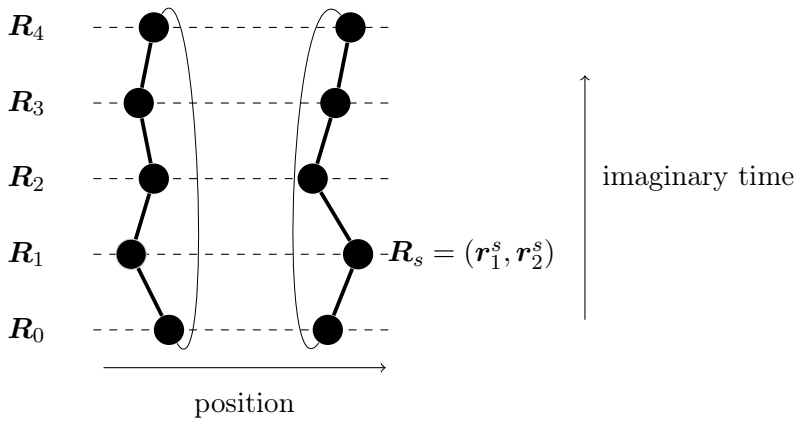

Figure 6.1: Equivalent classical system of interacting beads. In this case, the system is composed of 2 particles and P=5. The continuous black lines connecting beads (links) represent propagators between different time slices.

Worm updates work by sampling an extended configuration space, in which the polymers (also known as world lines) may be either closed or open (i.e., with one or more propagators missing). Most observables (including energies, superfluid properties, density profiles) are measured in configurations containing only the former. On the other hand, performing updates in configurations containing the latter allows to naturally vary polymer connectivity (and therefore, reliable investigating superfluid properties) to compute observables which would otherwise be very complicated to access (e.g., single particle density matrices) and to straightforwardly perform simulations in the Grand Canonical ensemble.

In the following, the types of moves employed in our implementation of the Worm Algorithm are discussed.

Open/Close. The open update is attempted on configurations with all worldlines closed. The update attempts to remove the propagators linking two beads chosen uniformly on the same worldline (see Fig. 6.2). If the update is accepted (with the probability prescribed by the Metropolis sampling scheme in Eq. (5.21)) the resulting configuration will contain an open worldline, also known as worm.

The close update inverts the previous one, extracting random positions for the missing beads and constructing the connecting propagators between the two open ends (also known as heads) of the worm (see Fig. 6.2).

Advance/Recede. This move attempts to shift forward or backward in imaginary time one of the two worm heads, by deleting existing beads or randomly extracting new ones where the distance between the heads increase or decreases, respectively (Fig. 6.3).

Wiggle. In the wiggle update one attempts to change the position of a finite number of beads belonging to a polymer in a closed-worldline configuration (see Fig. 6.4).

Insert/Remove. This pair of updates is employed when performing simulations in the Grand Canonical ensemble. The former is only applicable to closed-worldline configura-

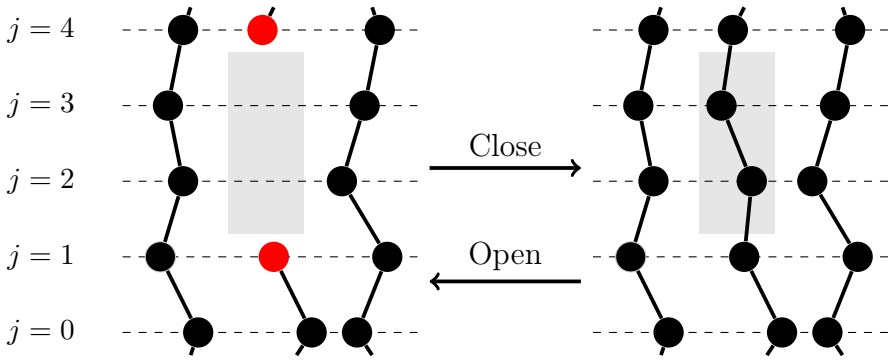

Figure 6.2: Open-Close updates. The worm heads are the red painted beads. Diferent imaginary time slices are labeled by j.

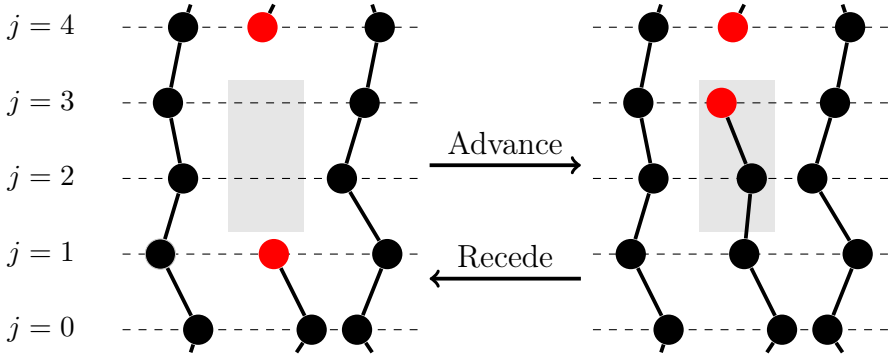

Figure 6.3: Advance-Recede updates.

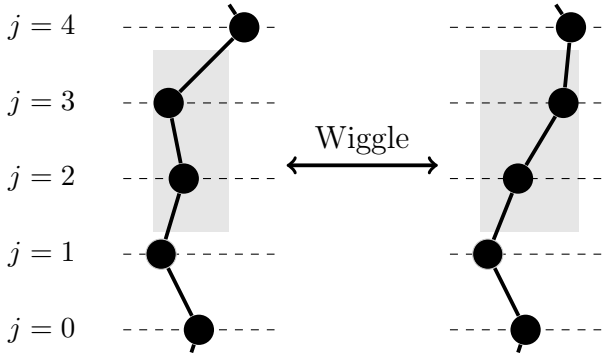

Figure 6.4: Wiggle update.

tions, and attempts to create a new open worldline composed by $M < P$ beads placed at randomly extracted positions. The latter attempts to delete an open worldline, if present, as long as the worm is composed at most by M beads (to ensure respect of the detailed balance conditions). See Fig. 6.5 for an example of such move in action.

Swap. This update is applicable to off-diagonal configurations only. Let j be the time slice of one of the worm heads. One consider the time slice $j + M$(because of imaginary periodicity, this addition is understood modulo P) and choose randomly a bead α in this time slice. The update attempts to connect the worldline where the worm resides with the worldline containing α. In order to do this, $M - 1$ beads before α are removed and

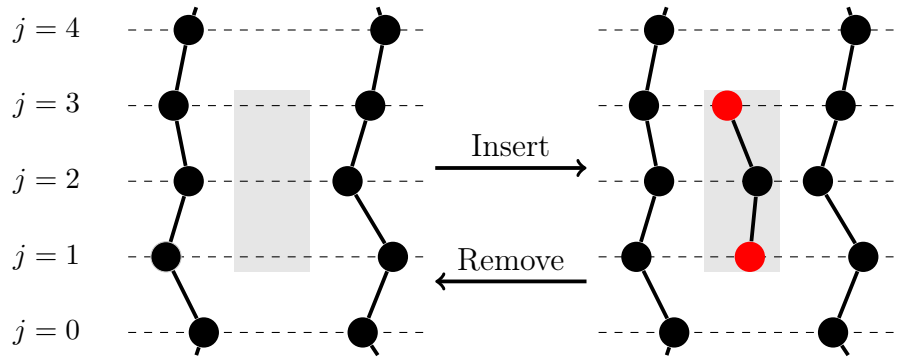

Figure 6.5: Insert-Remove updates.

replaced by randomly extracted position beads and a new link between the worm head and the replaced beads is created as depicted in Fig. (6.6).

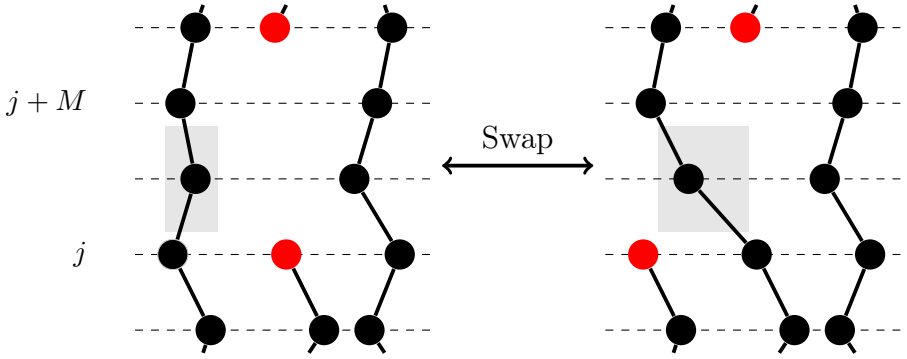

Figure 6.6: Swap update.

6.3 Numerical testing

In this section we report the results of several high-level tests that we performed to verify the reliability of our implementation of the worm algorithm.

We simulated a system of bosons interacting with a soft-core potential described by the Hamiltonian

$$H = -\frac{1}{2}\sum_{i=1}^{N}\Delta_i^2 + D\sum_{i>j}\Theta(|1 - r_{ij}|), \tag{6.9}$$

where Θ is the Heaviside function, r_{ij} is the distance between particles i and j, all lengths are expressed in units of the soft-core diameter a, and all energies are expressed in units of $\epsilon_0 = \hbar^2/ma^2$. The system is enclosed in a cell with periodic boundary conditions, of sides (L_x, L_y). The study is performed in the Grand Canonical ensemble, we denote by N the average number of particles and express the density ρ in term of the dimensionless parameter $r_s = 1/\sqrt{\rho a^2}$.

In order to reproduce published results [198, 199] we performed simulations for $D = 5$ and $(L_x, L_y) = (11.855, 10.267)$ in the ground-state regime for different values of the chemical potential μ.

At small values of the later (i.e. low particle number) the system is in a *superfluid* state, characterized by long-range particle exchange cycles. This phase can be identified

by computing the *superfluid fraction* ρ_s, i.e., the amount of particles involved in superfluid exchange cycles. This quantity is immediately accessible to PIMC simulations via the well-known winding number estimator [200].

At high density the system displays long-range crystalline order, with superfluid exchanges been suppressed; such a state can be straight forwardly characterized by computing the structure factor

$$S(\boldsymbol{k}) = \frac{|\rho_{\boldsymbol{k}}|^2}{N}; \qquad \rho_{\boldsymbol{k}} = \int e^{-i\boldsymbol{k}\cdot\boldsymbol{r}}\rho(\boldsymbol{r}). \tag{6.10}$$

where $\rho(\boldsymbol{r})$ is the particle density profile. This quantity will display peaks at values of the momentum $\boldsymbol{k}$ associated to the type of established crystalline order, while no such feature will appear for liquid (and superfluid) phases.

For intermediated values of μ, the ground state of the system features the coexistence of superfluidity and crystalline order, in a state known as supersolid and characterized by nonzero values for both the observables introduced above.

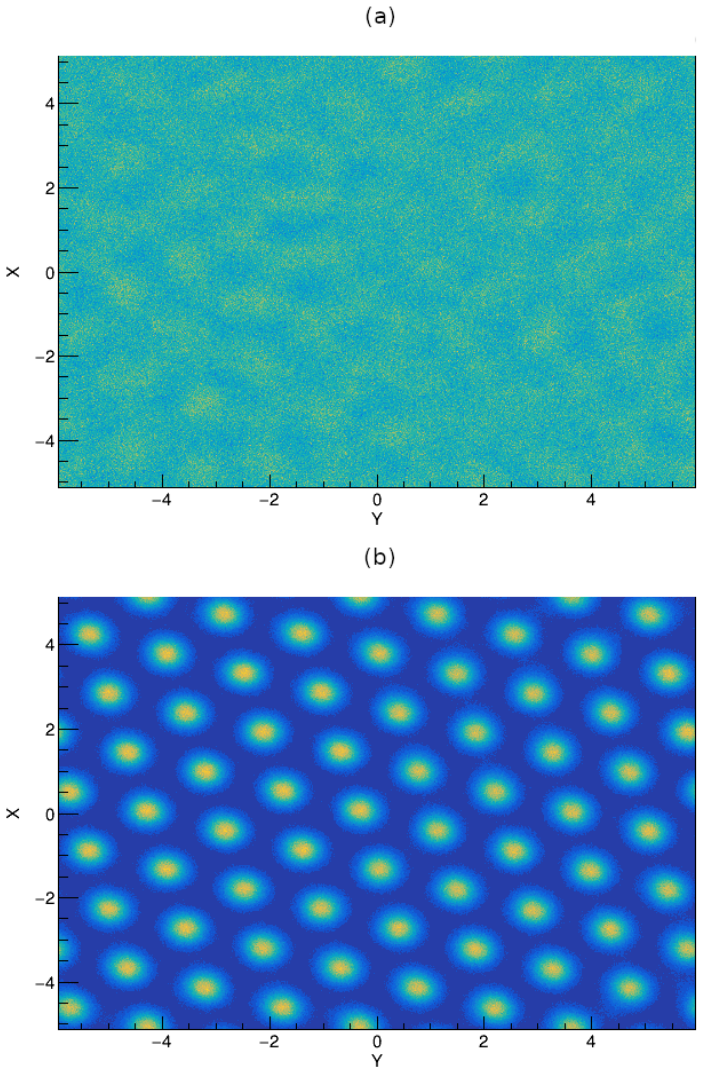

Figure 6.7: Obtained density profiles for different values of μ. (a) $\mu = 37$ and $r_s = 0.62$; (b) $\mu = 42$ and $r_s = 0.55$.

Figure 6.8 displays our results for ρ_s and $S(\boldsymbol{k}_0)$, with $\boldsymbol{k}_0 = [0.866\frac{2\pi}{a}, 0]$ being the peak

position associated to the crystalline order displayed by the system in the regime discussed above. A direct inspection immediately reveals the presence of the three regimes discussed above as diagnosed by the interplay between the two order parameters. A comparison of

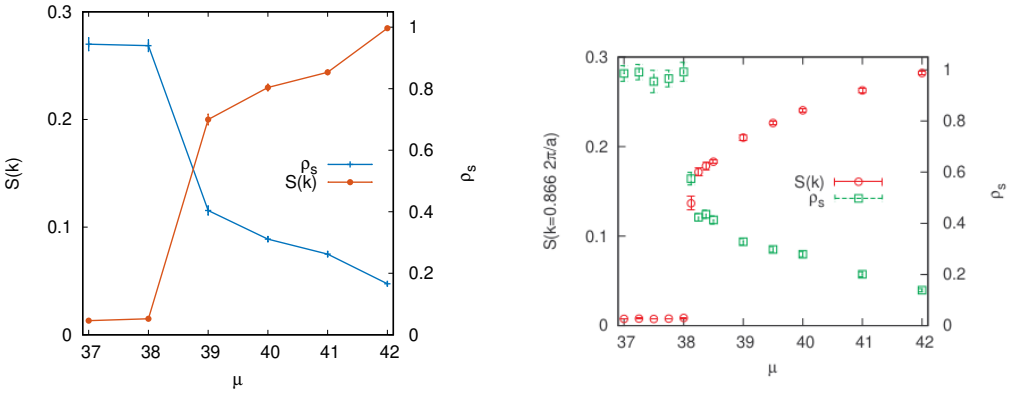

Figure 6.8: Static structure factor $S(\boldsymbol{k})(\boldsymbol{k} = [0.866\frac{2\pi}{a}, 0]$) and superfluid fraction ρ_s across the superfluid-supersolid transition. Results correspond to $D = 5$ and $(Lx, Ly) = (11.855, 10.267)$. Our calculated values are presented in the left panel while the right panel plot is taken from Ref. [199]

our results with the ones available in the literature [[199]; Fig. 6.8(right panel)] reveals essential compatibility between the two sets of points.

In order to further test our code, we also performed finite-temperature calculations for $(Lx, Ly) = (4.7958, 4.7958)$ and fixed particle number $N = 92 \pm 1$ with the aim of comparing with existing results [198]. The outcome of our calculations is displayed in Fig. 6.9. In the limit of high temperature the superfluid ground state is expected to decay to a nor-

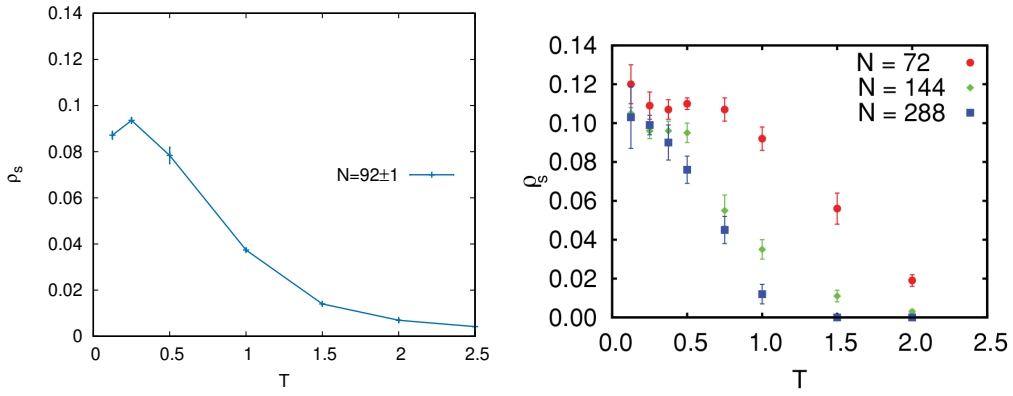

Figure 6.9: Superfluid fraction as a function of T (in units of ϵ_0) for a system of soft disks with $D = 5$. Here, μ is set so that $rs = 0.5$. Left panel results correspond to an average number of particles $N = 92 \pm 1$ with $(Lx, Ly) = (4.7958, 4.7958)$ calculated using our implementation. Right panel plot is taken from Ref. [198]

mal (classical liquid), a behaviour fully caught by our numerical simulations (Fig. 6.9 (left panel)). We also note essential agreement with existing predictions (Fig. 6.9 (right panel)).

6.4 Conclusions

We have benchmarked our implementation of the PIMC method in continuous space and the obtained results agree well with previous calculations. This allows us to study systems of interacting bosons with high degree of accuracy in an exact manner. The method does not suffer from critical slowing down which permits to characterize the system near a second order phase transition in high dimensional systems. Future perspectives include the study of experiments showing supersolidity and theoretical studies of bilayer systems.

Part III

Appendix

Appendix A

Stability of quantum scars

A.1 Properties of the PXP and the other constrained models

In this section, we summarize the properties of the spectrum of the PXP ($\alpha = 1$) and the other constrained model with $\alpha > 1$ of their perturbations. For any $\alpha \geq 1$, the Hamiltonian H_0^α and the perturbation V^α commute with the space reflection symmetry I and anticommute with the particle-hole symmetry $C_{ph} = \prod_i \sigma_i^z$. This fact has some important consequences, that hold for any Hamiltonian with these symmetries:

- all the eigenstates with $E \neq 0$ are found in pairs of opposite energies (*doublets*), related by particle-hole symmetry ($C_{ph} |E\rangle = |-E\rangle$);
- states with $E = 0$ can be classified as eigenstates of C_{ph} (*singlets*);
- the subspace of zero-energy eigenstates is exponentially large in L;
- the singlets have same eigenvalue with respect to C_{ph} and I: this means that the zero-energy space is the direct sum of two subspaces with $C_{ph} = I = \pm 1$;
- if $|\psi\rangle$ and $|\phi\rangle$ are two singlet eigenstates of H_0, then $\langle\phi|V|\psi\rangle = 0$. This holds even if $\langle\phi|\psi\rangle \neq 0$ (or even if $|\psi\rangle = |\phi\rangle$).

A.1.1 Scars

Here we report the properties of the scars under the action of I and C_{ph}. For the PXP model ($\alpha = 1$), they satisfy:

$$I |\Gamma_{12}\rangle = (-1)^{L/2-1} |\Gamma_{12}\rangle \tag{A.1}$$
$$I |\Gamma_{11}\rangle = (-1)^{L/2} |\Gamma_{11}\rangle \tag{A.2}$$
$$C_{ph} |\Gamma_{11}\rangle = (-1)^{L/2} |\Gamma_{11}\rangle \tag{A.3}$$
$$I |\Gamma_{21}\rangle = (-1)^{L/2-1} |\Gamma_{21}\rangle \tag{A.4}$$
$$I |\Gamma_{22}\rangle = (-1)^{L/2} |\Gamma_{22}\rangle \tag{A.5}$$
$$C_{ph} |\Gamma_{22}\rangle = (-1)^{L/2} |\Gamma_{22}\rangle . \tag{A.6}$$

The scars defined in Section 3.4.2 for $\alpha > 1$ and $L = (\alpha + 2)n + 3$ satisfy

$$I |\psi_\alpha^{(\pm 3)}\rangle = (-1)^n |\psi_\alpha^{(\pm 3)}\rangle \tag{A.7}$$
$$C_{ph} |\psi_\alpha^{(\pm 3)}\rangle = |\psi_\alpha^{(\mp 3)}\rangle . \tag{A.8}$$

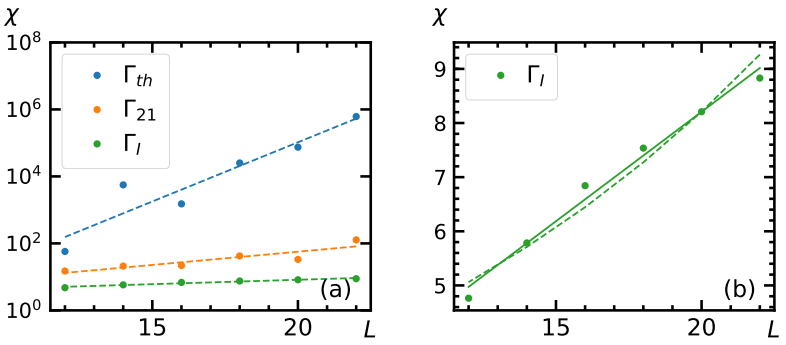

Figure A.1: Scaling of the fidelity susceptibility with system size, for the perturbation V'. The results shown refer to the states (a) $|\Gamma_{th}\rangle$, $|\Gamma_{21}\rangle$ and (b) $|\Gamma_I\rangle$ with open boundary conditions. Dashed lines are obtained from fits with an exponential scaling, solid lines with linear scaling. Similarly to the results for the perturbation V shown in Fig. 3.2, also in this case the scaling is exponential for the states $|\Gamma_{th}\rangle$, $|\Gamma_{21}\rangle$ (in agreement with ETH) and is linear for the state $|\Gamma_I\rangle$.

A.2 Stability to other perturbations

We report here the data of the fidelity susceptibility of the scars and of a generic thermal eigenstate in the PXP model for a different perturbation V', defined as

$$V' = \sum_{i=2}^{L-3} P_{i-2}\, \sigma^+_{i-1}\sigma^-_i\, \sigma^+_{i+1} P_{i+2} + \text{H.c.} \tag{A.9}$$

The perturbation is again chosen in such a way to have the same properties under symmetry transformations as the PXP Hamiltonian H_0, i.e. $IV'I = V$, $C_{ph}V'C_{ph} = -V'$. The results in Fig. A.1 show the same behaviour that we observed for the perturbation V in the main text: the fidelity susceptibility grows exponentially with system size for the states $|\Gamma_{th}\rangle$, $|\Gamma_{21}\rangle$ and linearly for the state $|\Gamma_{th}\rangle$.

A.3 Exact scars in the PXP model – properties of the edges

In this section we recall some properties of the scars of Eq. (3.5) and (3.7), and we comment on the profile of the energy density. As was noticed in Ref. [63], the PXP Hamiltonian can be written as a sum of two parts: a part which contains two-body interactions between blocks, and one with single-block terms only. The two-body terms annihilate the scars (we refer to the appendix of Ref. [63] for the proof), while the remaining terms are

$$H' = \sum_b [|10\rangle\langle 00| + |01\rangle\langle 00| + h.c.]_b. \tag{A.10}$$

A more convenient expression is obtained by defining the states

$$|\pm\rangle = \frac{1}{2}(|01\rangle + |10\rangle + \sqrt{2}\,|00\rangle), \tag{A.11}$$

$$|\mathbf{0}\rangle = \frac{1}{\sqrt{2}}(|10\rangle - |01\rangle). \tag{A.12}$$

The Hamiltonian H' has the form

$$H' = \sqrt{2}\sum_b (|+\rangle\langle+| - |-\rangle\langle-|). \tag{A.13}$$

This expression is useful to interpret the profile of the energy density of the scars. After this change of basis and a gauge transformation with the unitary matrix $V = \frac{1}{\sqrt{2}}\begin{pmatrix}1 & 1\\ 1 & -1\end{pmatrix}$, the new matrices have the form

$$A^+ = V\frac{1}{2}(A^{01} + A^{10} + \sqrt{2}A^{00})V^{-1} = \begin{pmatrix}0 & \sqrt{2}\\ 0 & 0\end{pmatrix}, \tag{A.14}$$

$$A^- = V\frac{1}{2}(A^{01} + A^{10} - \sqrt{2}A^{00})V^{-1} = \begin{pmatrix}0 & 0\\ \sqrt{2} & 0\end{pmatrix}, \tag{A.15}$$

$$A^{\mathbf{0}} = V\frac{1}{\sqrt{2}}(A^{10} - A^{01})V^{-1} = \begin{pmatrix}1 & 0\\ 0 & 1\end{pmatrix}, \tag{A.16}$$

and the new boundary vectors are

$$v_1' = Vv_1 = \begin{pmatrix}1\\ 0\end{pmatrix}, \tag{A.17}$$

$$v_2' = Vv_2 = \begin{pmatrix}0\\ 1\end{pmatrix}. \tag{A.18}$$

Now each block can be interpreted as a spin-1 variable with states $+, \mathbf{0}, -$ indicating the S_z component, and the Hamiltonian H' corresponds to the magnetization in the z direction. The form of the matrices $A^+, A^-, A^{\mathbf{0}}$, allows to easily see which are the non-zero components in the local S_z basis: they are the ones with the structure of a "dilute antiferromagnet", i.e. with alternating + and − and an arbitrary number of **0**s in between. This structure is a renowned feature of the AKLT state, whose relation with the MPS scars has been already pointed out in Ref. [63]. In open boundary conditions, the boundary vectors fix the sign of the first non-zero spin: on the left v_1' (v_2') constrains it to be in a + (−) state and vice versa for the vector on the right. Therefore, the components of the state Γ_{12} have a number of +s that exceeds the number of −s by one, so its energy is $E = \sqrt{2}$ (and vice versa for Γ_{21}, with $E = -\sqrt{2}$). The states Γ_{11} and Γ_{22}, on the other hand, have the same number of −s and +s, so they have energy $E = 0$. The energy density profiles reported in Ref. [63] can be understood as well from this construction: they correspond to the magnetization profile of the dilute antiferromagnet. In the bulk, the local magnetization averages to 0, while on the boundary it is affected by the choice of the boundary vector.

A.4 Exact scars with $E = \sqrt{3}$ – Proof

In this section we prove that the following state is an exact scar with energy $E = \sqrt{3}$

$$|\psi_\alpha^{(3)}\rangle = \sum_{\vec{s}} \left[(1,0)^T \cdot N^{s_1} M^{s_2} \dots M^{s_{2n}} N^{s_{2n+1}} \cdot (0,1)\right] |\vec{s}\rangle \tag{A.19}$$

where $s_1, s_2, \dots s_{2n+1}$ label the states of the blocks and

$$M^s = \begin{cases} 1 & \text{if } s = 00\dots00 \\ 0 & \text{otherwise,} \end{cases} \tag{A.20}$$

$$N^0 = \begin{pmatrix} 0 & \sqrt{3} \\ 0 & 0 \end{pmatrix}, \qquad N^L = \begin{pmatrix} 0 & 1 \\ 0 & 1 \end{pmatrix}, \tag{A.21}$$

$$N^C = \begin{pmatrix} 1 & 1 \\ 0 & -1 \end{pmatrix}, \qquad N^R = \begin{pmatrix} -1 & 1 \\ 0 & 0 \end{pmatrix}. \tag{A.22}$$

The indices $0, L, C, R$ are the state of three-site block, with the following notation: $|0\rangle = |000\rangle$, $|L\rangle = |100\rangle$, $|C\rangle = |010\rangle$, $|R\rangle = |001\rangle$.

The matrices in Eqs. A.21 and A.22 satisfy

$$N^R N^L = 0, \qquad (N^0 + N^L)(N^R + N^0) = 0. \tag{A.23}$$

The first equation implies that the state satisfies the blockade constraint. We can split the Hamiltonian in two parts: $H = H_M + H_N$ where H_M (H_N) flips only sites in the M (N) blocks.

We first prove that $H_M |\psi_\alpha^{(3)}\rangle = 0$. Consider a single term $P_{i-\alpha} \dots P_{i-1} X_i P_{i+1} \dots P_{i+\alpha}$ where i belongs to a block of type M: if i is not the first or last site of the block, it can only be flipped if both neighbouring N blocks are in the state 0. However, this never happens because $N^0 M^s N^0 = 0$. If i is the first site of the blocks, these two conditions must hold for it to be flippable: (i) the previous block must be in state 0; (ii) the following block must be either in state 0 or R. But $N^0 M^s N^0 = N^0 M^s N^R = 0$, so this Hamiltonian term annihilates the state. Similarly, using $N^0 M^s N^0 = N^L M^s N^0 = 0$, we find that the last site of the block cannot be flipped. This means that the sites in the M blocks are all "frozen" in the 0 state and concludes the proof that $H_M |\psi_\alpha^{(3)}\rangle = 0$.

We now consider H_N:

$$H_N |\psi_\alpha^{(3)}\rangle = \sum_b \Big[\big(|0\rangle\langle R| \big)_b \big(1 - |L\rangle\langle L| \big)_{b+1} + \big(1 - |R\rangle\langle R| \big)_{b-1} \big(|0\rangle\langle L| \big)_b + \big(|0\rangle\langle R| \big)_b + h.c. \Big] |\psi_\alpha^{(3)}\rangle \tag{A.24}$$

where $b = 1, \dots n+1$ labels the blocks of type N. From the relations $N^R N^L = N^0 N^L + N^R N^0 = 0$, we find that all the terms involving more than one block cancel and we are left with

$$H_N |\psi_\alpha^{(3)}\rangle = H' |\psi_\alpha^{(3)}\rangle . \tag{A.25}$$

$$H' = \sum_b \Big[|0\rangle \big(\langle R| + \langle C| + \langle L| \big) + h.c. \Big]_b . \tag{A.26}$$

Now, to prove that $H' |\psi_\alpha^{(3)}\rangle = \sqrt{3} |\psi_\alpha^{(3)}\rangle$, it is useful to change basis and define:

$$|\pm\rangle = \frac{|L\rangle + |C\rangle + |R\rangle \pm \sqrt{3} |0\rangle}{\sqrt{6}}, \tag{A.27}$$

$$|l\rangle = \frac{|C\rangle - |L\rangle}{\sqrt{2}}, \qquad |r\rangle = \frac{|C\rangle - |R\rangle}{\sqrt{2}}. \tag{A.28}$$

In this new basis the matrices have the form

$$N^+ = \begin{pmatrix} 0 & \sqrt{6} \\ 0 & 0 \end{pmatrix}, \qquad N^- = 0, \tag{A.29}$$

$$N^l = \begin{pmatrix} 1/\sqrt{2} & 0 \\ 0 & -\sqrt{2} \end{pmatrix}, \; N^r = \begin{pmatrix} \sqrt{2} & 0 \\ 0 & -1/\sqrt{2} \end{pmatrix}. \tag{A.30}$$

and the Hamiltonian H'

$$H' = \sum_b \left[\sqrt{3} \left|+\right\rangle \left\langle+\right| - \sqrt{3} \left|-\right\rangle \left\langle-\right| \right]_b \tag{A.31}$$

H' is diagonal in the new basis $\{|+\rangle, |-\rangle, |l\rangle, |r\rangle\}$. It is now sufficient to prove that all the non zero-components of $|\psi\rangle$ in the new basis have a one and only one block in $|+\rangle$ and all the others are in $|l\rangle$ or $|r\rangle$. This can be understood from the fact that (i) $N^+ N^{\alpha_1} \dots N^{\alpha_p} N^+ = 0$ (for any string in between) and that (ii) any string of matrices without N^+ is diagonal, so it annihilates when contracted with the boundary vectors $(1,0)^T$, $(0,1)$. The energy density profile of this state is then easy to understand in these basis: all the three-site blocks have the same energy density, because the '+' can be located anywhere in the chain, while the other sites have energy density 0. This contrasts with the MPS scars found in Ref. [63]: while there the energy density is localized on the edges because of the structure of dilute antiferromagnet, here the construction resembles a spin wave with a delocalized excitation.

A.5 Exact scars with $E = \sqrt{2}$, $\alpha = 3$

We now consider the case $\alpha = 3$ and construct exact eigenstates with $E = \pm\sqrt{2}$ as matrix product states with finite bond dimensions. They are constructed by assembling position dependent matrices in a periodic pattern, illustrated in Fig. A.2.

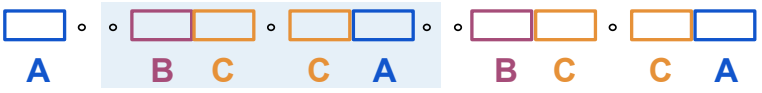

Figure A.2: Structure of an MPS for $L = 24$. The blocks are made of two sites. Empty dots are sites in the state 0. The structure of the state for generic system sizes is based on the periodic repetition of the pattern $0BC0CA0$ (highlighted in the picture).

The matrices A, B, C are defined on two-site blocks and have bond dimension 2. The dots represent empty sites. The pattern (0BC0CA0) that is repeated periodically consists of 11 sites. The first and last two sites of the open chain have to be in a block of type A or B. Therefore we have 4 possible states, labelled by the first and last block:

- $|\phi^{(2)}_{AB}\rangle$, for $L = 6 + 11n$;
- $|\phi^{(2)}_{BA}\rangle$, for $L = 9 + 11n$;
- $|\phi^{(2)}_{AA}\rangle$ and $|\phi^{(2)}_{BB}\rangle$, for $L = 13 + 11n$.

The matrices for the eigenvalue $E = \sqrt{2}$ are defined as

$$A^{00} = \begin{pmatrix} 0 & 1/\sqrt{2} \\ 0 & 1 \end{pmatrix}, \qquad A^{10} = \begin{pmatrix} 1/\sqrt{2} & 1/2 \\ 0 & 0 \end{pmatrix}, \tag{A.32}$$

$$A^{01} = \begin{pmatrix} -1/\sqrt{2} & 1/2 \\ 0 & 0 \end{pmatrix} \tag{A.33}$$

$$B^{00} = \begin{pmatrix} 1 & 1/\sqrt{2} \\ 0 & 0 \end{pmatrix}, \qquad B^{10} = \begin{pmatrix} 0 & 1/2 \\ 0 & 1/\sqrt{2} \end{pmatrix}, \tag{A.34}$$

$$B^{01} = \begin{pmatrix} 0 & 1/2 \\ 0 & -1/\sqrt{2} \end{pmatrix} \tag{A.35}$$

$$C^{00} = \begin{pmatrix} 0 & 0 \\ 1 & 0 \end{pmatrix}, \qquad C^{10} = \begin{pmatrix} 0 & 1/\sqrt{2} \\ 0 & 0 \end{pmatrix}, \tag{A.36}$$

$$C^{01} = \begin{pmatrix} 0 & -1/\sqrt{2} \\ 0 & 0 \end{pmatrix} \tag{A.37}$$

The boundary vectors are obtained by contracting the extremal matrices with $(1,0)^T$ on the left and $(0,1)$ on the right. The states $|\phi_{rs}^{(-2)}\rangle = C_{ph}\,|\phi_{rs}^{(2)}\rangle$ $(r,s = A,B)$ are other exact scars with energy $E = -\sqrt{2}$.

These scars satisfy the following properties:

$$I\,|\phi_{AB}^{(\pm 2)}\rangle = -\,|\phi_{AB}^{(\pm 2)}\rangle \tag{A.38}$$

$$I\,|\phi_{BA}^{(\pm 2)}\rangle = -\,|\phi_{BA}^{(\pm 2)}\rangle \tag{A.39}$$

$$I\,|\phi_{AA}^{(\pm 2)}\rangle = |\phi_{BB}^{(\pm 2)}\rangle \tag{A.40}$$

$$I\,|\phi_{BB}^{(\pm 2)}\rangle = |\phi_{AA}^{(\pm 2)}\rangle\,. \tag{A.41}$$

A.5.1 Proof

We first prove that the state above satisfies the constraints. The conditions are: $B^r C^s = C^r A^s = 0$ for $r = 01, 10$ and $s = 01, 10$, $C^{01}C^{01} = C^{01}C^{10} = C^{10}C^{10} = 0$, and $A^{01}B^{10} = 0$. It is straightforward to check that all of them are satisfied by the matrices A, B and C.

We now define the local Hamiltonian term $h_i = P_{i-3}P_{i-2}P_{i-1}X_iP_{i+1}P_{i+2}P_{i+3}$ and prove that $h_i\,|\psi_{\alpha=3}\rangle = 0$ when i is one of the sites between two C blocks. To prove this, we note that $C^{00}C^{00} = 0$, which immediately implies $P_{i-2}P_{i-1}P_{i+1}P_{i+2}\,|\psi_{\alpha=3}\rangle = 0$. Similarly, we can prove that $h_i\,|\psi_{\alpha=3}\rangle = 0$ when i is one of the sites between an A and a B block by noting that $A^{00}B^{00} = 0$ so the projectors in h_i annihilate the state $|\psi_{\alpha=3}\rangle$.

The next step is proving $h_i\,|\psi_{\alpha=3}\rangle = 0$ for i belonging to the C blocks. To set the notation, we label the two-site blocks (of types A, B, C) in the chains with indices $b = 0, 1, 2, \ldots, N_b$ from left to right. We define Γ_A as the set of integers b such that the b-th block is of type A, and similarly for Γ_B and Γ_C. We also define the operator P_b^s which projects the block b in the state $|s\rangle$.

With this notation, we obtain the following equation

$$\begin{aligned}\sum_{b\in\Gamma_C}\sum_{i\in b} h_i = \sum_{b,b+1\in\Gamma_C} & P_{b-1}^{00}\,|00\rangle_b\,(\langle 10| + \langle 01|)_b P_{b+1}^{00} \\ & + P_b^{00}\,|00\rangle_{b+1}\,(\langle 10| + \langle 01|)_{b+1} P_{b+2}^{00} \\ & + P_{b-1}^{00}(|10\rangle + |01\rangle)_b\,\langle 00|_b\,P_{b+1}^{00} \\ & + P_b^{00}(|10\rangle + |01\rangle)_{b+1}\,\langle 00|_{b+1}\,P_{b+2}^{00}.\end{aligned} \tag{A.42}$$

The sum in the right hand side runs over the indices such that both b and $b+1$ are blocks of type C. The first two terms of the sum annihilate $|\psi_{\alpha=3}\rangle$ because $C^{01} + C^{10} = 0$, the last two terms because $C^{00}C^{00} = 0$.

From the observations we made so far, we have now obtained that

$$H\left|\psi_{\alpha=3}\right\rangle = \sum_{b\in\Gamma_A\cup\Gamma_B}\sum_{i\in b} h_i\left|\psi_{\alpha=3}\right\rangle. \tag{A.43}$$

We can rewrite the action of these terms as

$$\sum_{b\in\Gamma_A\cup\Gamma_B}\sum_{i\in b} h_i\left|\psi_{\alpha=3}\right\rangle = \left(H_{non-int} - H_{int}\right)\left|\psi_{\alpha=3}\right\rangle. \tag{A.44}$$

The Hamiltonian $H_{non-int}$ contains the terms

$$H_{non-int} = \sum_{b\in\Gamma_A} P^{00}_{b-1}[\left|00\right\rangle\left(\left\langle 10\right| + \left\langle 01\right|\right) + h.c.]_b + \sum_{b\in\Gamma_B}[\left|00\right\rangle\left(\left\langle 10\right| + \left\langle 01\right|\right) + h.c.]_b P^{00}_{b+1}, \tag{A.45}$$

where, for the sake of brevity, in our notation for the boundary terms we choose to define $P^{00}_{-1}\equiv 1$, $P^{00}_{N_b+1}\equiv 1$. The Hamiltonian H_{int} reads

$$H_{int} = \sum_{\substack{b\in\Gamma_A\\ b+1\in\Gamma_B}} P^{00}_{b-1}[\left|00\right\rangle\left\langle 01\right| + h.c.]_b P^{10}_{b+1} + P^{01}_b[\left|00\right\rangle\left\langle 10\right| + h.c.]_{b+1}P^{00}_{b+2}. \tag{A.46}$$

By noting that $A^{01}B^{10}=0$ and $C^{00}(A^{00}B^{10}+A^{01}B^{00})C^{00}=0$, we find that $H_{int}\left|\psi_{\alpha=3}\right\rangle = 0$.

To conclude our proof, we now have to demonstrate that $H_{non-int}\left|\psi_{\alpha=3}\right\rangle = \sqrt{2}\left|\psi_{\alpha=3}\right\rangle$. We define the states

$$\left|e\right\rangle = \frac{\left|10\right\rangle + \left|01\right\rangle}{\sqrt{2}} \qquad \left|o\right\rangle = \frac{\left|10\right\rangle - \left|01\right\rangle}{\sqrt{2}}, \tag{A.47}$$

$$\left|\pm\right\rangle = \frac{\left|00\right\rangle \pm \left|e\right\rangle}{\sqrt{2}}, \qquad \left|0\right\rangle = \left|00\right\rangle. \tag{A.48}$$

We now perform the following changes of basis: on the A and B blocks, we use the (non-orthogonal) states $\left|+\right\rangle, \left|o\right\rangle, \left|0\right\rangle$, such that the new matrices of the MPS have the form

$$\tilde{A}^{+} = \begin{pmatrix} 0 & 1\\ 0 & 0\end{pmatrix}, \qquad \tilde{A}^{o} = \begin{pmatrix} 1 & 0\\ 0 & 0\end{pmatrix}, \tag{A.49}$$

$$\tilde{A}^{0} = \begin{pmatrix} 0 & 0\\ 0 & 1\end{pmatrix} \tag{A.50}$$

$$\tilde{B}^{+} = \begin{pmatrix} 0 & 1\\ 0 & 0\end{pmatrix}, \qquad \tilde{B}^{o} = \begin{pmatrix} 0 & 0\\ 0 & 1\end{pmatrix}, \tag{A.51}$$

$$\tilde{B}^{0} = \begin{pmatrix} 1 & 0\\ 0 & 0\end{pmatrix}, \tag{A.52}$$

while on the C blocks we use $\left|0\right\rangle$, $\left|e\right\rangle$ and $\left|o\right\rangle$, with the matrices

$$\tilde{C}^{0} = \begin{pmatrix} 0 & 0\\ 1 & 0\end{pmatrix}, \qquad \tilde{C}^{e} = 0, \qquad \tilde{C}^{o} = \begin{pmatrix} 0 & 1\\ 0 & 0\end{pmatrix}. \tag{A.53}$$

We now merge the pairs of consecutive C blocks. The only non-zero matrices for the superblock are

$$\tilde{G}^{0,o} = \begin{pmatrix} 0 & 0 \\ 0 & 1 \end{pmatrix}, \qquad \tilde{G}^{o,0} = \begin{pmatrix} 1 & 0 \\ 0 & 0 \end{pmatrix}. \tag{A.54}$$

The components of $|\psi_{\alpha=3}\rangle$ now have the form

$$|\psi_{\alpha=3}\rangle = \sum_{\vec{s}=(s_0,\ldots,s_{N_b})} c_{\vec{s}} |s_0\rangle \otimes |s_1\rangle \cdots \otimes |s_{N_b}\rangle \tag{A.55}$$

where the sum runs over the three new states of the basis for each component s_b and

$$c_{\vec{s}} = \begin{pmatrix} 1 & 0 \end{pmatrix} \left(\ldots \tilde{B}^{s_{b-1}} \tilde{G}^{s_b, s_{b+1}} \tilde{A}^{s_{b+2}} \tilde{B}^{s_{b+3}} \ldots \right) \begin{pmatrix} 0 \\ 1 \end{pmatrix}. \tag{A.56}$$

From the simple structure of the matrices, it is now easy to see that the only cases that give $c_{\vec{s}} \neq 0$ are the ones where the product of matrices in parentheses is a sequence of $\tilde{A}^o$, $\tilde{B}^0$, $\tilde{G}^{o,0}$, followed by a single matrix $\tilde{A}^+$ or $\tilde{B}^+$ and then by a sequence of $\tilde{A}^0$, $\tilde{B}^o$, $\tilde{G}^{0,o}$. Consider now a state $\vec{s}$ that satisfies this condition and let b^* be the index that corresponds to the $\tilde{A}^+$ or $\tilde{B}^+$ matrix. All the terms in $H_{non-int}$ annihilate $|\vec{s}\rangle$, except for the one with $b = b^*$: to prove this, it is sufficient to note that, for $b \in \Gamma_A$ if (i) $b < b^*$ then $s_{b-1} = o$ and hence $P^0_{b-1} |s_{b-1}\rangle = 0$, while if (ii) $b > b^*$ then $s_b = o$ and $[|00\rangle (\langle 10| + \langle 01|) + h.c.]_b |s_b\rangle = 0$; similarly, if (i) $b < b^*$ then $s_b = o$ and $[|00\rangle (\langle 10| + \langle 01|) + h.c.]_b |s_b\rangle = 0$, while if (ii) $b > b^*$ then $s_{b+1} = o$ and $P^0_{b+1} |s_{b+1}\rangle = 0$. The term of $H_{non-int}$ with $b = b^*$, on the other hand gives a non-zero term: if $b^* \in \Gamma_A$, then $s_{b^*-1} = 0$ and $s_{b^*} = +$, so $P^0_{b^*-1}[|00\rangle (\langle 10| + \langle 01|) + h.c.]_b |\vec{s}\rangle = \sqrt{2} |\vec{s}\rangle$, while if $b^* \in \Gamma_B$, then $s_{b^*+1} = 0$ and $s_{b^*} = +$, so $[|00\rangle (\langle 10| + \langle 01|) + h.c.]_b P^0_{b^*+1} |\vec{s}\rangle = \sqrt{2} |\vec{s}\rangle$. Therefore, we conclude that for each $\vec{s}$ such that $c_{\vec{s}} \neq 0$ $H_{non-int} |\vec{s}\rangle = \sqrt{2} |\vec{s}\rangle$, and using Eq. (A.55), we have $H_{non-int} |\psi_{\alpha=3}\rangle = \sqrt{2} \psi_{\alpha=3}$.

Appendix B

Constraint-induced delocalization

B.1 Extracting the disorder strengths $W^*(L)$ and $W_T(L)$

The average gap ratio $\overline{r}$ obtained for disordered PXP model with the constraint radius $\alpha = 2$ is shown in Fig. B.1a). A crossover between the ergodic regime at small disorder strengths W with $\overline{r} \approx \overline{r}_{GOE} \approx 0.53$ and the MBL regime at a large disorder with $\overline{r} \approx \overline{r}_{PS} \approx 0.39$ is clearly visible.

To extract the disorder strength $W_T(L)$ we find a crossing point of the $\overline{r}(W)$ curve for a given system size L with a constant $\overline{r} = \overline{r}_{GOE} - p$, as shown in Fig. B.1b). We take $p = 0.01$ and we have verified that setting $p \in (0.005, 0.02)$ does not change the quantitative behavior of $W_T(L)$ curves reported in the main text. We note that the value of parameter p is chosen in such a way that the average gap shows a "small deviation" from the GOE value at W_T. When the value of p is larger, e.g. $p \in (0.03, 0.05)$ (data not shown), the small L behavior of $W_T(L)$ is affected, however, the coefficient a describing the asymptotic linear growth $W_T(L) = aL + b + c/L + d/L^2$ remains the same within error bars.

The disorder strength $W^*(L)$ is obtained as a crossing point of $\overline{r}(W)$ curves for system sizes L_1, L_2 such that $L = (L_1 + L_2)/2$. Fig. B.1c) illustrates the extraction of $W^*(L = 26) = 6.00(4)$ for disordered PXP model with $\alpha = 2$. For $W = 6.2 > W^*(L = 26)$, we observe that the average gap ratio $\overline{r}$ decreases down to $\overline{r}_{PS}$ with increase of L when $L < 26$. At those system sizes the system is in the MBL regime for $W > W^*(L = 26)$. However, at sufficiently large L this is no longer the case and the system enters the "critical regime", as the comparison of $\overline{r}$ for $L = 28$ and $L = 32$ at $W = 6.2$ shows.

Due to a large variation in the scaling of Hilbert space dimension with system size L for various α, we proceed as follows when choosing L_1 and L_2 in the process of determination $W^*(L)$:

- for models with $\alpha \leq 2$, we choose $2 \leq |L_1 - L_2| \leq 4$. As the minimal difference between L_1 and L_2 we take 2, because the $\overline{r}(W)$ curves for $|L_1 - L_2| = 1$ lie very closely to each other which prevents us from an accurate determination of the crossing point. Disorder strength $W^*(L)$ is supposed to reflect the properties of the system at length scale L. To that end the values of L_1 and L_2 must be possibly close to L, hence we use $|L_1 - L_2| \leq 4$. The uncertainty of the length scale L at which $W^*(L)$ increases for larger values of $|L_1 - L_2|$. While this could be taken into account by adding an error bar on the value of L, we opt for choosing possibly small value of $|L_1 - L_2|$ for each model considered.

- for models with $\alpha > 2$, we choose $4 \leq |L_1 - L_2| \leq 2(2 + \alpha)$. Such a value of $|L_1 - L_2|$ is a result of balancing the two trends: we want $|L_1 - L_2|$ to be possibly small (so that

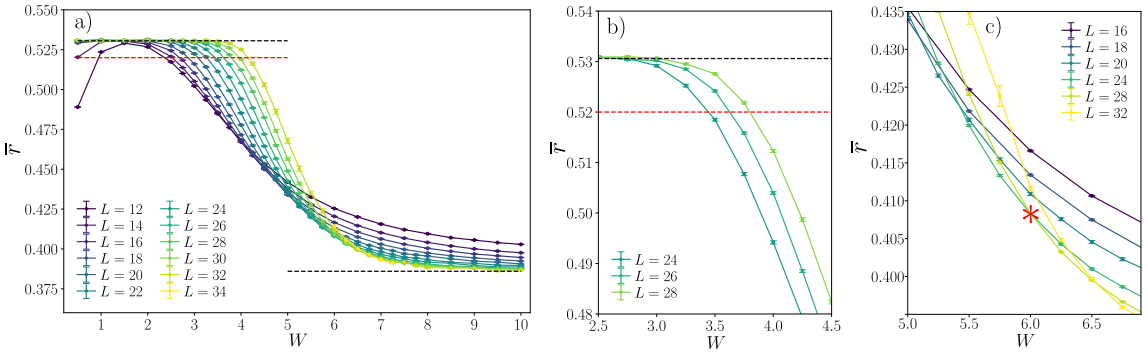

Figure B.1: Determination of disorder strengths $W_T(L)$ and $W^*(L)$. a) The average gap ratio at the middle of the spectrum for disordered PXP model with constraint radius $\alpha = 2$; b) $W_T(L)$ is found as a disorder strength W for which $\overline{r}(W) = \overline{r}_{GOE} - p \approx 0.52$ (denoted by the red line); c) The crossing point (denoted by $*$) of the gap ratio vs disorder strength $r(W)$ curves for $L = 24$ and $L = 28$ determines $W^*(L = 26) = 6.00(4)$.

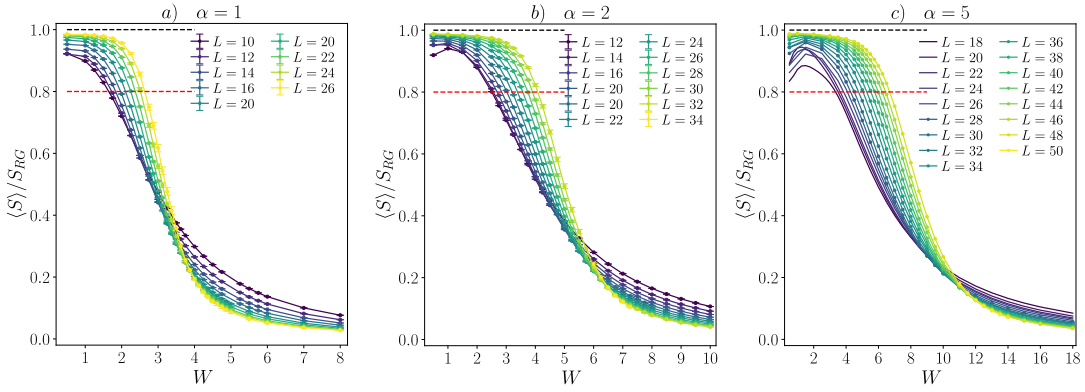

Figure B.2: The average entanglement entropy $\langle S \rangle$ of eigenstates at the middle of the spectrum of disordered PXP models divided by the entanglement entropy of random Gaussian states S_{RG} as a function of disorder strength W for various system sizes L and radius of constraint α.

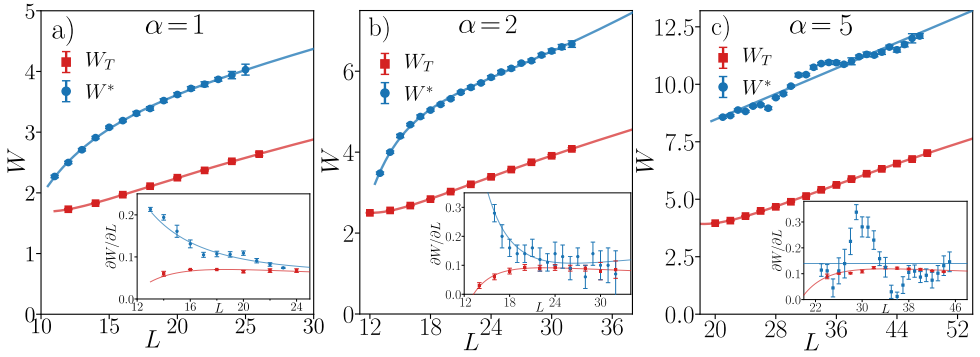

Figure B.3: The ergodic-MBL crossover in disordered PXP models. Disorder strengths $W_T(L)$ and $W^*(L)$ are obtained from analysis of the rescaled average entanglement entropy of eigenstates and plotted as function of the systems size L. Solid lines denote fits of the form $W(L) = aL + b + c/L + d/L^2$. The insets show derivatives of data with respect to L.

L_1 and L_2 are close to L), but not too small because then the determination of the crossing point is impeded. In the case of disordered PXP models: for $\alpha = 5$ we use $|L_1 - L_2| = 4, 6, 8$; for $\alpha = 7$ we use $L_1 - L_2| = 6$; for $\alpha = 10$ we use $|L_1 - L_2| = 8$. For the constrained models with $U(1)$ symmetry we use $|L_1 - L_2| = (2 + \alpha)$ and $|L_1 - L_2| = 2(2 + \alpha)$.

B.2 Analysis of the crossover in the average bipartite entanglement entropy of eigenstates

In a similar way one can analyze the crossover between the ergodic and MBL regimes using the average bipartite entanglement entropy of eigenstates $\langle S \rangle$. The average is performed over $\min\{\mathcal{N}_\alpha/20, 1000\}$ eigenstates in the middle of the spectrum and over all disorder realizations. Subsequently, the obtained values of the average entanglement entropy $\langle S \rangle$ are divided by the entanglement entropy of random Gaussian states S_{RG} for the constrained model of radius α. The value of S_{RG} is calculated numerically. The resulting rescaled entanglement entropy $\langle S \rangle / S_{RG}$ is expected to be close to 1 in the ergodic phase and to follow a $1/L$ scaling at large disorder strengths when the entanglement of eigenstates follows an area-law. This is indeed observed, as we show in Fig. B.2.

The disorder strength $W_T(L)$ is extracted from the rescaled entanglement entropy data at the point at which $\langle S \rangle / S_{RG} = 0.8$ (other values in the interval $(0.7, 0.95)$ give similar results). The rescaled entanglement entropy $\langle S \rangle / S_{RG}$ can be used to determine crossing points resulting in $W^*(L)$, analogously as in the case of the average gap ratio. The disorder strengths $W_T(L)$ and $W^*(L)$ obtained in such an analysis of the rescaled entanglement entropy data are shown in Fig. B.3. The linear drift of the whole ergodic-MBL crossover with increasing system size L to larger disorder strengths is clearly observed. This supports the conclusions obtained from the analysis of the average gap ratio in the main text.

B.3 Localization of wave function in the Fock space

In the main text we have shown that $W_T(L)$ as well as $W^*(L)$ increase linearly with L at sufficiently large system size: $W_T(L) \sim w_T L$ and $W^*(L) \sim w^* L$. We have also established that $w_T \leq w^*$.

The recent work [137] examines the behavior of fractal dimensions D_q for random quantum Ising model, finding that the wave function of the system is localized in the Fock space for $W_{AT}(L) = w'L$. Anderson localization of wave function is much stronger ergodicity breaking than MBL (which is defined on the level of local observables). Nevertheless, this results is consistent with our predictions provided that $w' > w^*$.

B.4 The radius of Fock space

In this section we provide arguments supporting the expectation that the kinetic term is getting more effective with increasing constraint radius α for the PXP models and that it is not the case for the constraints models with $U(1)$ symmetry.

Let us take an arbitrary eigenstate $|n\rangle$ of S_i^z operators which can be mapped to a certain Fock state of spinless fermions. Such a state is an eigenstate of the Hamiltonian of the constrained model in the large disorder ($W \to \infty$) limit. We consider now the following procedure. Acting with Hamiltonian H on $|n\rangle$, we obtain a state $H|n\rangle$ which is a non-trivial superposition of Fock states. The minimal integer R for which $H^R|n\rangle$ has a non-zero overlap with *all* Fock states in the Hilbert space, averaged over initial states, defines a *Fock*

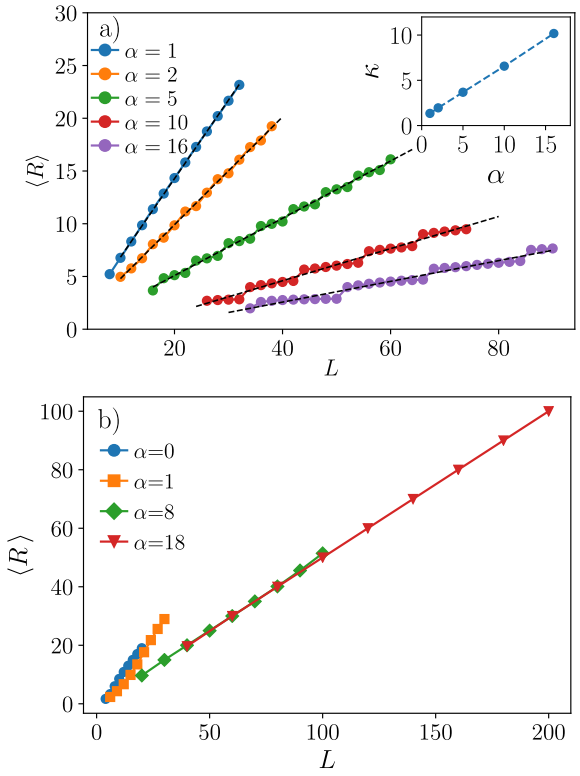

Figure B.4: The average radius of the Fock space $\langle R \rangle$ as function of the system size L for varying constrain radius α. For PXP models – panel a) – $\langle R \rangle \approx \frac{1}{\kappa} L$ where κ is increasing linearly with α (see the inset); for the constrained models with $U(1)$ symmetry, $\langle R \rangle \approx \frac{1}{2} L$ for large constraint radius α.

space radius $\langle R \rangle$. The bigger the value of $\langle R \rangle$, the larger is the number of actions of the kinetic term of Hamiltonian H needed to reach an arbitrary Fock state. Hence, it may be expected that the localization will be favored in systems where $\langle R \rangle$ increases rapidly with the system size L. And conversely, slow growth of $\langle R \rangle$ with system size L means that only few actions of H is needed in order to reach an arbitrary state from a given initial state, hence the Fock states are much more prone to delocalization over the whole Hilbert space.

The values of the average Fock space radius $\langle R \rangle$ for PXP models shown in Fig. B.4 a), demonstrate the approximately linear dependence $\langle R \rangle = \frac{1}{\kappa} L + const$ for all values of constraint radius α. The coefficient κ is linearly increasing with the constrain radius as the inset in Fig. B.4 a) shows. This implies that the disordered PXP models are indeed more prone to delocalization as the constraint radius is increased – this is reflected both in the values of W^* growing with α as well as in the well pronounced linear behavior of the $W^*(L)$ curves at large L. In fact, the oscillations on top of the linear trend in $W^*(L)$ for disordered PXP models with $\alpha = 5, 7, 10$ match the stair-like structure that appears in $\langle R \rangle (L)$ dependence.

The average Fock space radius $\langle R \rangle$ for the constrained models with $U(1)$ symmetry is shown in Fig. B.4 b) confirming that $\langle R \rangle \approx \frac{1}{2} L$ at large α. This makes the constrained models with $U(1)$ symmetry much more prone to localization in comparison to disordered PXP models. However, the interplay of disorder and constraints, described in the main text, assures the ergodicity of the constrained models with $U(1)$ symmetry at sufficiently large system size.

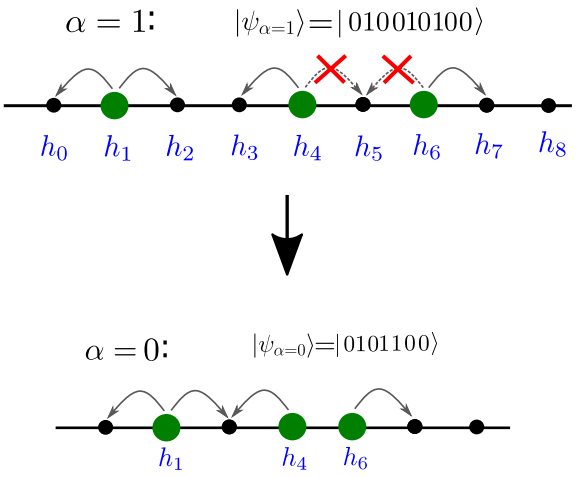

Figure B.5: Mapping between constrained model (constraint radius $\alpha = 1$) with $U(1)$ symmetry (top) and an unconstrained model.

B.5 Forward approximation for disordered PXP models

The forward approximation (FWA) provides a perturbative expression for the coefficients $\psi(n)$ of eigenstates in the basis of Fock states $|n\rangle$ [201]. The coefficient is equal (to the lowest order in $1/W$) to

$$\psi(n_2)_r = \sum_{p \in spaths(n_1,n_2)} \prod_{n \in p} \frac{1}{E_{n_1} - E_n}, \tag{B.1}$$

where $spaths(n_1, n_2)$ are the shortest paths connecting the Fock States $|n_1\rangle$, $|n_2\rangle$, it was assumed that $\psi(n_2) \to \delta_{n,n_2}$ as $W \to \infty$ and r is the length of the path between states $|n_1\rangle$, $|n_2\rangle$. FWA allows to qualitatively capture the MBL in disordered XXZ spin chain [201]. The localization occurs when the amplitude of the wavefunction decreases exponentially with distance from the center of the localization of a given eigenstate. Hence, we study the average growth rate:

$$Z_R = \frac{\log |\psi_R^2|}{2R}, \tag{B.2}$$

where the wavefunction ψ_R is calculated for the longest available paths with the average length of the Hilbert space radius R. This quantity, averaged over the centers of localization n_1 and over disorder realizations gives rise to $\langle Z_R \rangle$ shown in Fig. B.6 a), b) for disordered PXP models. FWA clearly captures the ergodic regime at small disorder strength W for which $\langle Z_R \rangle$ increases with system size L. The localized regime for which $\langle Z_R \rangle$ decreases with L is also visible. The crossing point of $\langle Z_R \rangle (W)$ curves for different L occurs at $W^*_{FWA} \approx 2.7$ both for $\alpha = 1$ and $\alpha = 10$ (and is, within the error bar, the same for all all $\alpha \in [1, 10]$). Fixing the system size to $L = 34$ and varying the radius of constraint α, we see that $\langle Z_R \rangle$ collapse upon rescaling $\langle Z_R \rangle \to \langle Z_R \rangle / f_{FWA}$ where the factor f_{FWA} depends linearly on the system size as shown in Fig. B.6.

The results of FWA, predicting a localization transition at the disorder strength W^*_{FWA} independent of the constraint radius α, are in a striking mismatch with the exact diagonalization data discussed in the main text which show that the crossover to localized regime occurs at a disorder strength increasing with α. Hence, the non-perturbative (beyond the FWA) effects destabilize the localized regime. Moreover, the impact of non-perturbative effects is getting stronger with increasing α since the mismatch between W^*_{FWA} and $W^*(L)$

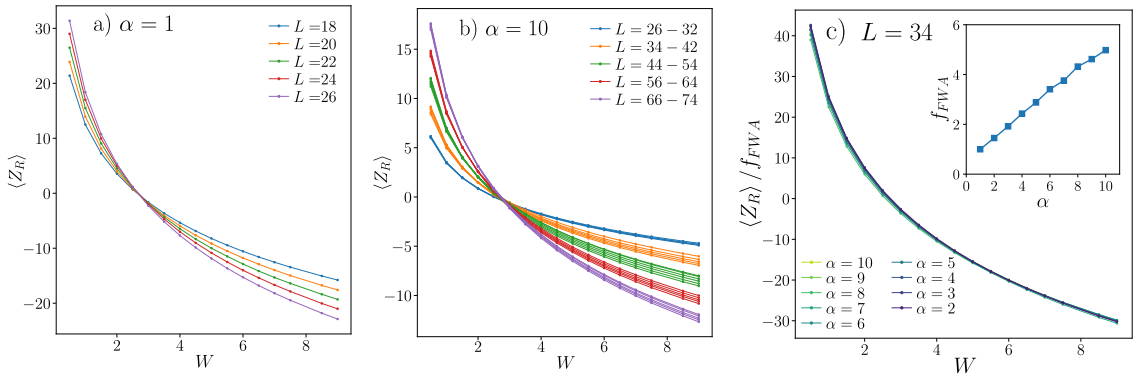

Figure B.6: Forward approximation for disordered PXP models. Panels *a*), *b*): the logarithm FWA amplitude $\langle Z_R \rangle$ (see text) for constraint radius $\alpha = 1, 10$. Panel *c*) the collapse of $\langle Z_R \rangle (W)$ for fixed system size $L = 34$ and varying radius of constraint $\alpha \in [1, 10]$ is obtained after a rescaling $\langle Z_R \rangle \to \langle Z_R \rangle / f_{FWA}$. The factor f_{FWA} is shown in the inset in panel c).

from exact diagonalization data increases with α. Such a scenario can be anticipated from the FWA results: the values of $\langle Z_R \rangle$ in the localized regime are orders of magnitude smaller for $\alpha = 10$ than for $\alpha = 1$. Hence, it seems plausible that the non-perturbative effects will be more apparent in systems with larger α.

The crossover between ergodic and MBL regimes in disordered PXP models was interpreted in favour of a stable MBL phase in [118]. The main argument of [118] is that the projection operators P_i^α commute with the disorder term $\sum_i h_i S_i^z$ and hence do not introduce new terms in expansion of a Fock state $|n\rangle$ in the $1/W$ perturbation series, in addition to *removing* some amplitudes which are instead allowed in their absence, for any fixed L. The argument was limited to lowest orders in perturbation theory and in this sense it cannot be considered rigorous. In fact, while it is true that for any given system size L the amplitudes are reduced by the presence of the constraints, it seems from our results that this simply moves the amplitudes growth up to some larger length scale (increasing with α), and that going to sufficiently larger L one recovers the lost amplitudes and then some more. We believe this ultimately leads to delocalization.

It is also true that one cannot, prima facie, discard the hypothesis that, for any given α, $W^*(\alpha, L) \to W_c^*(\alpha) < \infty$; But by comparing systems with different L's and α's we believe our data and interpretation do provide a coherent picture of delocalization in these constrained models. The impact of effects which occur beyond the FWA is apparent from the mismatch between FWA and exact diagonalization result. We believe that it is the strong non-perturbative effects, which cannot be captured within perturbation theory, that underlie the delocalization of the considered constrained models.

B.6 The mapping between constrained and unconstrained models

The mapping between constrained and unconstrained models is schematically shown in Fig. B.5. State $|\psi_{\alpha=1}\rangle = |010010100\rangle$ is a state of the constrained model with constraint radius $\alpha = 1$. Due to the presence of constraints, the particles on sites $i = 4$ ($i = 6$), where numeration starts from $i = 0$, cannot hop to the right (left). To map a state of model with constraint radius α and size L to a state of unconstrained model, each particle is joined

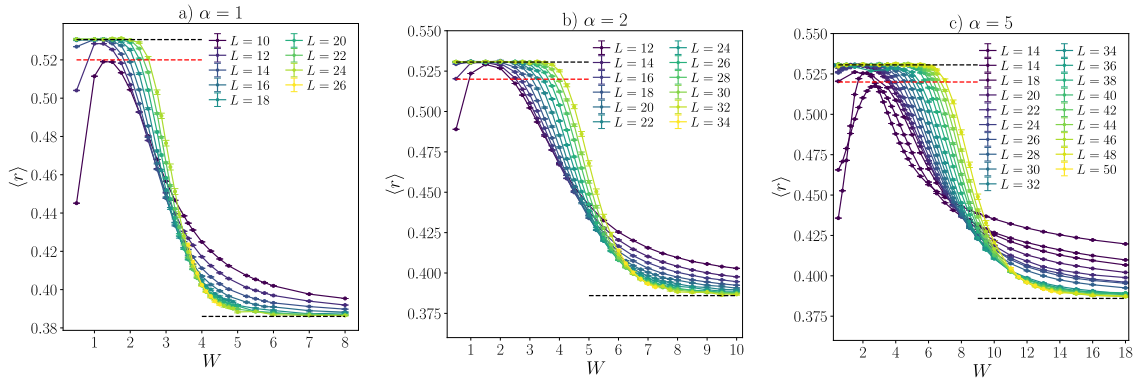

Figure B.7: The average gap ratio at the middle of the spectrum of disordered PXP models a function of disorder strength W for various system sizes L and radius of constraint α.

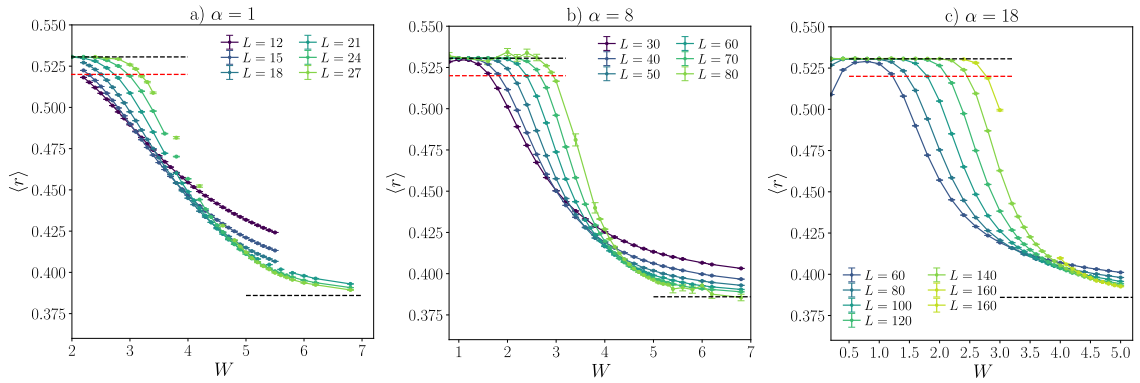

Figure B.8: The average gap ratio at the middle of the spectrum of disordered constrained models with $U(1)$ symmetry (Hamiltonian (2) in the main text) a function of disorder strength W for various system sizes L and radius of constraint α.

with α sites to its right (in some sense each particle acquires a $1+\alpha$ site radius). To assure that it can be done for each particle α sites are added at the right end of the chain, so that the chain is of size $L + \alpha$. Subsequently, each 'particle' of radius $1 + \alpha$ is replaced by an ordinary spinless fermion. The resulting chain size is $L + \alpha - N\alpha$. The procedure can be performed for each Fock state of the constrained model establishing a 1:1 mapping between a constrained model with N particles on L sites with constraint radius α (and open boundary conditions) to a model of N spinless fermions on $L - \alpha(N - 1)$ sites.

B.7 Average gap ratio for constrained models

Data for average gap ratio for disordered PXP models and for constrained models with $U(1)$ symmetry, used to extract the disorder strengths $W^*(L)$ and $W_T(L)$ is shown in Fig. B.7 and Fig. B.8.

Bibliography

[1] C. Gogolin and J. Eisert, *Equilibration, thermalisation, and the emergence of statistical mechanics in closed quantum systems*, *Reports on Progress in Physics* **79** (2016) 056001.

[2] L. D'Alessio, Y. Kafri, A. Polkovnikov and M. Rigol, *From quantum chaos and eigenstate thermalization to statistical mechanics and thermodynamics*, *Advances in Physics* **65** (2016) 239–362.

[3] T. Kinoshita, T. Wenger and D.S. Weiss, *A quantum newton's cradle*, *Nature* **440** (2006) 900.

[4] M. Schreiber, S.S. Hodgman, P. Bordia, H.P. Lüschen, M.H. Fischer, R. Vosk et al., *Observation of many-body localization of interacting fermions in a quasirandom optical lattice*, *Science* **349** (2015) 842.

[5] J. Smith, A. Lee, P. Richerme, B. Neyenhuis, P.W. Hess, P. Hauke et al., *Many-body localization in a quantum simulator with programmable random disorder*, *Nature Physics* **12** (2016) 907.

[6] T. Langen, R. Geiger and J. Schmiedmayer, *Ultracold atoms out of equilibrium*, *Annual Review of Condensed Matter Physics* **6** (2015) 201–217.

[7] R.P. Feynman, *Simulating physics with computers*, *International Journal of Theoretical Physics* **21** (1982) 467–488.

[8] I. Bloch, J. Dalibard and S. Nascimbène, *Quantum simulations with ultracold quantum gases*, *Nature Physics* **8** (2012) 267.

[9] S. Trotzky, Y.-A. Chen, A. Flesch, I.P. McCulloch, U. Schollwöck, J. Eisert et al., *Probing the relaxation towards equilibrium in an isolated strongly correlated one-dimensional bose gas*, *Nature Physics* **8** (2012) 325–330.

[10] K. Van Houcke, F. Werner, E. Kozik, N. Prokof'ev, B. Svistunov, M.J.H. Ku et al., *Feynman diagrams versus fermi-gas feynman emulator*, *Nature Physics* **8** (2012) 366–370.

[11] P. Schauß, M. Cheneau, M. Endres, T. Fukuhara, S. Hild, A. Omran et al., *Observation of spatially ordered structures in a two-dimensional rydberg gas*, *Nature* **491** (2012) 87.

[12] A. Browaeys and T. Lahaye, *Many-body physics with individually controlled Rydberg atoms*, *Nature Physics* **16** (2020) 132 [2002.07413].

[13] J.W. Britton, B.C. Sawyer, A.C. Keith, C.-C.J. Wang, J.K. Freericks, H. Uys et al., *Engineered two-dimensional ising interactions in a trapped-ion quantum simulator with hundreds of spins*, *Nature* **484** (2012) 489.

[14] C. Monroe, W. Campbell, L.-M. Duan, Z.-X. Gong, A. Gorshkov, P. Hess et al., *Programmable quantum simulations of spin systems with trapped ions*, *Reviews of Modern Physics* **93** (2021) .

[15] H. Bernien, S. Schwartz, A. Keesling, H. Levine, A. Omran, H. Pichler et al., *Probing many-body dynamics on a 51-atom quantum simulator*, *Nature* **551** (2017) 579–584.

[16] C.J. Turner, A.A. Michailidis, D.A. Abanin, M. Serbyn and Z. Papić, *Weak ergodicity breaking from quantum many-body scars*, *Nature Physics* **14** (2018) 745–749.

[17] F.M. Surace, M. Votto, E.G. Lazo, A. Silva, M. Dalmonte and G. Giudici, *Exact many-body scars and their stability in constrained quantum chains*, *Physical Review B* **103** (2021) [2011.08218].

[18] P. Sierant, E. Gonzalez Lazo, M. Dalmonte, A. Scardicchio and J. Zakrzewski, *Constraints induced delocalization*, *Accepted in Phys. Rev. Lett.* (2021) [2103.14020].

[19] E. Gonzalez Lazo, M. Heyl, M. Dalmonte and A. Angelone, *Finite-temperature critical behavior of long-range quantum Ising models*, *Submitted to SciPost Phys.* (2021) [2104.15070].

[20] E. Ott, *Chaos in Dynamical Systems*, Cambridge University Press, 2 ed. (2002), 10.1017/CBO9780511803260.

[21] A.M. Kaufman, M.E. Tai, A. Lukin, M. Rispoli, R. Schittko, P.M. Preiss et al., *Quantum thermalization through entanglement in an isolated many-body system*, *Science* **353** (2016) 794.

[22] M. Gring, M. Kuhnert, T. Langen, T. Kitagawa, B. Rauer, M. Schreitl et al., *Relaxation and prethermalization in an isolated quantum system*, *Science* **337** (2012) 1318.

[23] J. Kemp, N.Y. Yao, C.R. Laumann and P. Fendley, *Long coherence times for edge spins*, *Journal of Statistical Mechanics: Theory and Experiment* **2017** (2017) 063105.

[24] D.V. Else, P. Fendley, J. Kemp and C. Nayak, *Prethermal strong zero modes and topological qubits*, *Phys. Rev. X* **7** (2017) 041062.

[25] D.A. Huse, R. Nandkishore, V. Oganesyan, A. Pal and S.L. Sondhi, *Localization-protected quantum order*, *Phys. Rev. B* **88** (2013) 014206.

[26] Y. Bahri, R. Vosk, E. Altman and A. Vishwanath, *Localization and topology protected quantum coherence at the edge of hot matter*, *Nature Communications* **6** (2015) 7341.

[27] C.J. Turner, A.A. Michailidis, D.A. Abanin, M. Serbyn and Z. Papić, *Weak ergodicity breaking from quantum many-body scars*, *Nat. Phys.* **14** (2018) 745.

[28] J.M. Deutsch, *Quantum statistical mechanics in a closed system*, *Physical Review A* **43** (1991) 2046–2049.

[29] M. Srednicki, *Chaos and quantum thermalization*, *Physical Review E* **50** (1994) 888–901.

[30] M. Srednicki, *The approach to thermal equilibrium in quantized chaotic systems*, *Journal of Physics A: Mathematical and General* **32** (1999) 1163.

[31] M. Rigol, V. Dunjko and M. Olshanii, *Thermalization and its mechanism for generic isolated quantum systems*, *Nature* **452** (2008) 854–858.

[32] E. Khatami, G. Pupillo, M. Srednicki and M. Rigol, *Fluctuation-dissipation theorem in an isolated system of quantum dipolar bosons after a quench*, *Physical Review Letters* **111** (2013) .

[33] J.M. Deutsch, *Thermodynamic entropy of a many-body energy eigenstate*, *New Journal of Physics* **12** (2010) 075021.

[34] M. Rigol, *Breakdown of thermalization in finite one-dimensional systems*, *Physical Review Letters* **103** (2009) .

[35] S. Sorg, L. Vidmar, L. Pollet and F. Heidrich-Meisner, *Relaxation and thermalization in the one-dimensional bose-hubbard model: A case study for the interaction quantum quench from the atomic limit*, *Physical Review A* **90** (2014) .

[36] H. Kim, T.N. Ikeda and D.A. Huse, *Testing whether all eigenstates obey the eigenstate thermalization hypothesis*, *Physical Review E* **90** (2014) .

[37] R. Steinigeweg, A. Khodja, H. Niemeyer, C. Gogolin and J. Gemmer, *Pushing the limits of the eigenstate thermalization hypothesis towards mesoscopic quantum systems*, *Physical Review Letters* **112** (2014) .

[38] S.D. Geraedts, R. Nandkishore and N. Regnault, *Many-body localization and thermalization: Insights from the entanglement spectrum*, *Physical Review B* **93** (2016) .

[39] P.W. Anderson, *Absence of diffusion in certain random lattices*, *Physical Review* **109** (1958) 1492–1505.

[40] E. Abrahams, *50 YEARS OF ANDERSON LOCALIZATION*, World Scientific Publishing Co. Pte. Ltd. (2010), 10.1142/9789814299084.

[41] D. Basko, I. Aleiner and B. Altshuler, *Metal–insulator transition in a weakly interacting many-electron system with localized single-particle states*, *Annals of Physics* **321** (2006) 1126–1205.

[42] V. Oganesyan and D.A. Huse, *Localization of interacting fermions at high temperature*, *Physical Review B* **75** (2007) .

[43] M. Žnidarič, T. Prosen and P. Prelovšek, *Many-body localization in the heisenberg xxz magnet in a random field*, *Physical Review B* **77** (2008) .

[44] A. Pal and D.A. Huse, *Many-body localization phase transition*, *Physical Review B* **82** (2010) .

[45] C. Kollath, G. Roux, G. Biroli and A.M. Läuchli, *Statistical properties of the spectrum of the extended bose–hubbard model*, *Journal of Statistical Mechanics: Theory and Experiment* **2010** (2010) P08011.

[46] M. Rigol and L.F. Santos, *Quantum chaos and thermalization in gapped systems*, *Physical Review A* **82** (2010) .

[47] M. Collura, H. Aufderheide, G. Roux and D. Karevski, *Entangling many-body bound states with propagative modes in bose-hubbard systems*, *Physical Review A* **86** (2012) .

[48] V. Oganesyan, A. Pal and D.A. Huse, *Energy transport in disordered classical spin chains*, *Physical Review B* **80** (2009) .

[49] E. Cuevas, M. Feigel'man, L. Ioffe and M. Mezard, *Level statistics of disordered spin-1/2 systems and materials with localized cooper pairs*, *Nature Communications* **3** (2012) .

[50] B. Bauer and C. Nayak, *Area laws in a many-body localized state and its implications for topological order*, *Journal of Statistical Mechanics: Theory and Experiment* **2013** (2013) P09005.

[51] M. Serbyn, Z. Papić and D.A. Abanin, *Local conservation laws and the structure of the many-body localized states*, *Physical Review Letters* **111** (2013) .

[52] D.A. Huse, R. Nandkishore and V. Oganesyan, *Phenomenology of fully many-body-localized systems*, *Physical Review B* **90** (2014) .

[53] V. Ros, M. Müller and A. Scardicchio, *Integrals of motion in the many-body localized phase*, *Nuclear Physics B* **891** (2015) 420–465.

[54] D.A. Abanin, E. Altman, I. Bloch and M. Serbyn, *Colloquium : Many-body localization, thermalization, and entanglement*, *Reviews of Modern Physics* **91** (2019) .

[55] C.J. Turner, A.A. Michailidis, D.A. Abanin, M. Serbyn and Z. Papić, *Quantum scarred eigenstates in a rydberg atom chain: Entanglement, breakdown of thermalization, and stability to perturbations*, *Physical Review B* **98** (2018) .

[56] E.J. Heller, *Bound-state eigenfunctions of classically chaotic hamiltonian systems: Scars of periodic orbits*, *Physical Review Letters* **53** (1984) 1515–1518.

[57] I. Lesanovsky and H. Katsura, *Interacting fibonacci anyons in a rydberg gas*, *Phys. Rev. A* **86** (2012) 041601.

[58] D. Barredo, V. Lienhard, S. de Léséleuc, T. Lahaye and A. Browaeys, *Synthetic three-dimensional atomic structures assembled atom by atom*, *Nature* **561** (2018) 79.

[59] J. Zeiher, J.-y. Choi, A. Rubio-Abadal, T. Pohl, R. van Bijnen, I. Bloch et al., *Coherent many-body spin dynamics in a long-range interacting ising chain*, *Phys. Rev. X* **7** (2017) 041063.

[60] S. Moudgalya, S. Rachel, B.A. Bernevig and N. Regnault, *Exact excited states of nonintegrable models*, *Physical Review B* **98** (2018) .

[61] C.J. Turner, A.A. Michailidis, D.A. Abanin, M. Serbyn and Z. Papić, *Quantum scarred eigenstates in a Rydberg atom chain: Entanglement, breakdown of thermalization, and stability to perturbations*, *Phys. Rev. B* **94** (2018) 155134.

[62] V. Khemani, C.R. Laumann and A. Chandran, *Signatures of integrability in the dynamics of Rydberg-blockaded chains*, *Phys. Rev. B* **99** (2019) 161101.

[63] C.-J. Lin and O.I. Motrunich, *Exact quantum many-body scar states in the rydberg-blockaded atom chain*, *Phys. Rev. Lett.* **122** (2019) 173401.

[64] C.-J. Lin, A. Chandran and O.I. Motrunich, *Slow thermalization of exact quantum many-body scar states under perturbations*, *Phys. Rev. Research* **2** (2020) 033044.

[65] P. Sierant, A. Maksymov, M. Kuś and J. Zakrzewski, *Fidelity susceptibility in gaussian random ensembles*, *Phys. Rev. E* **99** (2019) 050102.

[66] A. Maksymov, P. Sierant and J. Zakrzewski, *Energy level dynamics across the many-body localization transition*, *Phys. Rev. B* **99** (2019) 224202.

[67] D. Sels and A. Polkovnikov, *Dynamical obstruction to localization in a disordered spin chain*, `2009.04501`.

[68] S. Choi, C.J. Turner, H. Pichler, W.W. Ho, A.A. Michailidis, Z. Papić et al., *Emergent su(2) dynamics and perfect quantum many-body scars*, *Phys. Rev. Lett.* **122** (2019) 220603.

[69] M. Pandey, P.W. Claeys, D.K. Campbell, A. Polkovnikov and D. Sels, *Adiabatic eigenstate deformations as a sensitive probe for quantum chaos*, *Phys. Rev. X* **10** (2020) 041017.

[70] M. Schecter and T. Iadecola, *Many-body spectral reflection symmetry and protected infinite-temperature degeneracy*, *Physical Review B* **98** (2018) 35139 [`1801.03101`].

[71] W.-L. You, Y.-W. Li and S.-J. Gu, *Fidelity, dynamic structure factor, and susceptibility in critical phenomena*, *Phys. Rev. E* **76** (2007) 022101.

[72] S. Moudgalya, S. Rachel, B.A. Bernevig and N. Regnault, *Exact excited states of nonintegrable models*, *Phys. Rev. B* **98** (2018) 235155.

[73] S. Moudgalya, N. Regnault and B.A. Bernevig, *Entanglement of exact excited states of Affleck-Kennedy-Lieb-Tasaki models: Exact results, many-body scars, and violation of the strong eigenstate thermalization hypothesis*, *Phys. Rev. B* **98** (2018) 235156.

[74] D.K. Mark, C.-J. Lin and O.I. Motrunich, *Exact eigenstates in the lesanovsky model, proximity to integrability and the pxp model, and approximate scar states*, *Phys. Rev. B* **101** (2020) 094308.

[75] M. Schecter and T. Iadecola, *Weak ergodicity breaking and quantum many-body scars in spin-1 xy magnets*, *Phys. Rev. Lett.* **123** (2019) 147201.

[76] K. Bull, I. Martin and Z. Papić, *Systematic construction of scarred many-body dynamics in 1d lattice models*, *Phys. Rev. Lett.* **123** (2019) 030601.

[77] S. Ok, K. Choo, C. Mudry, C. Castelnovo, C. Chamon and T. Neupert, *Topological many-body scar states in dimensions one, two, and three*, *Phys. Rev. Research* **1** (2019) 033144.

[78] A. Hudomal, I. Vasić, N. Regnault and Z. Papić, *Quantum scars of bosons with correlated hopping*, *Communications Physics* **3** (2020) .

[79] N. Shibata, N. Yoshioka and H. Katsura, *Onsager's scars in disordered spin chains*, *Phys. Rev. Lett.* **124** (2020) 180604.

[80] S. Chattopadhyay, H. Pichler, M.D. Lukin and W.W. Ho, *Quantum many-body scars from virtual entangled pairs*, *Phys. Rev. B* **101** (2020) 174308.

[81] S. Pai and M. Pretko, *Dynamical scar states in driven fracton systems*, *Phys. Rev. Lett.* **123** (2019) 136401.

[82] S. Moudgalya, B.A. Bernevig and N. Regnault, *Quantum Many-body Scars in a Landau Level on a Thin Torus*, `1906.05292`.

[83] F.M. Surace, P.P. Mazza, G. Giudici, A. Lerose, A. Gambassi and M. Dalmonte, *Lattice gauge theories and string dynamics in rydberg atom quantum simulators*, *Phys. Rev. X* **10** (2020) 021041.

[84] F.M. Surace, G. Giudici and M. Dalmonte, *Weak-ergodicity-breaking via lattice supersymmetry*, *Quantum* **4** (2020) 339.

[85] T. Iadecola and M. Schecter, *Quantum many-body scar states with emergent kinetic constraints and finite-entanglement revivals*, *Phys. Rev. B* **101** (2020) .

[86] D.K. Mark, C.-J. Lin and O.I. Motrunich, *Unified structure for exact towers of scar states in the affleck-kennedy-lieb-tasaki and other models*, *Phys. Rev. B* **101** (2020) 195131.

[87] H. Zhao, J. Vovrosh, F. Mintert and J. Knolle, *Quantum many-body scars in optical lattices*, *Phys. Rev. Lett.* **124** (2020) 160604.

[88] K. Lee, R. Melendrez, A. Pal and H.J. Changlani, *Exact three-colored quantum scars from geometric frustration*, *Phys. Rev. B* **101** (2020) 241111.

[89] C.-J. Lin, V. Calvera and T.H. Hsieh, *Quantum many-body scar states in two-dimensional rydberg atom arrays*, *Phys. Rev. B* **101** (2020) 220304.

[90] D. Perez-Garcia, F. Verstraete, J. Cirac and M. Wolf, *Peps as unique ground states of local hamiltonians*, *Quantum Information and Computation* **8** (2008) 650–663.

[91] J. Wurtz and A. Polkovnikov, *Emergent conservation laws and nonthermal states in the mixed-field ising model*, *Phys. Rev. B* **101** (2020) 195138.

[92] S. Sugiura, P.W. Claeys, A. Dymarsky and A. Polkovnikov, *Adiabatic landscape and optimal paths in ergodic systems*, *Physical Review Research* **3** (2021) .

[93] N. Macé, F. Alet and N. Laflorencie, *Multifractal scalings across the many-body localization transition*, *Phys. Rev. Lett.* **123** (2019) 180601.

[94] F. Pietracaprina, N. Macé, D.J. Luitz and F. Alet, *Shift-invert diagonalization of large many-body localizing spin chains*, *SciPost Phys.* **5** (2018) 45.

[95] P. Sierant, M. Lewenstein and J. Zakrzewski, *Polynomially filtered exact diagonalization approach to many-body localization*, *Phys. Rev. Lett.* **125** (2020) 156601.

[96] R. Van Beeumen, G.D. Kahanamoku-Meyer, N.Y. Yao and C. Yang, *A scalable matrix-free iterative eigensolver for studying many-body localization*, ACM, Jan, 2020, DOI.

[97] J. Šuntajs, J. Bonča, T. Prosen and L. Vidmar, *Quantum chaos challenges many-body localization*, *Physical Review E* **102** (2020) .

[98] P. Sierant, D. Delande and J. Zakrzewski, *Thouless time analysis of anderson and many-body localization transitions*, *Phys. Rev. Lett.* **124** (2020) 186601.

[99] D. Abanin, J. Bardarson, G. De Tomasi, S. Gopalakrishnan, V. Khemani, S. Parameswaran et al., *Distinguishing localization from chaos: Challenges in finite-size systems*, *Annals of Physics* **427** (2021) 168415.

[100] R.K. Panda, A. Scardicchio, M. Schulz, S.R. Taylor and M. Žnidarič, *Can we study the many-body localisation transition?*, *EPL (Europhysics Letters)* **128** (2020) 67003.

[101] M. Kiefer-Emmanouilidis, R. Unanyan, M. Fleischhauer and J. Sirker, *Evidence for unbounded growth of the number entropy in many-body localized phases*, *Phys. Rev. Lett.* **124** (2020) 243601.

[102] D.J. Luitz and Y.B. Lev, *Absence of slow particle transport in the many-body localized phase*, *Phys. Rev. B* **102** (2020) 100202.

[103] D. Sels and A. Polkovnikov, *Dynamical obstruction to localization in a disordered spin chain*, `2009.04501`.

[104] H.P. Lüschen, P. Bordia, S. Scherg, F. Alet, E. Altman, U. Schneider et al., *Observation of slow dynamics near the many-body localization transition in one-dimensional quasiperiodic systems*, *Phys. Rev. Lett.* **119** (2017) 260401.

[105] E. Guardado-Sanchez, B.M. Spar, P. Schauss, R. Belyansky, J.T. Young, P. Bienias et al., *Quench dynamics of a fermi gas with strong nonlocal interactions*, *Physical Review X* **11** (2021) .

[106] P. Scholl, M. Schuler, H.J. Williams, A.A. Eberharter, D. Barredo, K.-N. Schymik et al., *Quantum simulation of 2d antiferromagnets with hundreds of rydberg atoms*, *Nature* **595** (2021) 233–238.

[107] S. Ebadi, T.T. Wang, H. Levine, A. Keesling, G. Semeghini, A. Omran et al., *Quantum phases of matter on a 256-atom programmable quantum simulator*, *Nature* **595** (2021) 227–232.

[108] C.J. Turner, A.A. Michailidis, D.A. Abanin, M. Serbyn and Z. Papić, *Weak ergodicity breaking from quantum many-body scars*, *Nature Physics* **14** (2018) 745.

[109] C.-J. Lin and O.I. Motrunich, *Exact quantum many-body scar states in the rydberg-blockaded atom chain*, *Phys. Rev. Lett.* **122** (2019) 173401.

[110] W.W. Ho, S. Choi, H. Pichler and M.D. Lukin, *Periodic orbits, entanglement, and quantum many-body scars in constrained models: Matrix product state approach*, *Phys. Rev. Lett.* **122** (2019) 040603.

[111] V. Khemani, C.R. Laumann and A. Chandran, *Signatures of integrability in the dynamics of rydberg-blockaded chains*, *Physical Review B* **99** (2019) .

[112] J. Choi, H. Zhou, S. Choi, R. Landig, W.W. Ho, J. Isoya et al., *Probing quantum thermalization of a disordered dipolar spin ensemble with discrete time-crystalline order*, *Phys. Rev. Lett.* **122** (2019) 043603.

[113] W.W. Ho, S. Choi, H. Pichler and M.D. Lukin, *Periodic orbits, entanglement, and quantum many-body scars in constrained models: Matrix product state approach*, *Phys. Rev. Lett.* **122** (2019) 040603.

[114] T. Iadecola and M. Žnidarič, *Exact localized and ballistic eigenstates in disordered chaotic spin ladders and the fermi-hubbard model*, *Phys. Rev. Lett.* **123** (2019) 036403.

[115] M. Schecter and T. Iadecola, *Weak ergodicity breaking and quantum many-body scars in spin-1 xy magnets*, *Phys. Rev. Lett.* **123** (2019) 147201.

[116] F.M. Surace, P.P. Mazza, G. Giudici, A. Lerose, A. Gambassi and M. Dalmonte, *Lattice gauge theories and string dynamics in rydberg atom quantum simulators*, *Phys. Rev. X* **10** (2020) 021041.

[117] I. Mondragon-Shem, M.G. Vavilov and I. Martin, *The fate of quantum many-body scars in the presence of disorder*, 2010.10535.

[118] C. Chen, F. Burnell and A. Chandran, *How does a locally constrained quantum system localize?*, *Phys. Rev. Lett.* **121** (2018) 085701.

[119] H. Théveniaut, Z. Lan, G. Meyer and F. Alet, *Transition to a many-body localized regime in a two-dimensional disordered quantum dimer model*, *Phys. Rev. Research* **2** (2020) 033154.

[120] F. Pietracaprina and F. Alet, *Probing many-body localization in a disordered quantum dimer model on the honeycomb lattice*, *SciPost Physics* **10** (2021) .

[121] L. Herviou, J.H. Bardarson and N. Regnault, *Many-body localization in a fragmented hilbert space*, *Physical Review B* **103** (2021) .

[122] Y.Y. Atas, E. Bogomolny, O. Giraud and G. Roux, *Distribution of the ratio of consecutive level spacings in random matrix ensembles*, *Phys. Rev. Lett.* **110** (2013) 084101.

[123] L.F. Santos, G. Rigolin and C.O. Escobar, *Entanglement versus chaos in disordered spin chains*, *Phys. Rev. A* **69** (2004) 042304.

[124] T.C. Berkelbach and D.R. Reichman, *Conductivity of disordered quantum lattice models at infinite temperature: Many-body localization*, *Phys. Rev. B* **81** (2010) 224429.

[125] D.J. Luitz, N. Laflorencie and F. Alet, *Many-body localization edge in the random-field Heisenberg chain*, *Phys. Rev. B* **91** (2015) 081103.

[126] S. Bera, H. Schomerus, F. Heidrich-Meisner and J.H. Bardarson, *Many-body localization characterized from a one-particle perspective*, *Phys. Rev. Lett.* **115** (2015) 046603.

[127] T. Enss, F. Andraschko and J. Sirker, *Many-body localization in infinite chains*, *Phys. Rev. B* **95** (2017) 045121.

[128] L. Herviou, S. Bera and J.H. Bardarson, *Multiscale entanglement clusters at the many-body localization phase transition*, *Phys. Rev. B* **99** (2019) 134205.

[129] P. Sierant and J. Zakrzewski, *Model of level statistics for disordered interacting quantum many-body systems*, *Phys. Rev. B* **101** (2020) 104201.

[130] L.A. Colmenarez, P.A. McClarty, M. Haque and D.J. Luitz, *Statistics of correlation functions in the random heisenberg chain*, *SciPost Physics* **7** (2019) .

[131] T. Chanda, P. Sierant and J. Zakrzewski, *Many-body localization transition in large quantum spin chains: The mobility edge*, *Phys. Rev. Research* **2** (2020) 032045.

[132] J. Šuntajs, J. Bonča, T. Prosen and L. Vidmar, *Ergodicity breaking transition in finite disordered spin chains*, *Phys. Rev. B* **102** (2020) 064207.

[133] N. Laflorencie, G. Lemarié and N. Macé, *Chain breaking and kosterlitz-thouless scaling at the many-body localization transition in the random-field heisenberg spin chain*, *Physical Review Research* **2** (2020) .

[134] T. Devakul and R.R.P. Singh, *Early breakdown of area-law entanglement at the many-body delocalization transition*, *Phys. Rev. Lett.* **115** (2015) 187201.

[135] J. Gray, S. Bose and A. Bayat, *Many-body localization transition: Schmidt gap, entanglement length, and scaling*, *Phys. Rev. B* **97** (2018) 201105.

[136] E.V.H. Doggen, F. Schindler, K.S. Tikhonov, A.D. Mirlin, T. Neupert, D.G. Polyakov et al., *Many-body localization and delocalization in large quantum chains*, *Phys. Rev. B* **98** (2018) 174202.

[137] G. De Tomasi, I.M. Khaymovich, F. Pollmann and S. Warzel, *Rare thermal bubbles at the many-body localization transition from the fock space point of view*, *Physical Review B* **104** (2021) .

[138] G. De Tomasi, D. Hetterich, P. Sala and F. Pollmann, *Dynamics of strongly interacting systems: From fock-space fragmentation to many-body localization*, *Phys. Rev. B* **100** (2019) 214313.

[139] G. Pupillo, A. Micheli, M. Boninsegni, I. Lesanovsky and P. Zoller, *Strongly correlated gases of rydberg-dressed atoms: Quantum and classical dynamics*, *Physical Review Letters* **104** (2010) .

[140] J. Honer, H. Weimer, T. Pfau and H.P. Büchler, *Collective many-body interaction in rydberg dressed atoms*, *Phys. Rev. Lett.* **105** (2010) 160404.

[141] N. Henkel, R. Nath and T. Pohl, *Three-dimensional roton excitations and supersolid formation in rydberg-excited bose-einstein condensates*, *Phys. Rev. Lett.* **104** (2010) 195302.

[142] M. Mattioli, M. Dalmonte, W. Lechner and G. Pupillo, *Cluster luttinger liquids of rydberg-dressed atoms in optical lattices*, *Phys. Rev. Lett.* **111** (2013) 165302.

[143] M. Brenes, M. Dalmonte, M. Heyl and A. Scardicchio, *Many-body localization dynamics from gauge invariance*, *Phys. Rev. Lett.* **120** (2018) 030601.

[144] G. Giudici, F.M. Surace, J.E. Ebot, A. Scardicchio and M. Dalmonte, *Breakdown of ergodicity in disordered $u(1)$ lattice gauge theories*, *Phys. Rev. Research* **2** (2020) 032034.

[145] J.Z. Imbrie, *Diagonalization and many-body localization for a disordered quantum spin chain*, *Phys. Rev. Lett.* **117** (2016) 027201.

[146] J.Z. Imbrie, *On many-body localization for quantum spin chains*, *Journal of Statistical Physics* **163** (2016) 998.

[147] T. Dauxois, S. Ruffo, E. Arimondo and M. Wilkens, *Dynamics and thermodynamics of systems with long-range interactions: An introduction*, *Lecture Notes in Physics* (2002) 1–19.

[148] A. Campa, A. Giansanti, G. Morigi and F.S. Labini, *The study of the equilibrium and of the dynamical properties of long-range interacting systems*, *AIP Conference Proceedings* (2008) .

[149] G. Bertin, *Dynamics of Galaxies*, Cambridge University Press (2009), 10.1017/cbo9780511731990.

[150] R. Goldston and P. Rutherford, *Introduction to Plasma Physics*, Taylor amp; Francis (Nov, 1995), 10.1201/9781439822074.

[151] M. Born and K. Huang, *Dynamical Theory of Crystal Lattices*, Clarendon Oxford (1954).

[152] A. Campa, T. Dauxois, D. Fanelli and S. Ruffo, *Physics of Long-Range Interacting Systems*, Oxford University Press (Aug, 2014), 10.1093/acprof:oso/9780199581931.001.0001.

[153] R. Landig, L. Hruby, N. Dogra, M. Landini, R. Mottl, T. Donner et al., *Quantum phases from competing short- and long-range interactions in an optical lattice*, *Nature* **532** (2016) 476.

[154] A. Keesling, A. Omran, H. Levine, H. Bernien, H. Pichler, S. Choi et al., *Quantum Kibble-Zurek mechanism and critical dynamics on a programmable Rydberg simulator*, *Nature* **568** (2019) 207 [1809.05540].

[155] J. Zhang, G. Pagano, P.W. Hess, A. Kyprianidis, P. Becker, H. Kaplan et al., *Observation of a many-body dynamical phase transition with a 53-qubit quantum simulator*, *Nature* **551** (2017) 601 [1708.01044].

[156] P. Jurcevic, H. Shen, P. Hauke, C. Maier, T. Brydges, C. Hempel et al., *Direct Observation of Dynamical Quantum Phase Transitions in an Interacting Many-Body System*, *Physical Review Letters* **119** (2017) 080501 [1612.06902].

[157] J. Zhang, P.W. Hess, A. Kyprianidis, P. Becker, A. Lee, J. Smith et al., *Observation of a discrete time crystal*, *Nature* **543** (2017) 217.

[158] S. Choi, J. Choi, R. Landig, G. Kucsko, H. Zhou, J. Isoya et al., *Observation of discrete time-crystalline order in a disordered dipolar many-body system*, *Nature* **543** (2017) 221 [1610.08057].

[159] B. Neyenhuis, J. Zhang, P.W. Hess, J. Smith, A.C. Lee, P. Richerme et al., *Observation of prethermalization in long-range interacting spin chains*, *Science Advances* **3** (2017) e1700672 [1608.00681].

[160] K.R. Fratus and M. Srednicki, *Eigenstate Thermalization and Spontaneous Symmetry Breaking in the One-Dimensional Transverse-Field Ising Model with Power-Law Interactions*, *arXiv e-prints* (2016) arXiv:1611.03992 [1611.03992].

[161] A. Russomanno, M. Fava and M. Heyl, *Long-range Ising chains: eigenstate thermalization and symmetry breaking of excited states*, *arXiv e-prints* (2020) arXiv:2012.06505 [2012.06505].

[162] F.J. Dyson, *Existence of a phase-transition in a one-dimensional ising ferromagnet*, *Communications in Mathematical Physics* **12** (1969) 91–107.

[163] M.E. Fisher, S.-k. Ma and B.G. Nickel, *Critical exponents for long-range interactions*, *Physical Review Letters* **29** (1972) 917–920.

[164] J. Sak, *Recursion relations and fixed points for ferromagnets with long-range interactions*, *Physical Review B* **8** (1973) 281–285.

[165] N. Defenu, A. Trombettoni and S. Ruffo, *Criticality and phase diagram of quantum long-range o(n) models*, *Physical Review B* **96** (2017) .

[166] D.J. Thouless, *Long-range order in one-dimensional ising systems*, *Physical Review* **187** (1969) 732–733.

[167] P.W. Anderson, G. Yuval and D.R. Hamann, *Exact results in the kondo problem. ii. scaling theory, qualitatively correct solution, and some new results on one-dimensional classical statistical models*, *Physical Review B* **1** (1970) 4464–4473.

[168] J.L. Cardy, *One-dimensional models with 1/r2interactions*, *Journal of Physics A: Mathematical and General* **14** (1981) 1407–1415.

[169] J. Fröhlich and T. Spencer, *The phase transition in the one-dimensional ising model with 1/r 2 interaction energy*, *Communications in Mathematical Physics* **84** (1982) 87–101.

[170] E. Luijten and H. Meßingfeld, *Criticality in one dimension with inverse square-law potentials*, *Physical Review Letters* **86** (2001) 5305–5308.

[171] A. Dutta and J.K. Bhattacharjee, *Phase transitions in the quantum ising and rotor models with a long-range interaction*, *Physical Review B* **64** (2001) .

[172] S. Sachdev, *Quantum Phase Transitions*, Cambridge University Press, 2 edition ed. (2011).

[173] S. Humeniuk, *Thermal kosterlitz–thouless transitions in the 1/r 2 long-range ferromagnetic quantum ising chain revisited*, *Journal of Statistical Mechanics: Theory and Experiment* **2020** 063105.

[174] N. Metropolis, A.W. Rosenbluth, M.N. Rosenbluth, A.H. Teller and E. Teller, *Equation of state calculations by fast computing machines*, *The Journal of Chemical Physics* **21** (1953) 1087–1092.

[175] A.W. Sandvik, A. Avella and F. Mancini, *Computational studies of quantum spin systems*, AIP, 2010, DOI.

[176] U. Wolff, *Collective monte carlo updating for spin systems*, *Phys. Rev. Lett.* **62** (1989) 361.

[177] R.H. Swendsen and J.-S. Wang, *Nonuniversal critical dynamics in monte carlo simulations*, *Phys. Rev. Lett.* **58** (1987) 86.

[178] R.H. Swendsen, J.-S. Wang and A.M. Ferrenberg, *New monte carlo methods for improved efficiency of computer simulations in statistical mechanics*, *Topics in Applied Physics* (1992) 75–91.

[179] E. LUIJTEN and H.W. BLÖTE, *Monte carlo method for spin models with long-range interactions*, *International Journal of Modern Physics C* **06** (1995) 359–370.

[180] A. Dutta and J.K. Bhattacharjee, *Phase transitions in the quantum Ising and rotor models with a long-range interaction*, *Physical Review B* **64** (2001) 184106.

[181] H. Lipkin, N. Meshkov and A. Glick, *Validity of many-body approximation methods for a solvable model: (i). exact solutions and perturbation theory*, *Nuclear Physics* **62** (1965) 188 .

[182] R. Botet and R. Jullien, *Large-size critical behavior of infinitely coordinated systems*, *Physical Review B* **28** (1983) 3955.

[183] F.J. Dyson, *Existence of a phase-transition in a one-dimensional Ising ferromagnet*, *Communications in Mathematical Physics* **12** (1969) 91.

[184] M.E. Fisher, S.-k. Ma and B.G. Nickel, *Critical Exponents for Long-Range Interactions*, *Physical Review Letters* **29** (1972) 917.

[185] E. Luijten and H.W.J. Blote, *Classical critical behavior of spin models with long-range interactions*, *Phys. Rev. B* **56** (1997) 8945.

[186] A.W. Sandvik, *An introduction to quantum monte carlo methods*, in *Strongly Correlated Magnetic and Superconducting Systems*, G. Sierra and M.A. Martín-Delgado, eds., (Berlin, Heidelberg), pp. 109–135, Springer Berlin Heidelberg, 1997.

[187] M.C. Angelini, G. Parisi and F. Ricci-Tersenghi, *Relations between short-range and long-range Ising models*, *Physical Review E* **89** (2014) 062120.

[188] J.A. Koziol, A. Langheld, S.C. Kapfer and K.P. Schmidt, *Quantum-critical properties of the long-range transverse-field ising model from quantum monte carlo simulations*, *Physical Review B* **103** (2021) .

[189] E.J. Flores-Sola, B. Berche, R. Kenna and M. Weigel, *Finite-size scaling above the upper critical dimension in Ising models with long-range interactions*, *The European Physical Journal B* **88** (2015) 28.

[190] B. Sciolla and G. Biroli, *Dynamical transitions and quantum quenches in mean-field models*, *Journal of Statistical Mechanics: Theory and Experiment* **2011** (2011) 11003 [1108.5068].

[191] B. Žunkovič, M. Heyl, M. Knap and A. Silva, *Dynamical Quantum Phase Transitions in Spin Chains with Long-Range Interactions: Merging Different Concepts of Nonequilibrium Criticality*, *Phys. Rev. Lett* **120** (2018) 130601.

[192] M. Rigol, V. Dunjko and M. Olshanii, *Thermalization and its mechanism for generic isolated quantum systems*, *Nature* **481** (2012) 224.

[193] D.M. Ceperley and E.L. Pollock, *Path-integral computation of the low-temperature properties of liquidhe4*, *Physical Review Letters* **56** (1986) 351–354.

[194] J.E. Cuervo, P.-N. Roy and M. Boninsegni, *Path integral ground state with a fourth-order propagator: Application to condensed helium*, *The Journal of Chemical Physics* **122** (2005) 114504.

[195] M. Boninsegni, N.V. Prokof'ev and B.V. Svistunov, *Worm algorithm and diagrammatic monte carlo: A new approach to continuous-space path integral monte carlo simulations*, *Physical Review E* **74** (2006) .

[196] M. Boninsegni, N. Prokof'ev and B. Svistunov, *Worm algorithm for continuous-space path integral monte carlo simulations*, *Physical Review Letters* **96** (2006) .

[197] N. Prokof'ev, B. Svistunov and I. Tupitsyn, *"worm" algorithm in quantum monte carlo simulations*, *Physics Letters A* **238** (1998) 253.

[198] S. Saccani, S. Moroni and M. Boninsegni, *Phase diagram of soft-core bosons in two dimensions*, *Physical Review B* **83** (2011) .

[199] S. Saccani, *Quantum Monte Carlo studies of soft Bosonic systems and Minimum Energy Pathways*, Ph.D. thesis, SISSA, 2013, http://hdl.handle.net/20.500.11767/4931.

[200] E.L. Pollock and D.M. Ceperley, *Path-integral computation of superfluid densities*, *Physical Review B* **36** (1987) 8343–8352.

[201] F. Pietracaprina, V. Ros and A. Scardicchio, *Forward approximation as a mean-field approximation for the anderson and many-body localization transitions*, *Phys. Rev. B* **93** (2016) 054201.